(2)

Lead Detection and Mapping with Reference to Relationships Between Scale, Sensor Characteristics, Surface Conditions and Atmospheric Properties

ANNUAL REPORT

15 April 1991 - 14 April 1992

ONR Grant No: N00014-90-J-1840

J. Key, R.S. Stone, J.A. Maslanik, and E. Ellefsen

Cooperative Institute for Research in Environmental Sciences
Division of Cryospheric and Polar Processes
University of Colorado
Boulder, CO 80309-0449

20 April 1992

Lead Detection and Mapping with Reference to Relationships Between Scale, Sensor Characteristics, Surface Conditions and Atmospheric Properties

ANNUAL REPORT

15 April 1991 - 14 April 1992

ONR Grant No: N00014-90-J-1840

J. Key, R.S. Stone, J.A. Maslanik, and E. Ellefsen

Cooperative Institute for Research in Environmental Sciences
Division of Cryospheric and Polar Processes
University of Colorado
Boulder, CO 80309-0449

20 April 1992

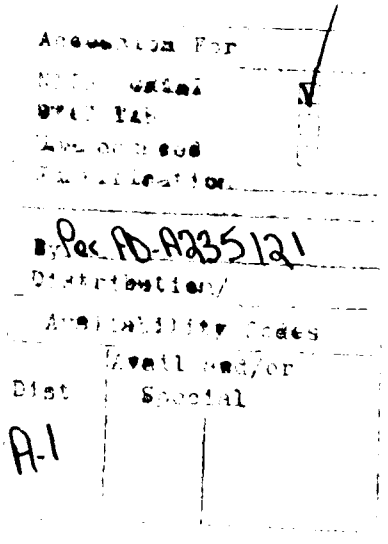

TABLE OF CONTENTS

SUMMARY

This project was originally proposed and funded for a two-year period. A third year of research has recently been proposed and, while its subject matter is a logical extension to that of the first two years, it is also a change in direction (section III.3). Therefore we present here results from the first two years collectively, rather than the second year alone. Those topics that are exclusive to either year 1 or year 2 are identified. In some cases, however, the topics described in this report were initially investigated in year 1 and continued in year 2.

During the first two years of the project, empirical studies of scale relationships in the retrieval of sea ice lead statistics have been undertaken, as have modeling investigations of atmospheric influences on the satellite signal. Additionally, we have developed statistical models that describe the scaling properties of leads. The empirical studies have been based primarily on comparisons within and between Landsat and AVHRR imagery, while the atmospheric models have been specific to the AVHRR. Submarine sonar data have been used in the statistical model development. Specific accomplishments to date include:

(1) The parameterizations of clouds, haze, and atmospheric chemical constituents in the LOWTRAN 7 radiative transfer model have been reviewed. Atmospheric temperature and humidity profiles for the arctic have been constructed from Soviet ice island data and are being used in the model. (Year 1)

(2) Resampling methods have been tested on simulated, AVHRR, and Landsat images, as have the effects of digital enhancements. (Year 1)

(3) Procedures for the retrieval of lead statistics have been developed and applied to Landsat imagery successively degraded to more coarse resolutions.

(4) The relationship between "apparent" lead widths measured along a transect (e.g., from submarine sonar or as a sampling method for satellite imagery) and the "true" lead width distribution has been formalized in a statistical sense, so that one distribution may be obtained from the other. Submarine sonar data have been analyzed in this context. (Year 1)

(5) A statistical model has been developed for the retrieval of lead area fraction from measurements along a line; e.g., a submarine sonar transect or a lineal sampling method for satellite images.

(6) The effect of atmosphere/surface conditions on the AVHRR-measured radiance in the thermal channels has been examined in terms of thermal contrast. Surfaces include open water, 5 cm, 15 cm, and 2 m thick ice. Atmospheric conditions include clear sky with haze, cirrus, and low-level ice crystal plumes.

(7) Additional KRMS data has been acquired for a time period in which DMSP OLS data is

currently being used in the analysis of lead patterns.

(8) Information on Arctic aerosol optical depths during LEADEX have been collected by two of the investigators on the NOAA P-3 with sun photometers. This information will be used in future radiative transfer applications.

(9) Two workshops for the satellite remote sensing investigators of the Leads ARI have been hosted by this group in Boulder. Recommendations for instrumentation during LEADEX'92 were made.

One workshop report and two referreed papers have been published, and one paper has been submitted for publication. Three additional papers are in preparation for submission to referreed journals. Two graduate students have been supported part-time over the course of the project.

PROJECT OBJECTIVES

The goal of this project is to understand how sensor characteristics, atmospheric properties, and surface conditions influence the detection and interpretation of sea ice leads using Advanced Very High Resolution Radiometer (AVHRR) and other satellite data. We seek to determine the sources and magnitudes of errors inherent in the measurements, how data from different sensors can be combined, and how lead statistics change with the different spatial resolutions of existing and future sensors.

In partial fulfillment of these objectives, we have defined which atmospheric and surface parameters are most critical for lead detection. Based on model simulations, we have been able to better evaluate the importance of Arctic-specific model parameters; e.g., temperature and humidity profiles and aerosols, for the purpose of accurately simulating sensor responses. Sensor characteristics such as spectral response, field-of-view, spatial resolution, scan geometry and data processing methods coupled with scene variability (solar zenith angle, atmospheric opacity, surface temperature, snow cover, ice thickness, size with respect to sensor resolution) determine feature signatures. The effects of these parameters had to be examined before lead signatures could be evaluated in terms of lead width and orientation, particularly for features that occur near spatial and radiometric limits of sensor resolution.

The NOAA AVHRR satellite sensor provides daily, Arctic-wide coverage of ice conditions at moderate resolution and low cost. These image sets contain information that is of primary concern to research and operational interests in the Arctic. Although a variety of studies have examined various aspects of remote sensing of sea ice, essentially no work had previously been done to relate lead signatures observed in AVHRR data to lead characteristics. This lack of substantive verification work left key questions unanswered and posed significant research problems relevant to current lead investigations. Specifically, the following questions motivated our research during the first two years of the project:

Lead and Surface Characteristics: How does lead detection depend on ice thickness for given sets of sensor properties, surface temperatures, and atmospheric conditions? Since the temperature contrast between open water and ice provides a means to map leads using thermal imagery, to what degree does this contrast affect the apparent width of a lead as observed in an image and our ability to detect it? Does lead orientation affect lead detection when a wide-angle scanning instrument such as AVHRR is used instead of a nadir-viewing sensor such as Landsat? How accurately must surface temperatures be measured to yield accurate lead calculations?

Atmospheric, Boundary Layer, and Solar Zenith Angle Effects: How do these factors combine with surface conditions and path length to the sensor to determine the thresholds of lead detection? What feedbacks to the atmosphere do leads create, and how will these affect detection; e.g., ice crystal plumes from open leads that extend up to - and in some cases through - the top of the inversion layer? What are the characteristics of "typical" polar atmospheres (i.e., water vapor content, temperature profiles, cloud microphysical

characteristics), how are they treated in radiative transfer models, and how do these factors affect remote sensing?

General Sensor Considerations: In what ways might sensor scan-angle, sensor calibration, data gridding, and image enhancements influence the ability to detect leads? Are lead statistics derived from image centers where spatial resolution is greatest comparable to those derived from image limbs where resolution is poorest?

While we do not claim to be able to answer all of these questions completely, the results of the past two years' research have given us at least partial answers to each. The data collected during LEADEX will be used in the validation of those results.

To accomplish our objectives, our approach includes both modeling and empirical studies (Figure 1). The radiative transfer modeling is done for the purpose of simulating the satellite sensor response under a variety of atmospheric and surface conditions. The empirical studies include: a comparison of lead statistics determined in imagery of varying scales; e.g., AVHRR, Landsat, KRMS and OLS data; effects of different resampling methods and digital image enhancements on lead detection in AVHRR and Landsat data; use of distributions derived from the low resolution imagery to estimate characteristics of the distributions obtained in the high resolution images; and the relationship between lead width and spacing statistics measured along a transect to the true distributions.

Results from this work will be important to the development and application of lead detection and mapping algorithms proposed elsewhere within the Leads ARI. For example, the ability to more accurately access lead width and spacing distributions from medium resolution imagery is crucial to the evaluation of large-scale heat flux estimates. The modeling and empirical approaches to quantifying the relationships of scale discussed here are a necessary first step to operational lead analysis from satellite data.

Satellite data used in this study includes Landsat visible, AVHRR visible and thermal, KRMS passive microwave, and OLS visible and thermal. Additionally, lead statistics have been derived from submarine sonar data. Radiosonde temperature and humidity profiles from arctic ice islands are employed for radiative transfer studies. Each data type is described in more detail in the appropriate sections.

This report is divided into three parts. The first details those studies that relate directly to retrieving lead statistics from satellite imagery: image preprocessing, sensor field-of-view, and sampling methods. The second part describes radiative transfer studies of how the atmosphere affects the satellite signal and how this in turn might affect lead statistics derived from the imagery. The third part of the report summarizes the accomplishments to date and future plans.

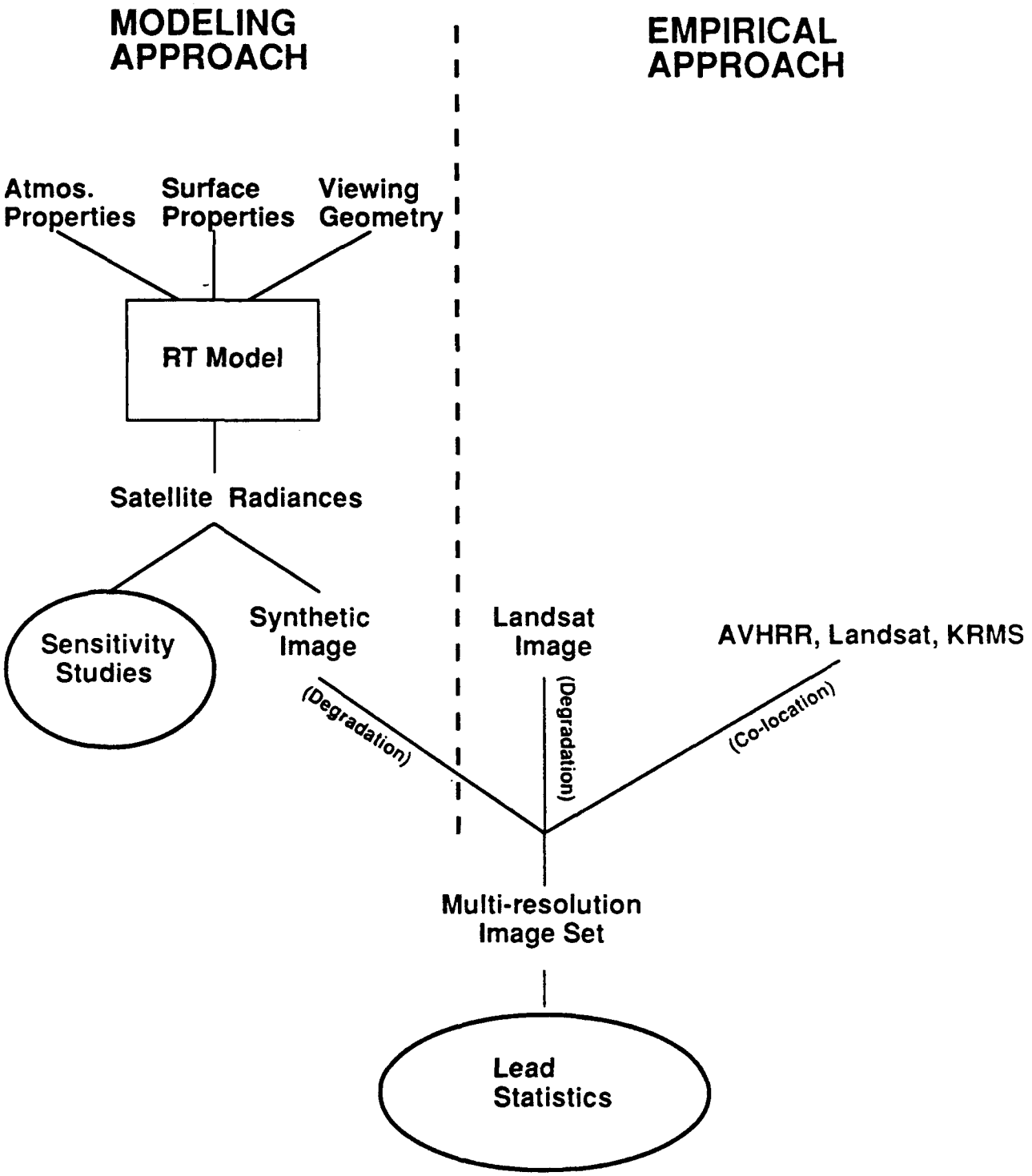

Figure 1. Overview of the modeling and empirical approaches to the study of lead mapping and relationships of scale in satellite data. The radiative transfer model on the left is used for sensitivity studies and to generate synthetic imagery. This imagery as well as Landsat data are degraded to coarser resolutions. The simulated multi-resolution data sets, along with actual data from different satellite sensors, are used to study the effects of measurement scales on derived lead statistics.

Part I: IMAGE-RELATED STUDIES

The empirical portion of this study involves the comparison of AVHRR, Landsat, and - to a limited extent - KRMS data. These sensors provide a broad range of spectral and spatial resolutions. In this section, the potential effect of image preprocessing methods on lead statistics is examined.

I.1 IMAGE PREPROCESSING AND ITS EFFECT ON LEAD STATISTICS

Figures 2 and 3 show the effect on lead detection in AVHRR imagery of different resampling methods and different digital number thresholds for "lead / no lead" mapping. The plots in Figure 2 of digital numbers along transects in AVHRR data processed using different resampling schemes show some relatively small shifts in digital number (DN) within leads and adjacent to leads, which would yield a change in estimated lead-covered area (such as at transect location 292-293 in Figure 2a). For small leads, the potential exists to perhaps mask the lead completely (as at transect location 279 in Figure 2a). Figure 3a shows results using a threshold that detects small and large leads. The threshold used for Figure 3b detects only the larger leads. The effect of the "smoothing" interpolations (bilinear and cubic convolution) is to eliminate about 40% of the smallest leads using this threshold detection scheme. Figure 4 summarizes the effect of threshold and resampling scheme on total lead-covered area (in this case, the percent of an AVHRR image covered by leads). The effect of using different resampling schemes is small compared to the effect of choosing different thresholds. Thus, while Figure 3 suggests a substantial reduction in small leads when interpolations are used vs. nearest neighbor, the effect of the loss of these small leads on total lead area is relatively small. However, it is also worth noting that, since the turbulent fluxes from a given lead-covered area increase as the proportion of lead-covered area in narrow leads (as opposed to wide leads) increases, any systematic shift by the processing scheme toward a reduction in small leads may need to be considered when calculating regional estimates of surface fluxes.

To further examine the effects of different interpolation schemes, "synthetic" images containing a simulated lead or lead complex with different shapes and dimensions (e.g., the patterns shown in Figure 5) are used. Four lead types were created (e.g., "Type 1", etc. in Figure 5): Type 1 represents narrow open-water leads; Type 2 wider open-water leads; Type 3 leads with new and young ice growing from the edges of the leads; and Type 4 representing leads with new ice building up along one side of the leads. These images were then resampled using bilinear interpolation and nearest-neighbor methods. Resampling was applied to a 45° rotation of the original images. Table 1 lists the change in lead-covered area resulting from the resampling and determined using two different thresholds. A DN of 10 (a typical reflectance for open water) was chosen to represent open water and a DN of 85 was used for ice-covered pixels. The effects are clearly dependent on the threshold chosen to define the cut-off between whether to consider a pixel as part of a lead or not. Both the bilinear and nearest neighbor interpolations cause large reductions in the area assumed to be open water. When a threshold is chosen at a higher reflectance, such as would be appropriate to detect all pixels with some open water or thin ice in them, then the percentage of pixels with some lead-covered area increases substantially when bilinear interpolation is used.

In addition to affecting the calculation of lead-covered area, the different resampling schemes affect the appearance of leads in an image, and thus the ability of an interpreter or automated pattern-recognition scheme to detect the leads. In particular, nearest neighbor resampling tends to break up the linearity of leads. Figure 6 shows a lead complex in Landsat imagery resampled using nearest neighbor (Figure 6a), with an attempt at reconstituting the linearity using a median filter (Figure 6b). As with most enhancements, the improvement is subjective, but the lead patterns appear more well defined in the median-filtered image.

Additional insight into the effects of spatial resolution and sensor properties can be gained by comparing colocated imagery from different sensors. Figure 7 shows registered Landsat MSS imagery (top) and AVHRR data (bottom) for a portion of the Beaufort Sea. While the same general lead structure is apparent in both images, the ability to detect the smaller leads is considerably reduced in the AVHRR image (maximum spatial resolution of 1.1 km) vs. the 80 m Landsat image. This effect of spatial resolution on lead detection, as well as the effect of different spectral information on lead mapping, is also illustrated in Figure 8, which shows a subsection of the Landsat and AVHRR images, as well as a KRMS strip superimposed on the Landsat data. This comparison of how leads are represented in visible-band wavelengths (the Landsat), thermal (AVHRR), and passive microwave (KRMS), points out the problems of intercomparing lead statistics derived from different sensors. In this example, threshold detection of lead-covered area in the three data types yields 1.1% lead-covered area in the Landsat, 12.8% in the AVHRR (which includes apparent low cloud with substantially warmer temperatures than the ice surface), and 5.4% lead-covered area in the KRMS image.

These different representations are perhaps better represented by comparing transects through the imagery. Figure 9 shows such a transect. The lead located at transect location 32 is marked with an arrow on the Landsat image in Figure 8. The transect runs vertically through the imagery. In this example, a contrast stretch was applied to the AVHRR data to enhance the subtle DN differences in the image. From these comparisons and a similar comparison of transects in AVHRR (unenhanced) and Landsat (Figure 7), it is fairly clear that the AVHRR and Landsat reveal similar lead patterns, but that the number of leads detected, and the image area that is considered to be partially lead-covered, is quite sensitive to the DN threshold chosen to define lead area. In Figure 9, for example, the large lead at location 32 could be defined as having a lead width from 800 m to about 1500 m in the Landsat data depending on the DN threshold used, and from 300 m to 1800 m in the AVHRR, again depending on which DN is selected. The lead information contained in the KRMS data clearly is quite different from that shown in the other image types.

Table 1. Effect of resampling method (bilinear interpolation = BL, nearest neighbor = NN) and digital number (DN) threshold on estimation of percent lead-covered area.

		Fractional Area Lead Coverage (%) (by Resampling Method)		
Lead Type	Threshold	None	Bilinear	NN
1	≤ 84	0.65	1.23	0.82
2	≤ 84	1.83	2.61	1.77
3	≤ 84	1.83	2.59	1.77
4	≤ 84	1.83	2.60	1.77
1	≤ 10	0.65	0.01	0.00
2	≤ 10	1.83	1.19	0.00
3	≤ 10	1.83	0.00	0.00
4	≤ 10	1.83	0.64	0.00

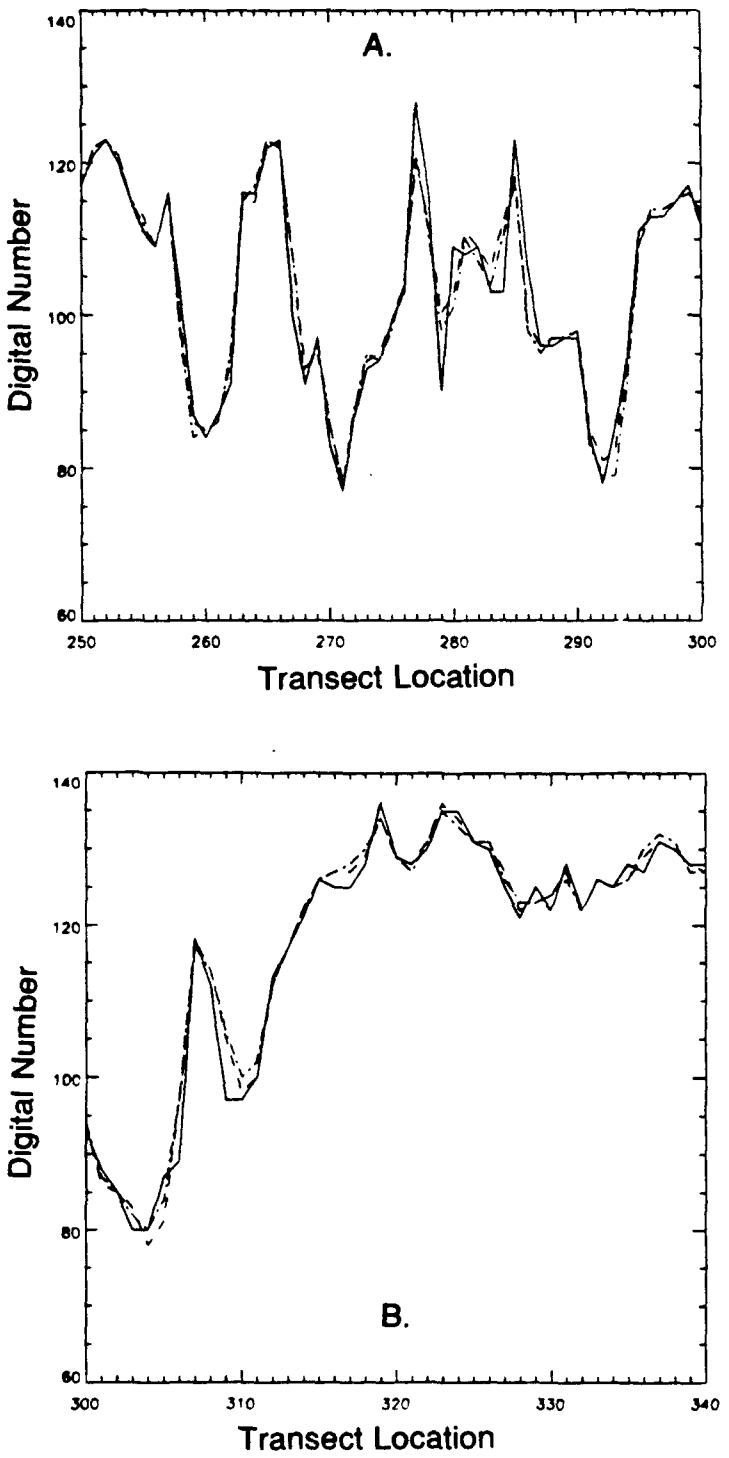

Figure 2. Change in AVHRR digital number (DN) using different resampling schemes. Plotted data are two transects (graphs A and B) through three colocated images processed using nearest neighbor (NN) (solid line), cubic convolution (CC) (dashed line), and bilinear interpolation (BI) (dot-dash line).

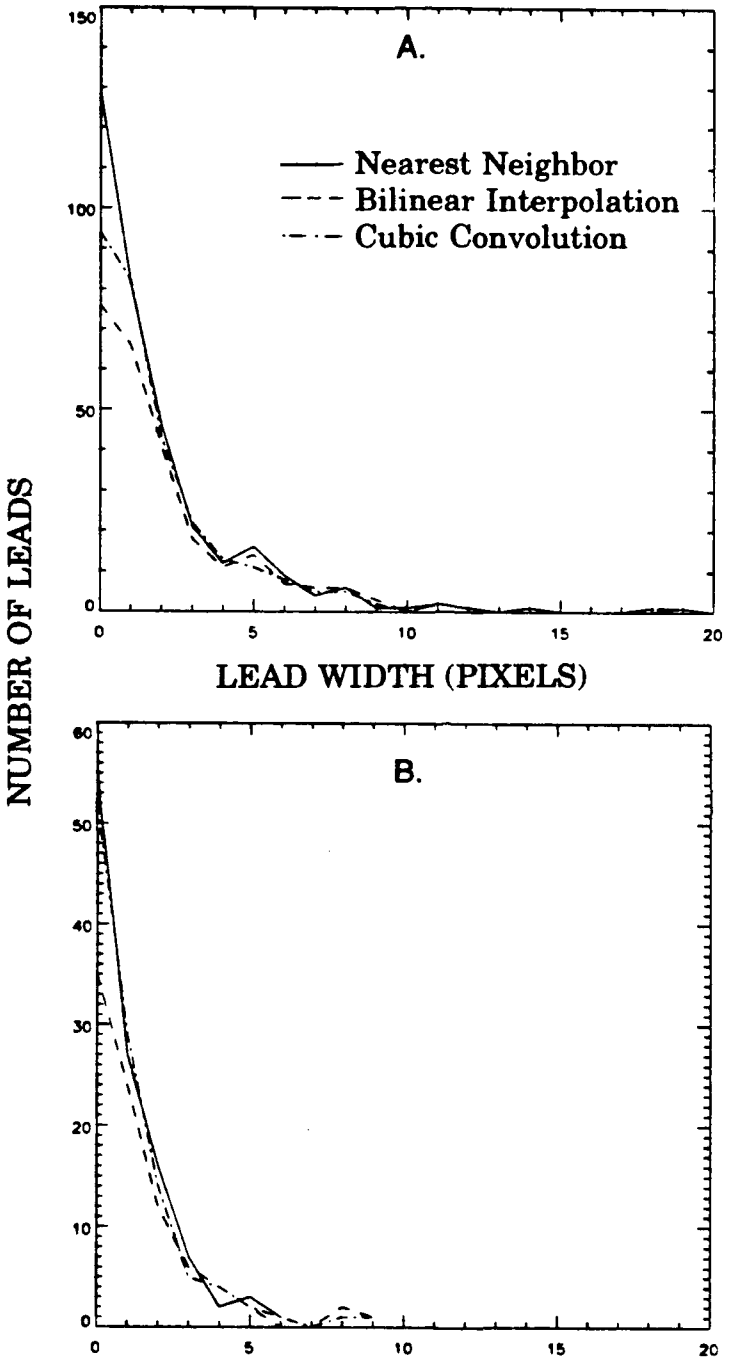

Figure 3. Comparison of number of leads encountered in AVHRR imagery resampled using NN, CC, and BI with two different DN thresholds (graphs A and B) used to represent leads.

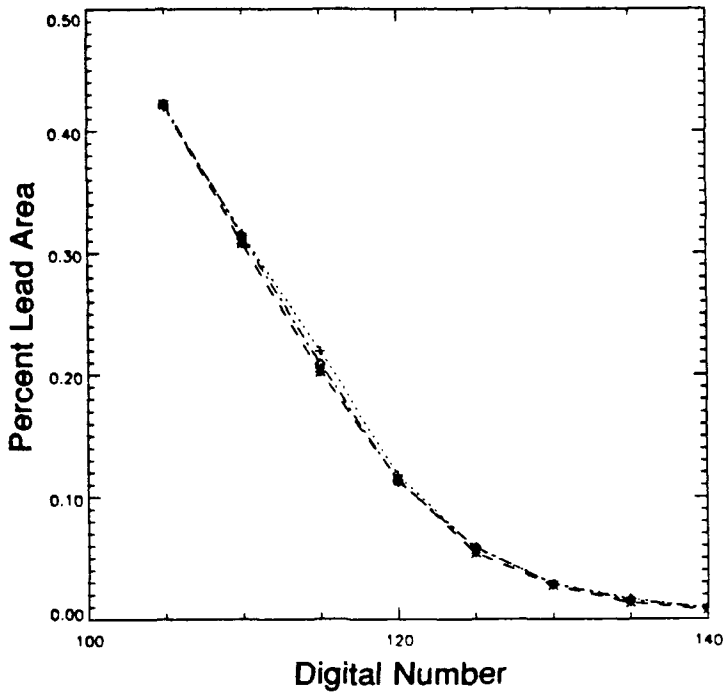

Figure 4. Change in percent lead area estimated in an AVHRR image as a function of resampling scheme and DN threshold.

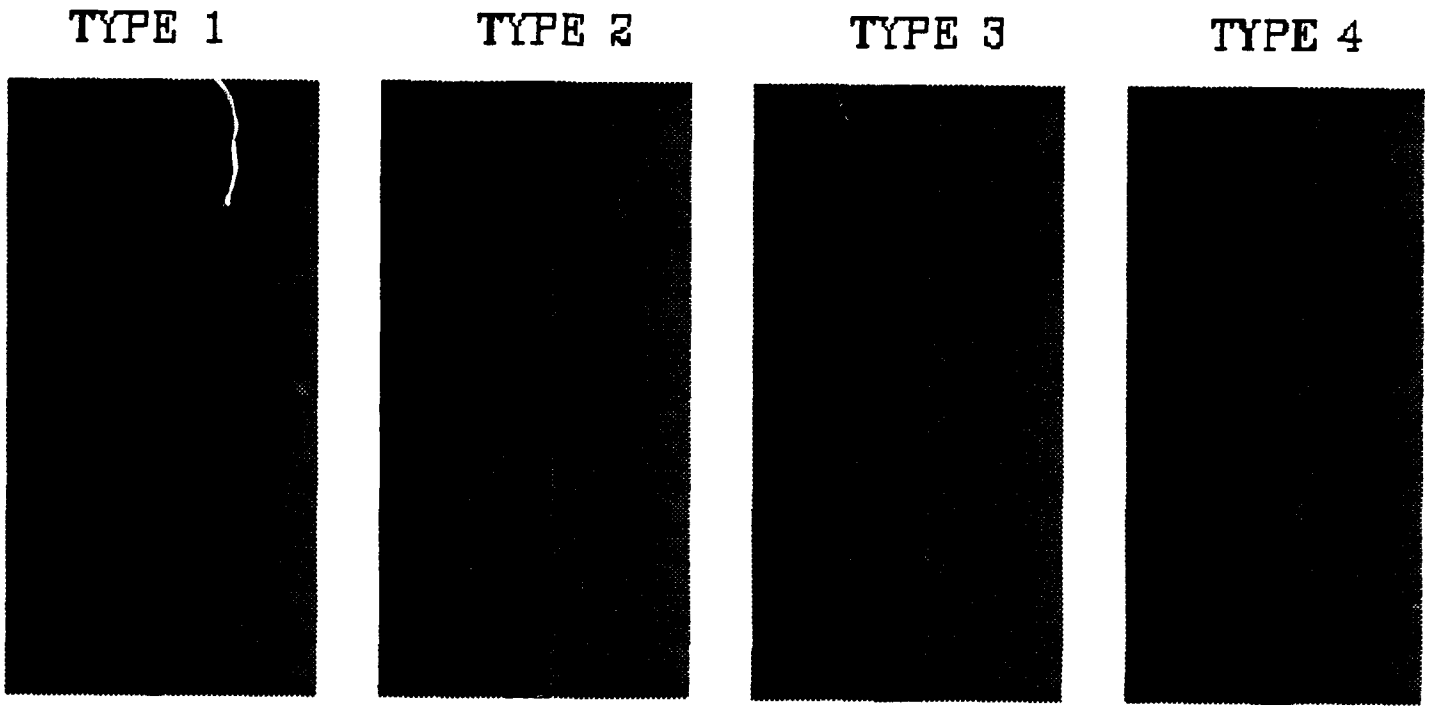

Figure 5. Synthetic images used to assess effects of resampling on different lead types.

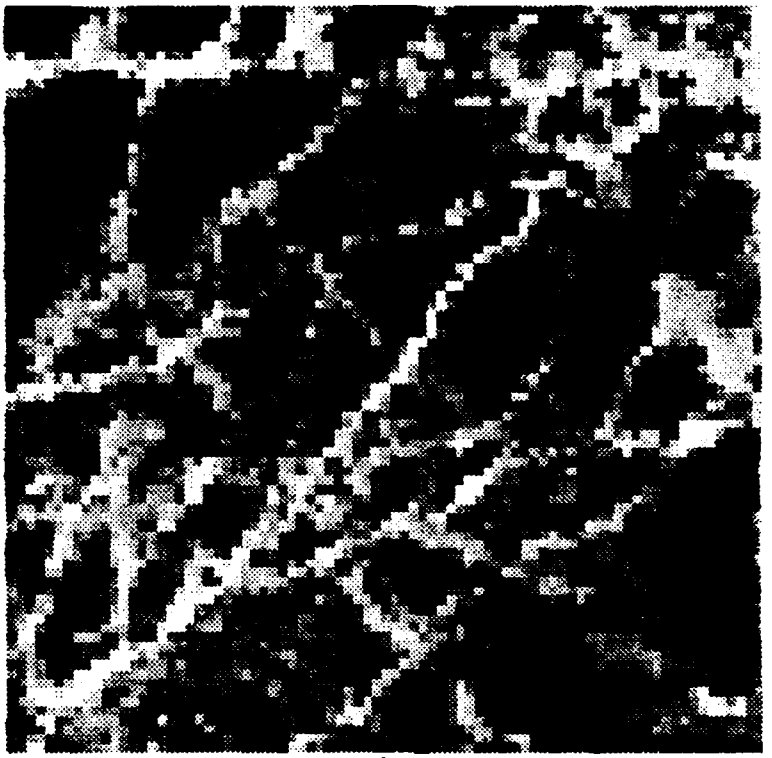

A.

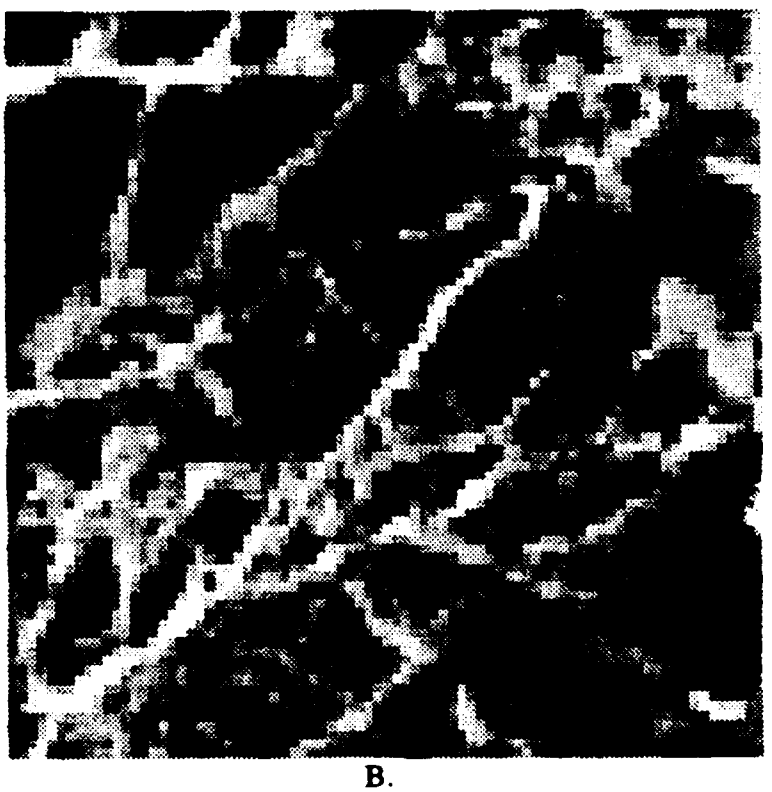

B.

Figure 6. Effect of NN resampling on lead appearance in Landsat imagery (Fig. A), and reconstruction of lead appearance through the application of a spatial filter (Fig. B).

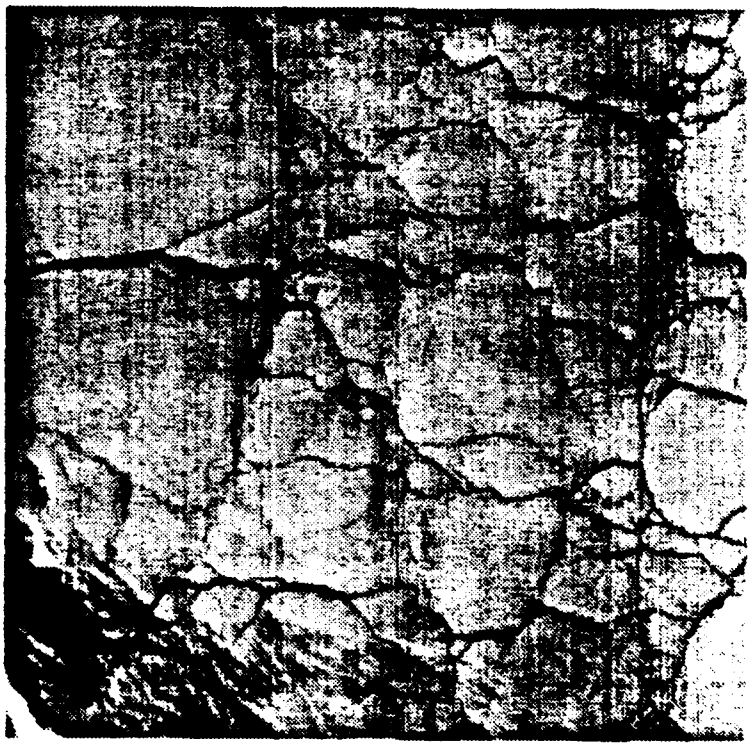

A.

B.

Figure 7. Colocated Landsat and AVHRR imagery for the Beaufort Sea, showing the representation of the same lead complex in the different image types.

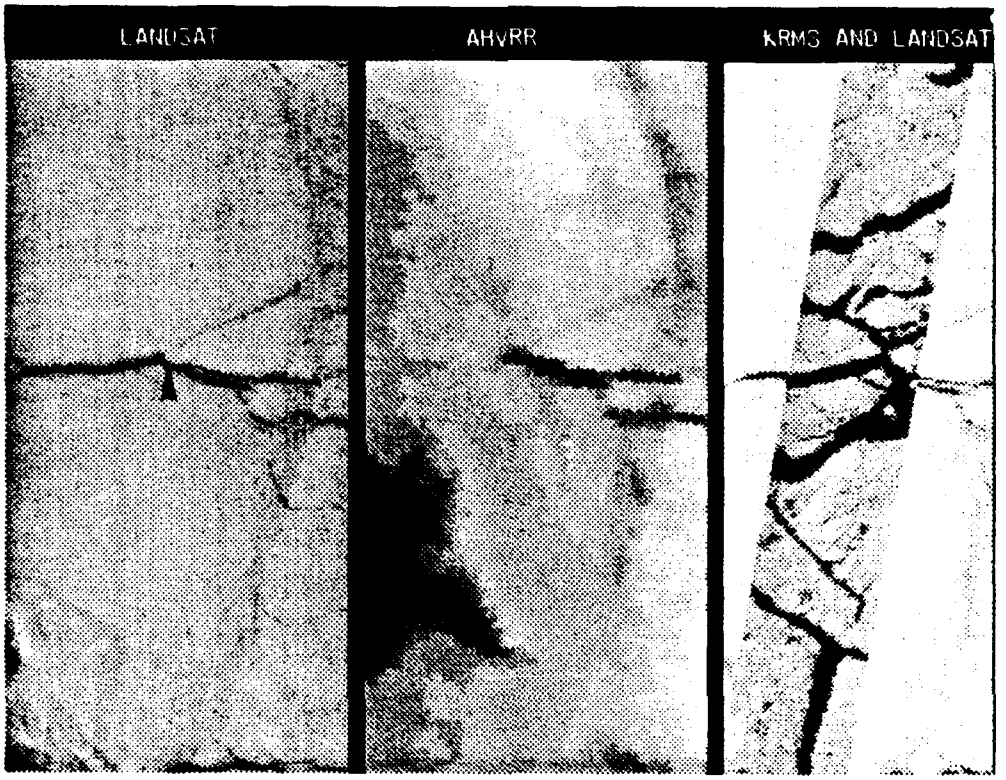

Figure 8. Colocated Landsat, AVHRR, and KRMS + Landsat imagery for the Beaufort Sea. The black arrowhead in the Landsat image marks the location of the lead and transect presented in Figure 9.

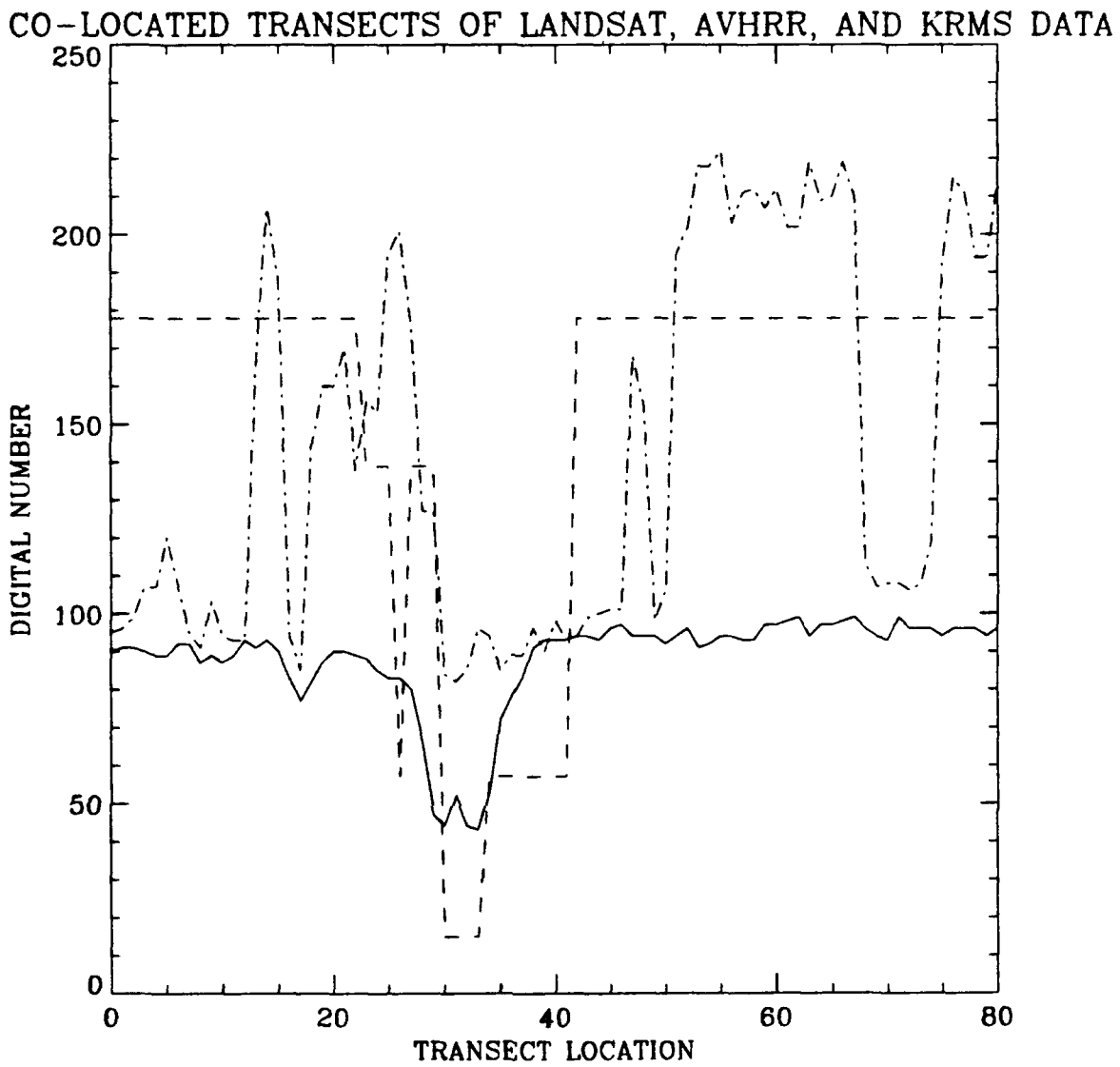

Figure 9. Transect through the imagery in Figure 8: Landsat (solid line), AVHRR (dashed line), KRMS (dot-dash line).

I.2 THEORETICAL ANALYSIS OF THE EFFECT OF SENSOR RESOLUTION ON OBSERVED FRACTIONAL AREA COVERAGE

While there have been studies of the effect of sensor resolution on parameter retrieval, the approaches have been empirical and have dealt only with cloud fraction (and a single cloud type such as cumulus; e.g., *Shenk and Salomonson* [1972], *Wielicki and Welch* [1986]) or land cover classes (e.g., *Woodcock and Strahler* [1987], *Townshend and Justice* [1988]). In the case of cloud fraction, real and simulated data containing cloud fields were degraded in resolution, and the fractional coverage was observed as a function of scale. In the case of land cover classes, the variance of the image was plotted as a function of measurement scale for the purpose of determining the optimal resolution for monitoring. While all of these studies are useful, no concise statement of the relationship between fractional coverage and sensor resolution was given, so that the results are difficult to generalize to other parameters such as leads. Figure 10 provides an example of visual changes in leads with increasing pixel size (and is described in more detail in section I.3). Here we present an analytical approach to this problem currently being investigated.

I.2.1 *Analytical Approach*

Our goal is to determine the probability distribution for the proportion of pixels in an image that have the characteristic of interest; e.g., the fraction that are cloudy or are sea ice leads, etc. This depends on the distribution of the subpixel area fraction of the parameter, specified by its shape, mean and variance. The variance depends on the pixel size and the spatial structure of the parameter, represented by its autocovariance function. The formalization that follows can be applied to virtually any geophysical parameter whose spatial distribution can be described in this manner.

I.2.1.1 Indicator Function

Let $q(x)$ be a measurable property (e.g., temperature) at the point whose position is represented by the two-element location vector x, and define ζ to be any condition on q. For example, ζ might be the condition $q(x) < t_s\text{-}\delta$, where t_s is the surface temperature and δ is some threshold value. The indicator function $I(x)$ in region R is equal to 1 if $q(x)$ satisfies ζ and 0 otherwise. The fractional coverage for which q satifies ζ is given by

$$P = A_R^{-1} \int_R I(x)\, dx \qquad (1)$$

where A_R is the area of R and is a normalizing factor. For the rest of the discussion R is a satellite image. The probability density of I is $f_I(1) = P$ and $f_I(0) = 1 - P$.

Now let $q_Z(y)$ be a measurable property of a pixel Z within R centered at location y (again, a vector). As measured by the sensor, q_Z would be an average over a pixel:

$$q_Z(y) = A_Z^{-1} \int_{Z(y)} q(x)\, dx$$

where A_Z is the area of the pixel. In reality the sensor point spread (transfer) function would play a role here, but this is beyond the scope of this study. The fractional area of R for which q_Z satisfies ζ is an estimate of the "true" fractional coverage and is

$$P' = N^{-1} \sum_R I_Z(y) \tag{2}$$

where N is the number of pixels in R and I_Z is the indicator function for the pixel based on q_Z, defined in the same way as is I for a point based on q. Our goal is to relate P' to P over a range of A_Z.

To determine P' analytically the probability density of I_Z must be known. It is not trivial, and depends on P, ζ, pixel size, and the way in which objects satisfying ζ are distributed in space. Since I_Z is a function of q_Z, which in turn depends on the fractional coverage within a pixel, p_Z, then I_Z can be expressed in terms of p_Z. For example, consider a cloud pattern where the cloud top temperature is everywhere the same. Let ζ be a thresholding operation such that

$$I_Z(q_Z) = \begin{cases} 1 & \text{if } q_Z < t_s - \delta \\ 0 & \text{otherwise} \end{cases}$$

where t_s is the surface temperature and δ is some threshold amount. (It is assumed that $t_s > t_c$, the cloud top temperature.) This is equivalent to

$$I_Z(p_Z) = \begin{cases} 1 & \text{if } p_z \geq p \\ 0 & \text{otherwise} \end{cases} \tag{3}$$

The expression $p_Z \geq p$ states that the fractional coverage within the pixel is greater than some quantity p, which has a value such that

$$(1-p)T_s + pT_c < T_s - t$$

Of course, there is a distribution of t_c, although we do not address this issue here. It should also be noted that I_Z need not have only values of 0 and 1. It could, for example, take on values of 0, 0.5, and 1 if ζ is multi-conditional. So, based on (3), the probability density of I_Z is

$$f_{I_z}(1) = Prob(P_Z \geq p)$$
$$f_{I_z}(0) = 1 - Prob(P_Z \geq p) = Prob(P_Z < p)$$

where P_Z represents the random variable subpixel fractional coverage (with specific realization

p_Z), Prob($P_Z \geq p$) represents the probability that the fractional coverage within the pixel is greater than some quantity p. Now, how is Prob($P_Z \geq p$) determined?

I.2.1.2 Distribution of Subpixel Area Coverage

For a single pixel the fractional coverage of the geophysical parameter is

$$p_Z(y) = A_Z^{-1} \int_{Z(y)} I(x)\, dx$$

which can be considered as an estimate of P. After *Stoyan et al.* [1989, p. 184], the expected value and variance of P_Z are

$$\begin{aligned} E(P_Z) &= P \\ var(P_Z) &= E[P_Z - E(P_Z)]^2 \\ &= E\left\{[A_Z^{-1} \int_Z I(x)\, dx - P][A_Z^{-1} \int_Z I(x')\, dx' - P]\right\} \\ &= A_Z^{-2} \int_Z \int_Z k_I(\|x-x'\|)\, dx\, dx' \end{aligned}$$

where k_I is the autocovariance function for the indicator function.

If a specific model distribution for P_Z is assumed, with expected value and variance as defined above, then the density of the pixel indicator function is also known. Here we use the Beta distribution, a two-parameter density function defined over the closed interval $0 \leq y \leq 1$ often used as a model for proportions:

$$f_{beta}(y) = \begin{cases} y^{\alpha-1}(1-y)^{\beta-1} \dfrac{\Gamma(\alpha+\beta)}{\Gamma(\alpha)\Gamma(\beta)}, & \alpha,\beta > 0; 0 \leq y \leq 1 \\ 0, & elsewhere \end{cases}$$

The two parameters can be determined from maximum likelihood estimation based on the mean and variance of the subpixel fractional coverage:

$$\beta = \frac{[1-E(P_Z)]}{var(P_Z)} \{E(P_Z)[1-E(P_Z)] - var(P_Z)\}$$

and

$$\alpha = \frac{E(P_Z)\beta}{[1-E(P_Z)]}$$

The shape of the distribution is related to the size of the pixel relative to the spatial

structure (e.g., wavelength) of the geophysical parameter. In the limiting case with very large pixels relative to the wavelength of cloud elements, for example, most pixels would have a similar subpixel fraction of cloud and the variance would be very small. The distribution would therefore have a single peak. On the other hand, if the pixel size is very small then the likelihood of pixels being either completely overcast or completely clear increases, the variance increases, and two peaks are expected. This is illustrated in Figure 11 where the beta distribution is shown for a mean fraction of 0.2 and variances of 0.1, 0.05, and 0.01.

Exponential covariance is a reasonable model for many geophysical parameters and is used here:

$$k_I(r) = p(1-p)\,e^{-\alpha r} \quad (r, \alpha \geq 0) \tag{4}$$

where α describes the dependence of the covariance on the vector distance $r=\|x-y\|$. Implicit in this expression is that $q(x)$ is isotropic. The parameter α can be determined from observed autocovariances. Equation 4 can be written in linear form as

$$\ln[k_I(r)] = \ln[p(1-p)] - \alpha r$$

and α determined through the method of least squares regression. Examples of observed and model autocovariances are given in Figure 12.

I.2.1.3 Distribution of P′ and its Error

As shown in (2), the random variable P' is the proportion of the N pixels in R for which $I_Z = 1$, and its sampling distribution may be approximately normally distributed (this has not yet been tested) with mean and standard error, respectively,

$$\mu = f_{I_Z}(1)$$

$$\sigma = \sqrt{\frac{f_{I_Z}(1)\; f_{I_Z}(0)}{N}}$$

if N is large. The distribution function of the fractional coverage at a particular sensor resolution, $F_{P'}$, can be determined from

$$F_{P'}(p') = \int_0^{p'} \frac{1}{\sigma\sqrt{2\pi}}\, e^{-(x-\mu)^2/2\sigma^2}\, dx \tag{4}$$

However, it is not likely that the I_Z at one location is independent of I_Z at nearby locations, so that the degrees of freedom must be adjusted to account for spatial autocorrelation. This has the effect of increasing the variance of P'.

If the true fractional coverage P is a known, single value, then one way of expressing the error is $A = |P - P'|$, $(0 \le A \le P)$, with distribution function

$$F_A(a) = Prob(A \le a) = \int_{P-a}^{P+a} f_{P'}(p')\, dp'$$

where the density function $f_{P'}$ is determined numerically from $F_{P'}$.

We note here that the preceeding formalization of the problem may not be necessary if the "object" of interest follows certain scaling laws, such as those used in the definition of fractals. It may be that the relationship between changes in some geometrical descriptor of a geophysical phenomenon and the scale of measurement is adequately described by the fractal dimension. This has been shown to be true of clouds [*Lovejoy*, 1982] and land cover classes [*DeCola*, 1989] for the relationship between area and perimeter. The stream length-drainage area relationship has also been described in terms of fractals [e.g., *Robert and Roy*, 1990]. A preliminary investigation of lead length, L, at different pixel sizes, U, in the degraded Landsat data shown in Figure 10 has also indicated a fractal characteristic. This relationship is expressed as

$$L \propto U^{1-D}$$

where D is the fractal dimension $(1 \le D \le 2)$. The data in Table 2 yield a fractal dimension of 1.18, from which we infer that lead lengths constitute a fractal set.

Table 2. Changes in open water fraction with pixel size.

Pixel Size (m)	Fraction	Area (km^2)
80	0.030	270.0
160	0.027	235.8
320	0.023	196.7
640	0.016	124.9

The above formalization is currently being tested with a Poisson line process as a simulated satellite image. The density of the process (i.e., mean spacing) is 1250 m and the orientations of the lines (leads) are random. The lines are assigned thicknesses (widths) following the negative exponential density function:

$$f_W(w) = \frac{1}{\lambda} e^{-w/\lambda}$$

where w is lead width and λ is the mean width. For the simulations λ=200m. One realization of the Poisson line process is shown in Figure 13, where the pixel size is 50 m. Figure 14 illustrates how the scan angle effect can be included in the simulated leads images.

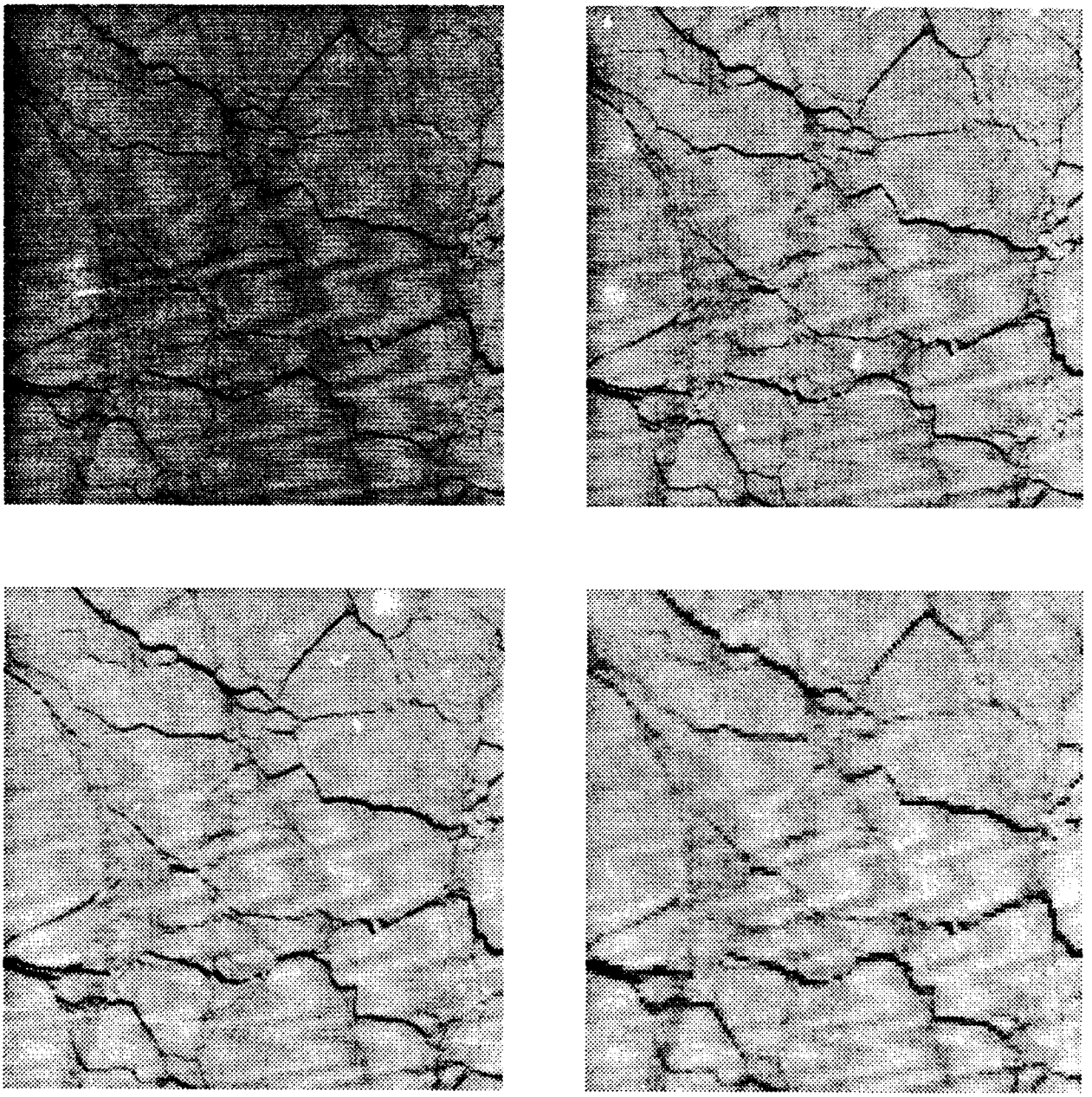

Figure 10. Landsat MSS band 4 scene of the ice pack north of Alaska in March 1988. Area covered in the upper left image is approximately (80 km)^2. The remaining are degraded images with pixel sizes of 160, 320, and 640 m.

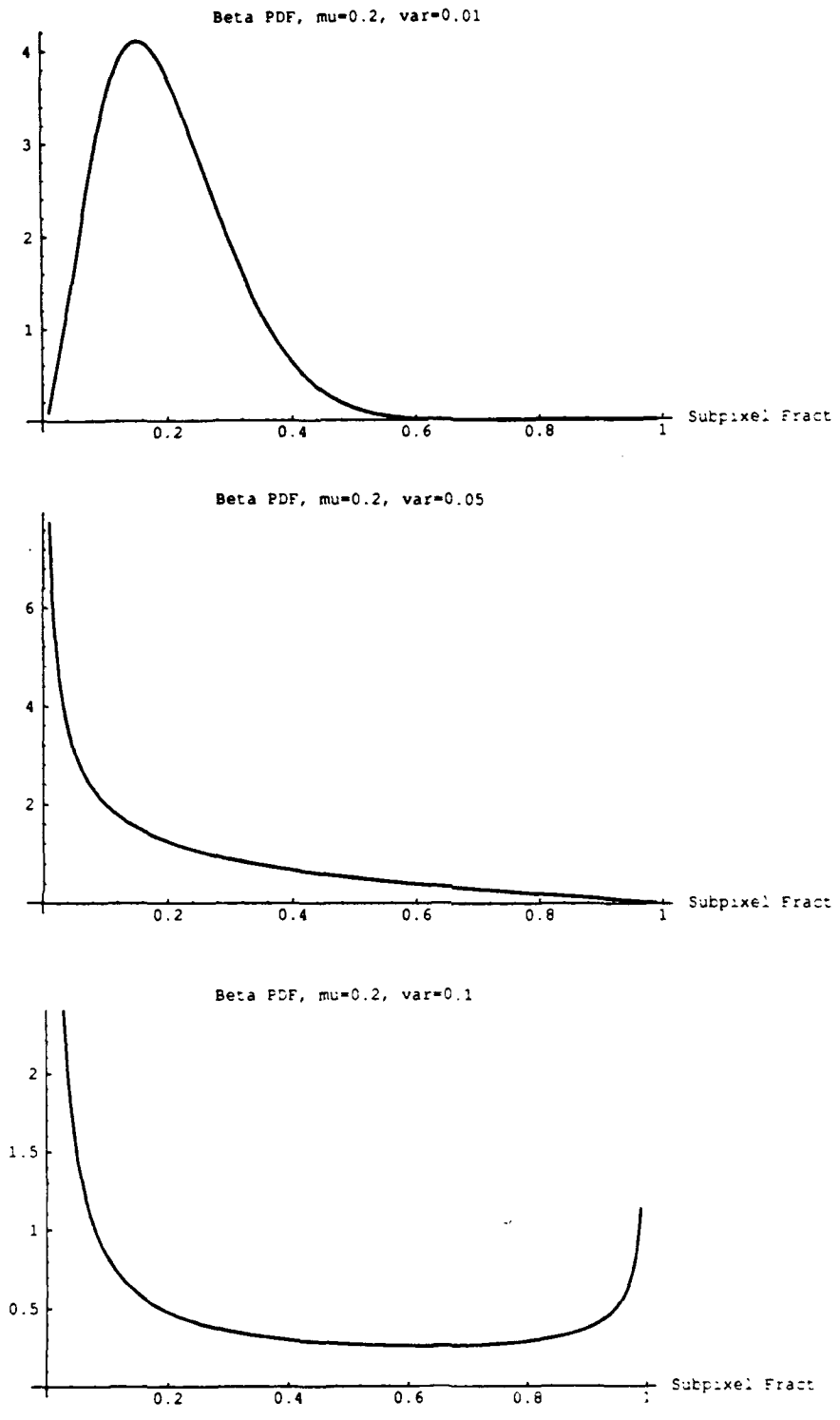

Figure 11. Three realizations of the Beta probability density function. In all cases the mean subpixel fractional coverage is 0.2. The variance is (a) 0.1, (b) 0.05, and (c) 0.01.

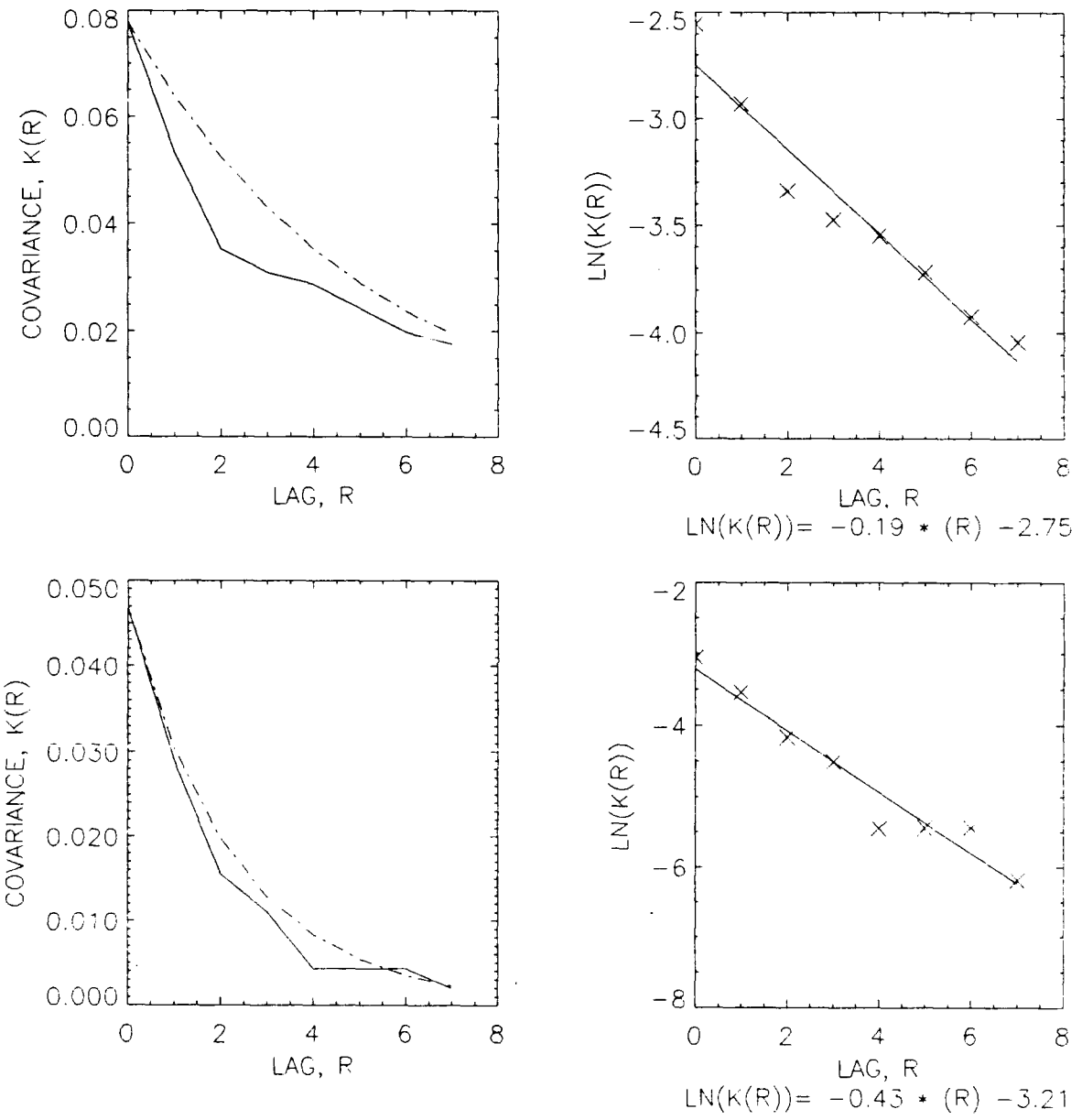

Figure 12. Autocovariance of the indicator function for two transects across the Landsat image in Figure 10. Shown are the observed (solid) and modeled (dot-dash) autocovariances on the left and the regression line fit to the observations on the right.

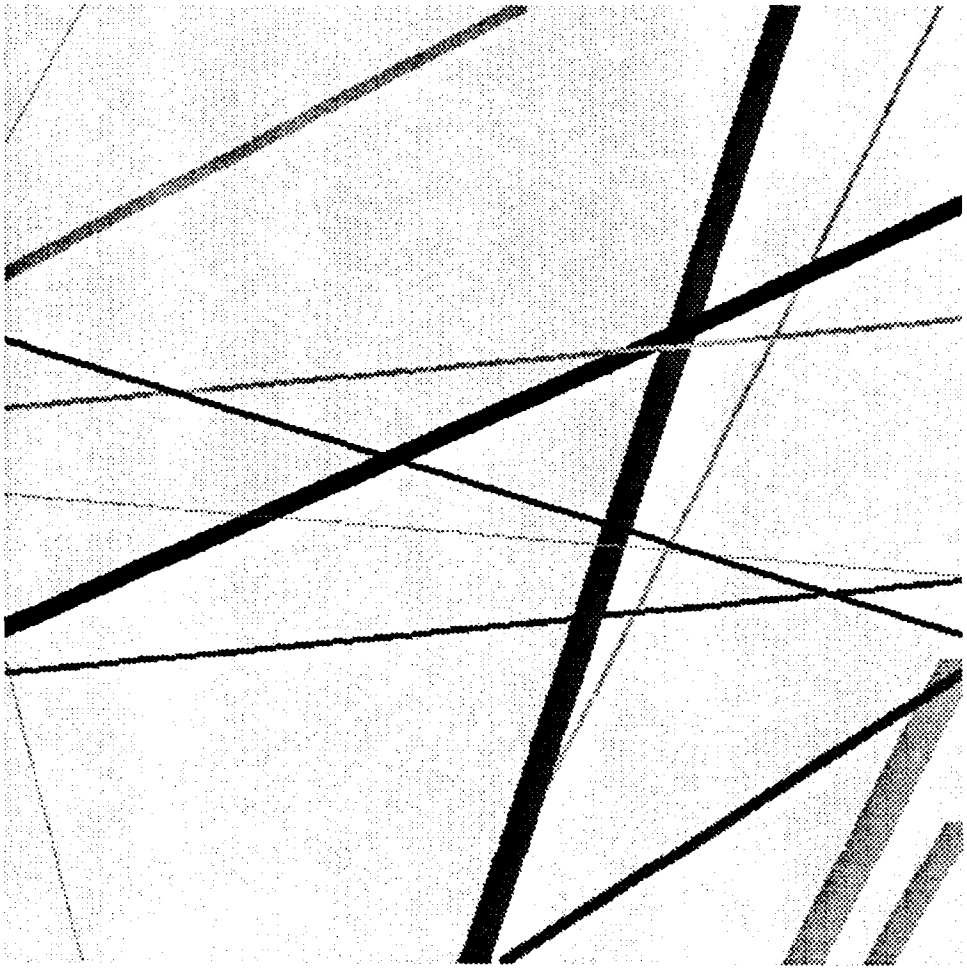

Figure 13. One realization of a Poisson line process in image form. Pixel size is 50 m.

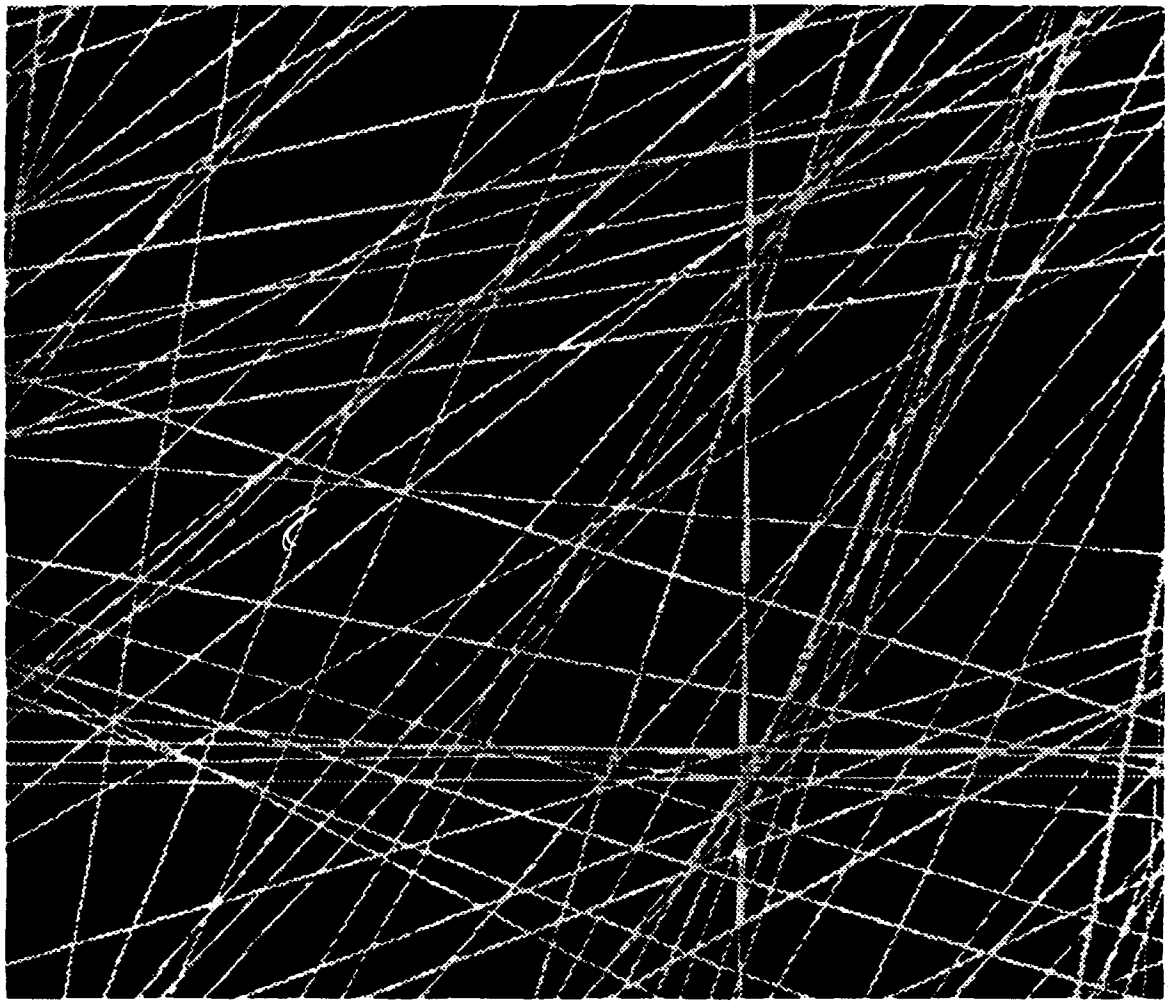

Figure 14. Another realization of a Poisson line process with the AVHRR scan angle effect included. Both images are from approximately 600 km off-nadir on the left side of the image and 1350 km off-nadir (the swath edge) on the right. In (a) all pixels are 1.1 km on a side. In (b) the scan angle effect is included.

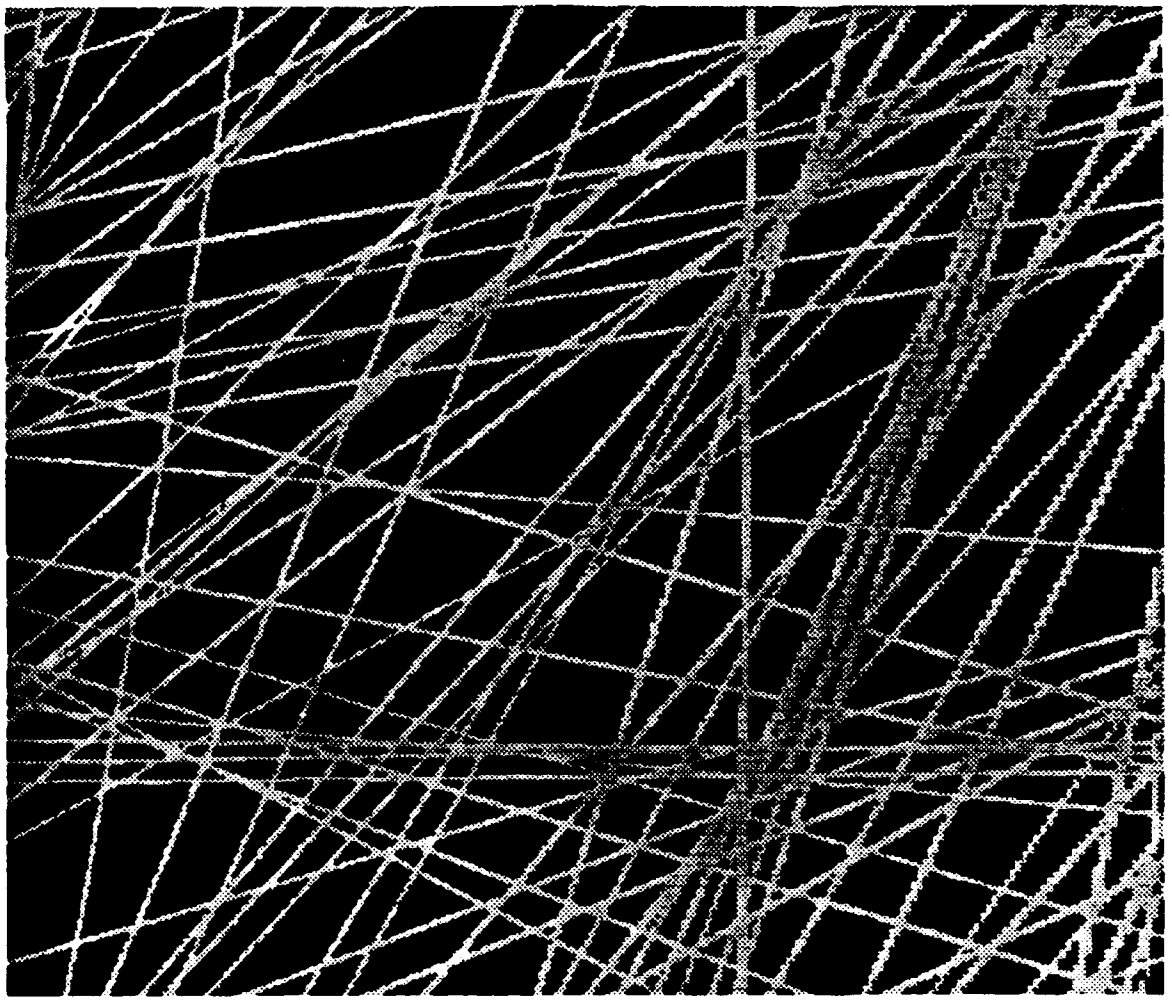

Figure 14, *continued.*

I.3 EMPIRICAL ANALYSIS OF THE EFFECT OF SENSOR RESOLUTION ON LEAD WIDTH DISTRIBUTIONS

While there are advantages to comparing lead statistics derived from different types of imagery as shown in Figure 8, such a study would be difficult given different acquisition times, wavelength ranges of the various sensors, and geolocation problems. To alleviate these problems, comparisons are made across image scales based on the same initial image, where the change in resolution is obtained by modeling the transfer function between the initial data and the desired resolution and then subsampling. A spatial filter that estimates the point spread function of the Landsat sensor is applied following the methodology presented in *Justice et al.* [1989]. At each degradation cycle, Gaussian random noise is added back into the image to reduce the smoothing effects of the filtering operation. Images with FOVs of 160, 320, 640, and 1280 m were created in this manner (Figure 10). Data are Landsat Multispectral Scanner (MSS) band 4 (0.5-0.6 μm) scenes of the Beaufort Sea, March 1988, with an initial field-of-view (FOV) of 80 m.

Lead statistics are retrieved from a lead/not-lead binary image. To obtain the binary image the fourth order trend surface is removed from original grey scale image [*Eppler and Full*, 1992] and a thresholding procedure is applied at each degradation cycle. One example is shown in Figure 15. Valid lead fragments are identified, where "valid" refers to a linear feature for which a meaningful width and orientation can be determined. Linearity is determined through correlation/regression analysis. Lead widths are measured perpendicular to the regression line, at 1 km intervals, and the slope of the regression line is the measure of the lead orientation.

The distribution of lead widths corresponding to the images in Figure 10 is shown in Figure 16. The disappearance of small leads due to a lack of contrast and the increase in the relative frequency of large leads as pixel size increases can readily be seen. In this particular image, a width threshold of approximately 250 m divides those leads which would disappear in the 320 and 640 m degradations. This change in lead widths as a function of pixel size affects the total lead area was previously illustrated (Table 2) for the images in Figure 10, where lead area fraction decreases with increasing pixel size. Orientations of leads can also be expected to change, if anisotropy (i.e., a preferred orientation) exists. An illustration of this is shown in Figure 17 for the Landsat image in Figure 10. Results from other Landsat scenes show similar patterns as do those for the simulated images.

Given the changes in the entire width distribution and in the widths of individual leads with increasing pixel size as illustrated in Figure 18, is it possible to estimate the true widths of the leads? The criteria for how a given lead will "grow" or disappear during image degradation must include a measure of its thermal contrast to the surrounding ice. For example, a narrow, open lead might grow during the first degradation, accompanied by a drop in contrast due to smoothing, and then disappear in the subsequent scene. A narrow refrozen lead, in comparison, might disappear during the first degradation. An empirical transfer function that describes this change is currently being investigated.

Figure 15. Trend surface image corresponding to the Landsat scene in Figure 10a.

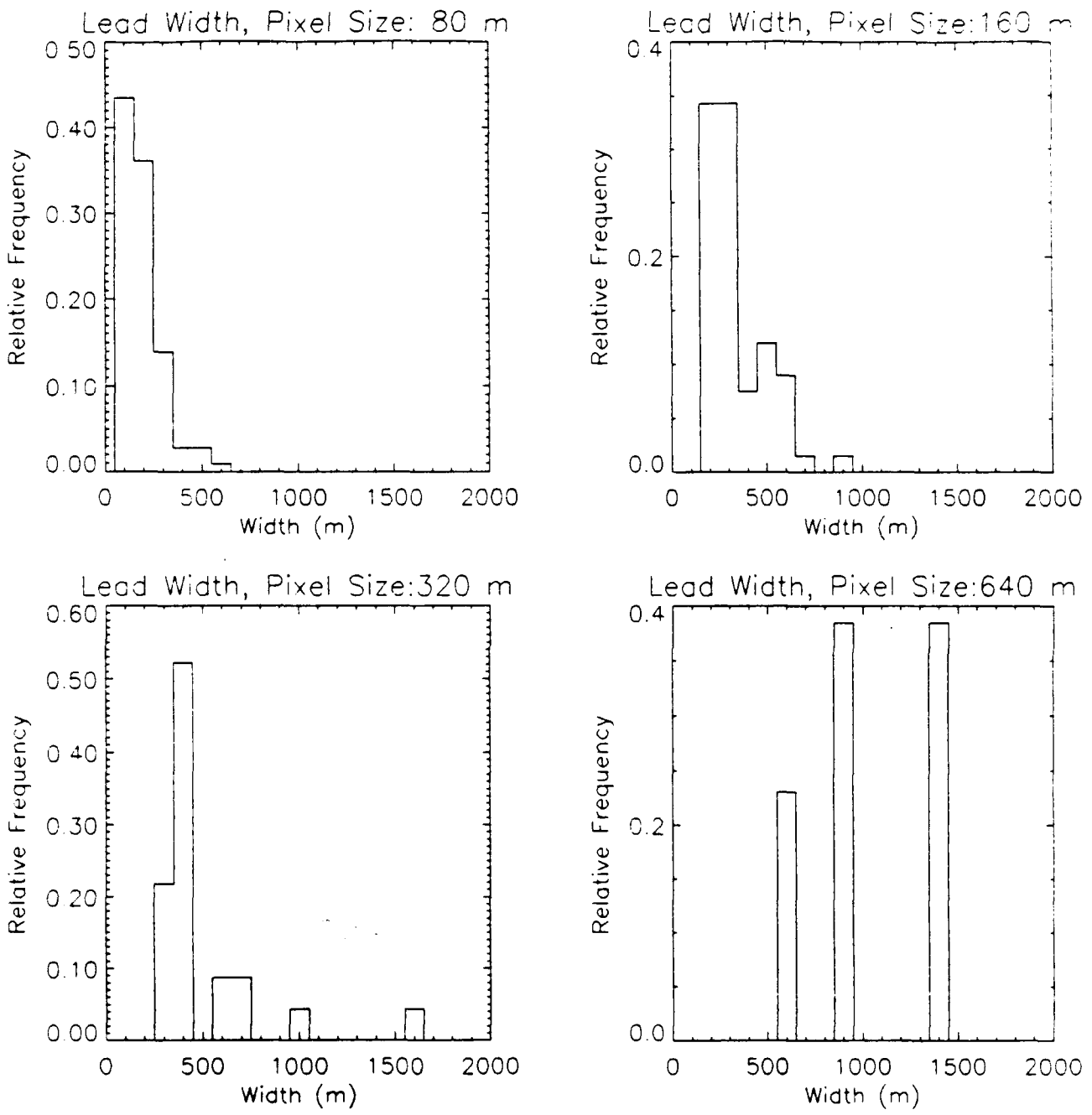

Figure 16. Lead width distributions for the images in Figure 10. Widths are grouped in 100 m bins.

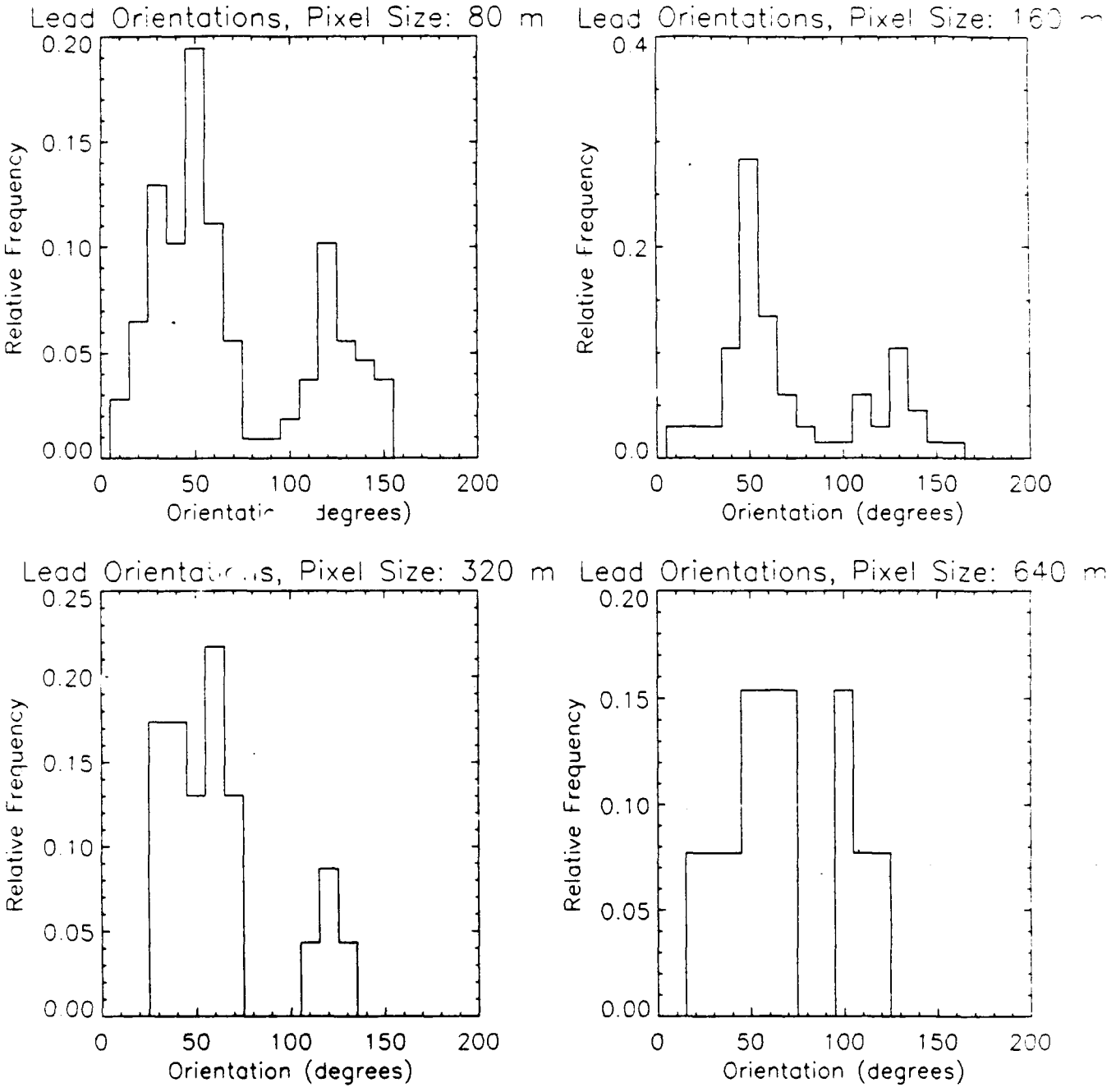

Figure 17. Lead orientations for a series the degraded Landsat imagery to that in Figure 10. Orientation is expressed as slope in a Cartesian coordinate system.

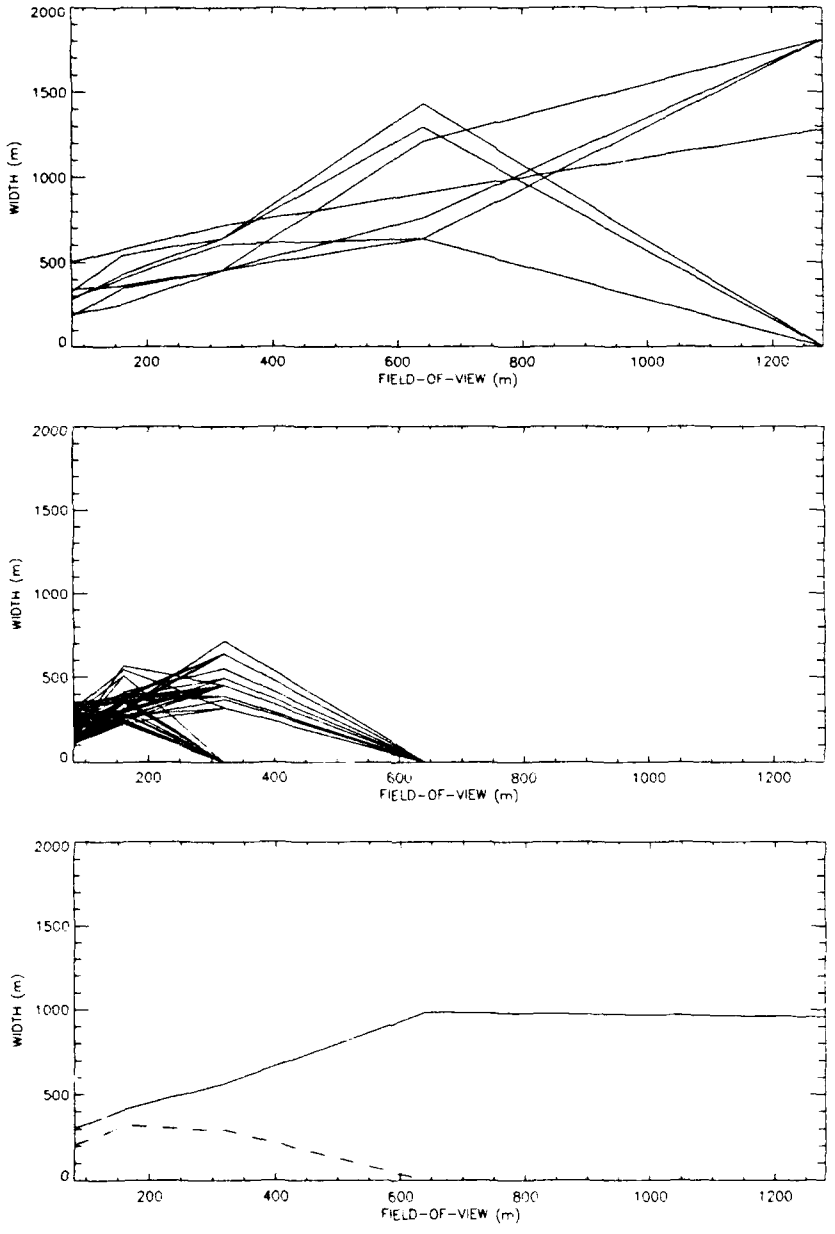

Figure 18. Change in lead widths of individual leads from Figure 10 as a function of pixel size for those that "survived" the degradation to 640 m (top), and those that did not survive (middle). The bottom plot gives the means of the top (solid) and middle (dashed) plots.

I.4 ESTIMATING WIDTH DISTRIBUTION MOMENTS FROM PARTIAL DATA

Given that very small features will generally not be resolved, the issue then becomes one concerning the possibility of using the partial distribution of a particular statistic (e.g., lead widths) measured at low resolution to estimate the complete or "true" distribution of that parameter. For example, assume that lead widths, x, follow a negative exponential distribution with an unknown mean, λ. From a sampling point of view it is useful to treat the distribution of widths as discrete and address the number n_i of leads in bin i that have widths between x_i and x_i+w where w is the width of the bin:

$$n_i = \frac{Nw}{\lambda} e^{-x_i/\lambda} \tag{5}$$

where N is the unknown total number of leads in the spatial area. The idea is that n_i is measured for a few bins, and that λ and N are estimated. To accomplish this, (5) is rewritten in linear form as

$$\ln(n_i) = \ln\left(\frac{Nw}{\lambda}\right) - \frac{1}{\lambda} x_i$$

Letting $a = \ln(Nw/\lambda)$ and $b = \lambda^{-1}$ and solving for a and b by the method of least squares with the observed data, the mean of the distribution and the total number of leads can then be estimated.

Experiments with this model show it to be very sensitive to the bin width and the number of bins in which leads actually occurred in the low resolution imagery. This is not unexpected considering that the entire range of x is being estimated in the least squares model by observations in only one part of its entire range (such extrapolation is not recommended). The problem can be alleviated somewhat by including a few observations of small lead widths; for example, measurements from a few SAR images within the same area.

I.5 LINEAL METHODS OF ESTIMATING LEAD PARAMETERS

I.5.1 *Lead Widths Measured Along a Transect*

Perhaps the largest source of high-resolution data that is potentially useful for lead statistics is that collected by submarine sonar over the last three decades. For ice draft information these data are invaluable. But can they also be used for statistics of lead geometries; i.e., lead widths and spacings? Lead width and spacing statistics have been examined in two sonar data sets. Both are in the Canada Basin (Figure 19); one in August of 1970 and one in October of 1978. Tables 3 and 4 show the results. How realistic are these data? If leads are conceptualized as linear features of some width, then crossing the lead at any angle other than perpendicular to its local orientation will result in an overestimate of the actual width.

Table 3. Lead widths (m) and standard deviations (below) in the QUEENFISH data by region, maximum draft (cm), minimum width (m). Also given are the maximum lead widths encountered. No statistics are given if fewer than 20 leads were found in a region.

MAX DRAFT/ MIN WIDTH	REGION A	B	C	D	E	F	G	H
30 / 3	26.5	33.1	21.3	26.5	47.7	------	18.5	23.8
	2.1	2.9	2.4	2.6	7.1		2.6	3.7
20	60.5	66.1	54.8	53.5	68.3	------	------	------
	3.8	5.8	5.6	5.2	9.6			
50	88.2	109.7	------	100.4	------	------	------	------
	5.3	10.8		10.4				
200	------	------	------	------	------	------	------	------
Maximum:	228	502	130	283	327		70	90
70 / 3	32.6	54.8	27.5	32.1	49.4	36.4	34.7	40.0
	3.3	3.8	2.0	2.8	7.0	8.3	3.8	3.7
20	63.7	78.1	55.6	54.2	73.7	55.9	59.0	60.4
	6.8	5.2	3.9	4.2	9.9	13.9	6.4	5.4
50	106.1	129.2	106.5	104.2	129.5	------	98.1	105.5
	14.3	8.5	7.9	9.5	19.0		10.3	9.1
200	------	------	------	------	------	------	------	------
Maximum:	885	526	255	294	374	537	257	227
100 / 3	28.9	40.8	32.9	30.9	50.5	32.4	36.4	40.0
	2.4	2.5	2.5	2.2	6.5	6.6	3.7	3.6
20	59.3	70.4	70.2	53.6	74.1	------	57.9	62.8
	5.4	4.1	5.5	3.8	9.1		5.9	5.6
50	102.4	126.6	124.5	98.6	123.0	------	98.6	109.6
	11.9	7.8	11.2	8.1	15.9		10.0	9.8
200	------	------	------	------	------	------	------	------
Maximum:	886	533	763	299	374	539	263	269

Table 3, *cont.* Lead widths (m) and standard deviations (below) in the northeastern Canada Basin data by region, maximum draft (cm), minimum width (m). Also given are the maximum lead widths encountered. No statistics are given if fewer than 20 leads were found in a region.

MAX DRAFT/ MIN WIDTH	REGION I	J	K	L	M
30 / 3	116.9	9.6	10.2	------	5.4
	100.8	4.9	2.4		1.7
20	------	------	------	------	------
50	------	------	------	------	------
200	------	------	------	------	------
Maximum:	2181	153	83		42
70 / 3	30.8	14.4	17.6	8.7	15.9
	16.1	2.0	3.3	1.3	4.2
20	132.8	62.5	65.8	------	------
	81.4	9.3	13.7		
50	------	------	------	------	------
200	------	------	------	------	------
Maximum:	2274	234	342	72	510
100 / 3	28.7	17.9	18.8	9.4	16.5
	12.1	2.1	2.7	1.1	4.5
20	104.6	61.6	68.8	------	84.7
	52.9	7.4	10.8		29.9
50	------	------	------	------	------
200	------	------	------	------	------
Maximum:	2280	239	348	81	792

Table 4. Lead spacings in the QUEENFISH data, by region, maximum draft (cm), minimum width (m). S=mean spacing (m) with standard deviation below, N=number of leads per kilometer. Also given are the maximum spacings encountered. No statistics are given if fewer than 20 leads were found in a region.

MAX DRAFT/ MIN WIDTH		REGION A	B	C	D	E	F	G	H
30 / 3	S:	462.9	428.5	929.9	739.4	685.9	------	2190.9	2551.0
		39.9	41.7	118.9	82.2	155.1		402.5	759.2
	N:	2.01	2.16	1.06	1.31	1.38		0.45	0.33
20	S:	1240.1	1014.0	2821.6	1897.2	1061.8	------	------	------
		150.1	125.6	601.9	307.5	240.6			
	N:	0.73	0.92	0.31	0.51	0.90			
50	S:	2552.6	2351.2	------	5493.8	------	------	------	------
		318.7	503.1		1436.6				
	N:	0.36	0.41		0.17				
200		------	------	------	------	------	------	------	------
Maximum:		4893	5842	9321	8594	7062		13523	24321
70 / 3	S:	339.7	369.8	364.1	513.0	504.7	553.1	859.6	737.7
		24.9	30.2	34.6	41.2	102.8	108.2	100.1	61.9
	N:	2.67	2.35	2.56	1.83	1.82	1.70	1.10	1.14
20	S:	783.2	568.2	926.6	1050.0	816.9	983.4	1775.5	1230.3
		70.6	50.3	97.9	102.5	173.1	221.0	264.0	131.4
	N:	1.16	1.53	1.02	0.91	1.14	0.98	0.54	0.67
50	S:	1818.8	1238.0	2935.7	3226.0	1868.1	------	3757.9	3029.1
		190.6	150.4	621.9	577.5	515.6		1200.8	653.3
	N:	0.50	0.73	0.33	0.29	0.48		0.22	0.27
200		------	------	------	------	------	------	------	------
Maximum:		3807	4792	4777	4488	6782	4996	6221	3304
100 / 3	S:	238.1	213.4	225.5	416.3	443.2	421.6	837.0	722.0
		14.8	13.1	17.9	31.5	88.4	84.4	97.6	72.3
	N:	3.73	3.93	3.86	2.24	2.04	2.20	1.13	1.31
20	S:	597.7	416.5	581.6	866.6	705.2	------	1587.7	1321.9
		46.4	33.7	59.9	78.7	147.0		227.5	213.0
	N:	1.51	2.05	1.54	1.09	1.30		0.60	0.72
50	S:	1468.9	1064.2	1449.1	2465.7	1591.7	------	3603.1	3251.1
		157.0	126.1	261.8	348.7	397.6		1158.5	723.5
	N:	0.61	0.83	0.63	0.37	0.60		0.23	0.29
200		------	------	------	------	------	------	------	------
Maximum:		2897	2808	3628	4478	6779	4993	6218	8918

Table 4, *cont.* Lead spacings in the northeastern Canada Basin data, by region, maximum draft (cm), minimum width (m). S=mean spacing (m) with standard deviation below, N=number of leads per kilometer. Also given are the maximum spacings encountered. No statistics are given if fewer than 20 leads were found in a region.

MAX DRAFT/ MIN WIDTH		REGION I	J	K	L	M
30 / 3	S:	3381.9	4567.3	2477.4	------	2996.1
		1500.2	2495.0	913.9		1948.1
	N:	0.15	0.22	0.36		0.17
20		------	------	------	------	------
50		------	------	------	------	------
200		------	------	------	------	------
Maximum:		23429	71342	42161		37059
70 / 3	S:	994.4	700.1	928.5	1763.9	911.1
		229.6	129.7	159.7	449.3	169.6
	N:	0.96	1.37	1.01	0.53	1.07
20	S:	4476.4	4587.8	4479.7	------	------
		1396.3	1513.8	1513.3		
	N:	0.19	0.21	0.20		
50		------	------	------	------	------
200		------	------	------	------	------
Maximum:		24918	13508	10022	25355	14562
100 / 3	S:	739.6	585.6	635.4	858.2	709.5
		130.6	73.9	89.7	197.8	110.9
	N:	1.28	1.65	1.53	1.09	1.36
20	S:	2896.8	2765.0	2860.5	------	4493.1
		795.8	623.6	608.4		1214.4
	N:	0.29	0.35	0.31		0.19
50		------	------	------	------	------
200		------	------	------	------	------
Maximum:		12353	7298	10022	25212	11154

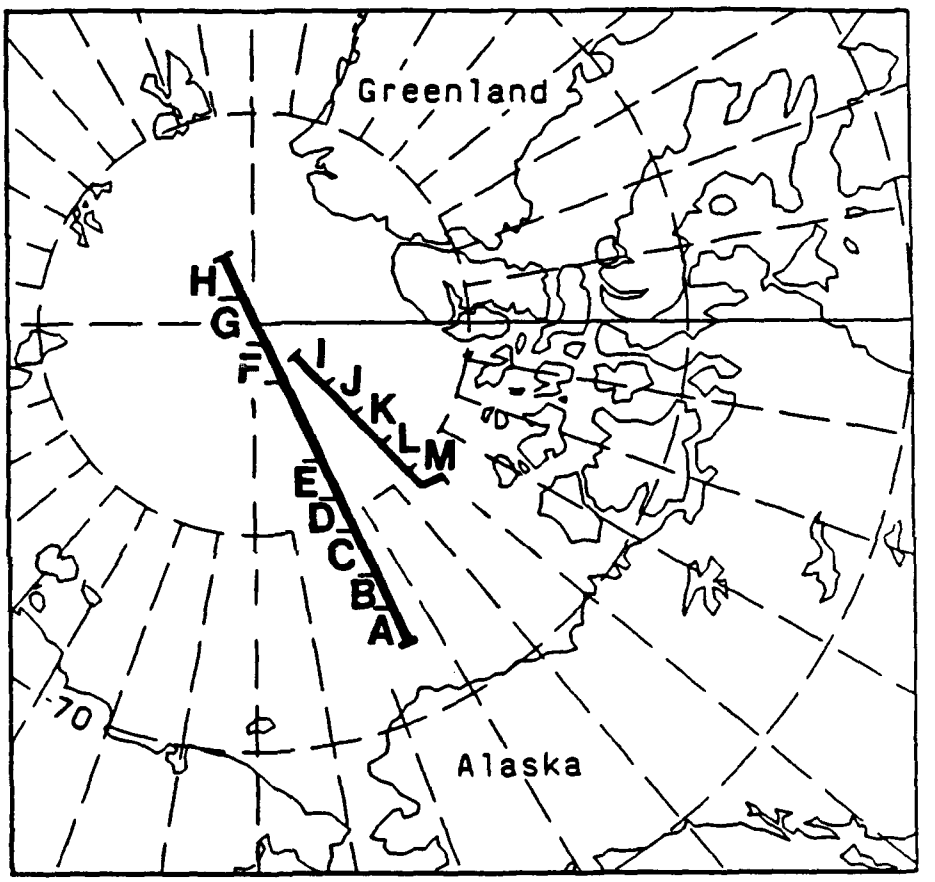

Figure 19. Sonar transect locations through the central Canada Basin (August 1970) and northeastern Canada Basin (October 1978).

A methodology has been developed for estimating width distributions of linear features from measurements along a transect through a network of such features. Both isotropic and anisotropic orientations of the linear features have been considered. In the anisotropic case, the distribution of orientations of the lines must be known. In both cases if the distribution of true widths and the orientations are viewed as independent random variables then the true width distribution can be determined from the apparent widths and vice versa. Furthermore, if the true widths and the orientations vary jointly then the apparent width can be determined from the joint distribution. The geometry used in the development of the statistical model is shown in Figure 20. Also shown is an example of the error distribution function (the difference between the true and apparent lead widths) for transects taken nearly parallel to the preferred orientation mean and another perpendicular to the mean orientation of leads in the Landsat image of Figure 10.

"True" lead width distributions in both submarine sonar and Landsat imagery have been determined and apparent widths measured along transects were obtained. In the imagery it was found that lead orientations were not uniform, and width distributions generally followed the negative exponential model although considerable variation was observed. The width distributions measured from submarine sonar illustrated that the general shape is similar to those derived from overhead imagery, but that the errors in widths can be significant. Of course, this potential error is not an issue if adequate two-dimensional data are available. For example, side-scan sonar will permit a more accurate retrieval of lead and keel statistics, although processing such data introduces a new set of problems. Sonar data with concurrent overhead imagery from aircraft or satellite is also a potentially valuable source of information. However, lead width distributions derived from satellite data may not be accurate since very small leads are not resolved. This is particularly true for medium resolution data such as that from the DMSP or the AVHRR. One solution might be to retrieve the orientation information from satellite data where small lead widths cannot be resolved, and the width information from submarine sonar transects. Aircraft using a laser profilometer would be analogous to the sonar transects. Unfortunately, it is not possible to determine the actual error in lead widths derived from much of the archived sonar data. However, if lead "climatologies" can be compiled for various locations and seasons, or if significant relationships between lead orientation and geostrophic winds can be developed, then at least we can determine the probable error.

Other applications of this procedure are possible. For example, the formalization would be the same for lead and keel spacing distributions and their associated errors. An application similar to that of the sonar transect concerns sampling strategies. Lead widths can be sampled along a transect in satellite imagery or aerial photos, and this sample can then be used to infer the characteristics of the true distribution. A similar application involves large-scale estimates of heat flux. Heat flux through leads is in part a function of fetch, and fetch is a function of the true lead width and the crossing angle of the wind. If the wind direction is constant as it travels across the network of leads, then the distribution of fetches can be determined from the distribution of true lead widths as presented in the previous sections.

The entire procedure is detailed in the Attachment.

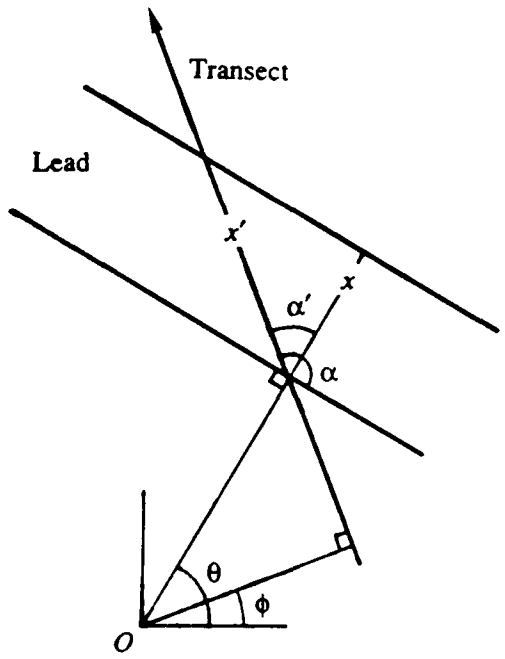

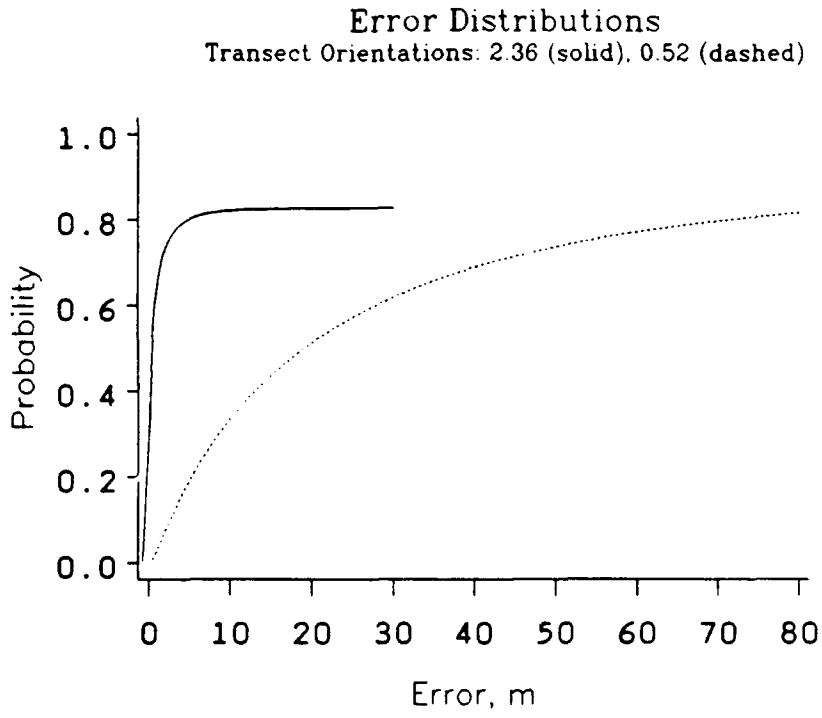

Figure 20. TOP: Lead and transect geometry used to estimate the distribution of errors in lead width measurements when made along a transect; i.e., with submarine sonar. BOTTOM: The error distributions are shown for two different transects across a lead network that exhibited a preferred orientation: one oriented almost parallel to the mean lead orientation and the other almost perpendicular.

I.5.2 *Lead Fractional Area Coverage Measured Along a Transect*

In the previous section sea ice leads were modeled as a Poisson line process and a method was was presented for estimating the "actual" lead width distribution from a width distribution measured along a transect (the "apparent" lead width distribution). The purpose of this section is to extend that work to the estimation of the fractional area coverage of leads from measurements along a line. This line could be a submarine transect under the ice or on a satellite image. Two methods from stochastic geometry are presented although applications have not yet been performed. While the problem is illustrated with respect to sea ice leads it should be noted that the general lineal method described here is applicable to any geophysical parameter with known (or determinable) spatial structure.

I.5.2.1 *Method for a Poisson Line Process*

If in fact leads can be accurately modeled as a Poisson line process then one approach to estimating the area fraction is to use the lead width distribution [*Miles*, 1964]:

$$p' = Prob[O \text{ is covered}] = 1 - e^{-\tau w} \tag{1}$$

where O is an arbitrary origin and τ is the density of the process. The overall mean line (lead) thickness (width), w', is defined as

$$w' = \pi^{-1} \int_0^{\pi} w'(\theta)\, d\theta$$

where $w'(\theta)$ is the mean thickness of lines with orientation θ ($0 \le \theta \le \pi$). This applies to lines oriented isotropically; i.e., with a uniform distribution: $f_\Theta(\theta)=\pi^{-1}$ where f_Θ is the probability density function for lead (line) orientations. For anisotropic thick lines then

$$w' = \int_0^{\pi} w'(\theta)\, dF_\Theta(\theta)$$

where $dF_\Theta(\theta) = f_\Theta(\theta)\, d\theta$, and F_Θ is the cummulative distribution function for orientations. The lead width distribution can be determined as in *Key and Peckham* [1991].

I.5.2.2 *General Lineal Method*

The general expression for the estimate of the fractional area coverage, p', of a geophysical parameter whose actual fractional coverage is p, regardless of the the spatial structure of that parameter is

$$p' = \mu_U^{-1} \int_U I(x)\, dx$$

The factor μ_U is needed for normalization and depends on the shape of the structuring element U; for example it may be the length of a line or the area of a square. The indicator function $I(x)$ for the underlying function $q(x)$ at coordinate vector location x is 1 if $q(x)$ satisfies some condition and 0 otherwise.

The expected value of p' is p and its variance is

$$p' = E(p'-p)^2 = \mu_U^{-2} \int_U \int_U k_I(\|x-y\|)\, dx\, dy$$

where k_I is the autocovariance function of the indicator function I [*Stoyan et al.*, 1989].

For measurements along an array of n parallel lines the corresponding expressions are

$$\begin{aligned} p' &= \frac{L}{nl} \\ var(p') &= (nl)^{-2} \int_{nl} \int_{nl} k_I(\|x-y\|)\, dx\, dy \end{aligned} \tag{2}$$

where L is the total length of lines each of length l.

Exponential covariance, as described in the previous section, is used here:

$$k_I(r) = p(1-p)\, e^{-\alpha r} \quad (r, \alpha \geq 0) \tag{3}$$

where α describes the dependence of the covariance on the vector distance $r=\|x-y\|$. Implicit in this expression is that $q(x)$ is isotropic.

For a Poisson line process $\alpha=2\tau/\pi$ [*Stoyan et al.*, 1989, pg. 178; *Miles*, 1964] and the estimation variance is approximately

$$var(p') \approx \frac{2p(1-p)\left(1-\frac{1}{\alpha l}\right)}{n\alpha l}$$

These models are currently being applied to real and simulated satellite data. Results will be presented in the next report.

Part II: RADIATIVE TRANSFER MODELING STUDIES

II.1 RADIATIVE TRANSFER STUDIES IN LEAD DETECTABILITY

II.1.1 *Radiative Transfer Modeling and Model Validation*

In order to utilize radiative transfer models most effectively, we have reviewed how they treat factors such as ice cloud morphology, cloud optical thickness, low level inversions, boundary layer effects, and other aspects relevant to the polar regions. A particular concern is that existing models, cloud properties, standard atmospheres, etc. have typically been developed for low and mid-latitude applications, and may thus contain biases or shortcomings when applied to polar regions. Part of this effort involves incorporating polar atmospheres and cloud properties into the models. Arctic-specific temperature and humidity profiles have been obtained and are discussed in the next section. Unfortunately, little information on the microphysical characteristics of arctic clouds is available. Data that are available, however, are being incorporated into the models where appropriate. This is limited primarily to arctic stratus experiments during the early 1980's, and some measurements of aerosols. Additional data is expected to be obtained during LEADEX by instruments on the NOAA P-3.

Work described in this part of the report relies heavily on simulating radiances measured by the AVHRR sensor. To simulate radiances in the AVHRR thermal channels, daily temperature and humidity profiles in each season are used with the LOWTRAN 7 radiative transfer model [*Kneizys et al.*, 1988]. Radiances are modeled for sensor scan angles from 0° to 60° in 10° increments. The appropriate sensor response function is applied to the calculated radiances, and radiances are then converted to brightness temperatures. Atmosperic chemical composition, background tropospheric and stratospheric aerosols for the subarctic winter and summer models are used, since no such information is available from the ice islands. The optical properties of Arctic haze have not been extensively measured; model calculations [*Blanchet and List*, 1983] show that the volume extinction coefficient of Arctic haze is generally of the same order of magnitude as that of the tropospheric aerosols. Therefore, the use of tropospheric background aerosols is appropriate.

In order to test some sense of the validity of the radiative transfer model, downwelling longwave irradiances (fluxes) computed with LOWTRAN were compared to measurements at South Pole, Greenland and Denver. Radiosonde data from the three locations were used for the calculations. To obtain irradiance, E, from LOWTRAN (which outputs radiances, L) the calculation was done for four angles (8 streams) and employed the weighting function:

$$E = \pi(0.3626838L_1 + 0.3137066L_2 + 0.2223810L_3 + 0.1012285L_4)$$

where the subscripts of L refer to the sensor zenith angles 79.430°, 58.296°, 37.187°, and 16.201°, respectively. Additionally, a single-angle method (52.5°) was tested and found to give fairly accurate results. The bandwidth of 3.5 - 50 μm used in the calculations corresponds with the bandwidth in which a pyrgeometer measures.

The LOWTRAN irradiances differed from the measurements by -4.7% to +5.6% . Assuming 5% accuracy for the pyrgeometer data these results are acceptable. Results for clear sky are listed in Table 5.

Table 5. Comparison between modeled and observed longwave fluxes under clear sky conditions.

Station and Date	Measured ($W\ m^{-2}$)	4 Angles ($W\ m^{-2}$)	Error (%)	52.5° ($W\ m^{-2}$)	Error (%)
Denver, 9-30-89	334	336	+0.60	320	-4.19
South Pole, 12-28-86	128	124	-3.13	117	-8.60
South Pole, 7-31-86	71	75	+5.63	71	0.0
South Pole, 11-6-86	107	102	-4.67	96	-10.28

Calculations were also done for cloudy sky conditions. In comparisons of model results and observations, the observed cloud fraction, A_c, must be considered. Here the model is used to estimate clear and overcast fluxes, and these are weighted by the observed cloud fraction.

A remaining problem concerns the differences between the microphysical properties of LOWTRAN's cloud models and those of the observed clouds, which are unknown. Table 6 gives the results of the cloudy sky comparisons.

Table 6. Comparison between modeled and observed longwave fluxes under cloudy conditions.

Station and Date Cloud Fraction, Type	Measured ($W\ m^{-2}$)	4 Angles ($W\ m^{-2}$)	Error (%)	52.5° ($W\ m^{-2}$)	Error (%)
Greenland, 7-23-90; 8/8, stratocumulus	309	301	-2.59	301	-2.59
Greenland, 7-26-90 3/8, stratocumulus	283	282	-0.35	275	-2.48
Greenland, 7-1-90 1/8, cirrus	225	227	+0.89	217	-3.56
South Pole, 7-16-86 8/8, cirrus	157	156	-0.64	156	-0.64
South Pole, 11-26-86 8/8, cirrus	126	129	+2.38	122	-3.17

To examine the effect of vertical temperature structure on upwelling longwave radiation, radiances in the three channels were estimated using arctic mean and subarctic standard winter and summer profiles (described below) with identical seasonal surface temperatures. The maximum difference in radiances was 0.05 W m^{-2} sr^{-1} indicating that the vertical temperature distribution of the relatively dry arctic atmosphere plays a very small role in the attenuation of upwelling longwave radiation.

II.1.2 *Ice Island Data*

Analyses are based on atmospheric temperature and humidity profiles collected by rawinsonde from a Soviet ice island (NP-26), located at approximately 85° N 170° W during 1983-1987 (Figure 21). Generally two observations per day were collected covering a vertical range of 0-25 km. Profiles that have at least 10 levels are retained in the analysis. Observations include temperature, dew point depression, wind speed, and wind direction. For the years 1986-87 surface-based cloud observations are also available. These observations include low, middle, and high cloud types, height of the cloud base, and cloud fraction.

Only clear sky profiles are of interest in one of the studies below, and since the satellite thermal radiances under cloudy conditions will reflect cloud top temperature and a significant amount of cloud cover will affect the lower tropospheric temperature structure, clear sky "seasons" that differ in their vertical temperature and humidity structures are then defined. The seasons are determined objectively with a squared Euclidean distance clustering algorithm; the variables are temperature and humidity at each level. To reduce the degree of statistical dependence between levels, only one measurement per kilometer was used. The resulting seasons are winter: October through March, summer: June through August, and transition: April, May, and September. The resulting mean seasonal temperature profiles for clear, cloudy (greater than 75% cloud cover), and mixed conditions are shown in Figure 22.

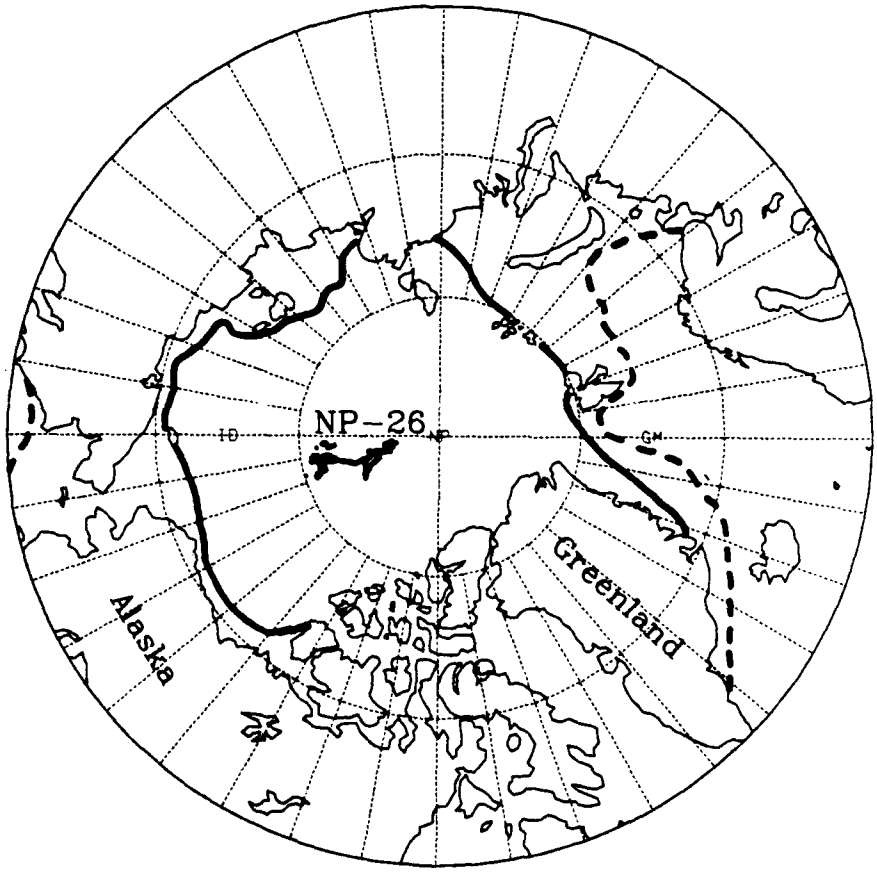

Figure 21. **Average minimum (solid) and maximum (dashed) sea ice extent in the Arctic Ocean. Also shown is the area covered by the NP-26 drifting ice island.**

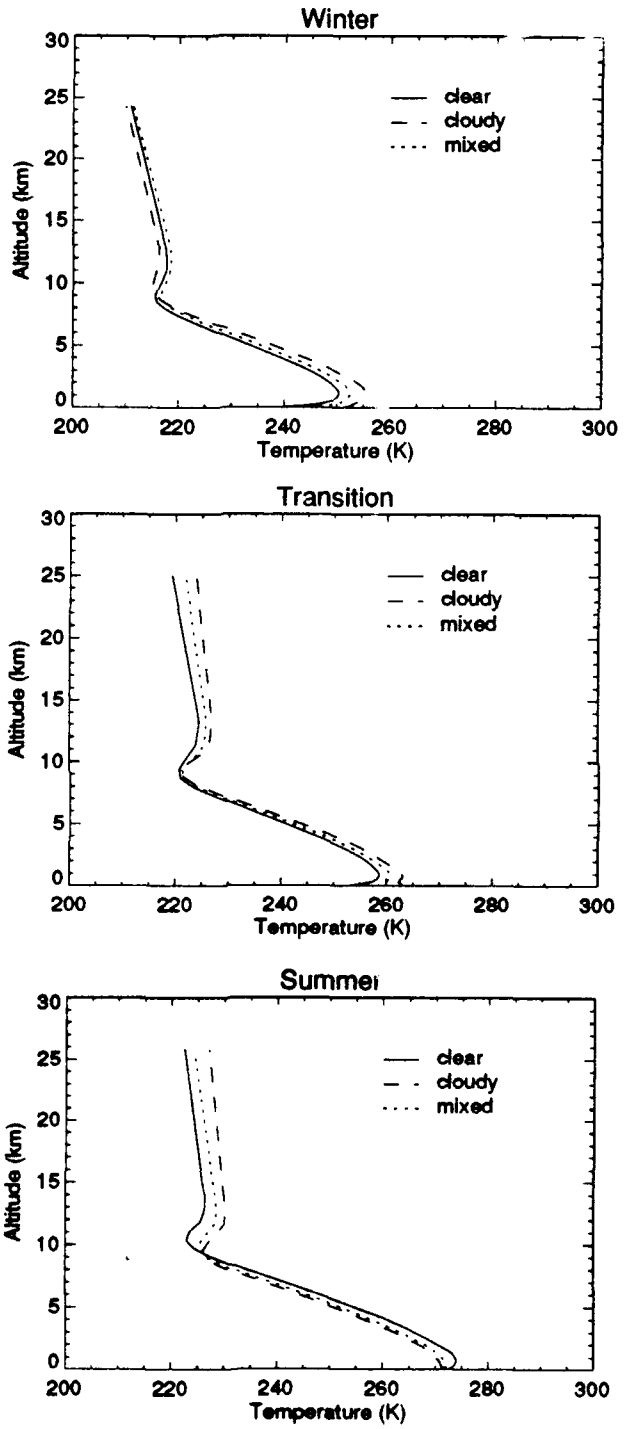

Figure 22. Arctic winter, transition, and summer temperature profiles under clear, cloudy, and mixed conditions from a Soviet ice island located in the Canada Basin.

II.1.3 *Contrast Studies*

Atmospheric and view angle effects are modeled under a variety of conditions to simulate sensor response in order to gain a better understanding of how leads might appear in the satellite data under varying surface and atmospheric conditions. With this knowledge, it may be possible to estimate the smallest resolvable lead under a given set of surface/atmospl c/sensor resolution and view angle conditions. Emphasis is on the AVHRR thermal channels (3: centered at approximately 3.7 μm, 4: 11 μm, 5: 12 μm).

LOWTRAN calculations using the data and methodology described above were made over a range of 0.55 micron optical depths for three prescribed surface temperatures used to characterize different lead types (open or refrozen) and a fourth to represent the "background" scene consisting of 2 m thick multiyear ice. These temperatures were estimated using a surface energy balance approach [*Maykut*, 1982] to characterize the open leads at 271 K, leads covered by 5 cm thick ice (257 K) and 15 cm thick ice (248 K). The multiyear ice has a skin temperature of 235 K in all model calculations. The model was run for satellite viewing angles of 0° (nadir), 20° and 50° and accounted for differences in directional emissivity at each central wavelength of the AVHRR channels. Temperature and humidity profiles were based on the mean January ice island soundings. All simulated radiances were converted to brightness temperatures for ease of analysis and intercomparisons.

Examples of the results are shown in Figure 23 for three commonly observed conditions in the Arctic, ice crystal precipitation and haze in the boundary layer and high-level cirrus. Figures 23a, 23c, and 23e are composites of results at 0° viewing angle showing the behavior of channel brightness temperatures (numbered 3, 4 and 5 on the plots) for simulations assuming each of the surface temperatures defined above. Figures 23b, 23d, and 23f show results for a satellite angle of 50°. A hypothetical cirrus cloud of varying optical depth was inserted in the lowest 1 km of the atmosphere to simulate the effects of "ice crystal precipitation" which is a common feature affecting the radiative balance of the lower troposphere in the Arctic. Regardless of the underlying surface type the simulated brightness temperatures rapidly converge to the 248 K blackbody radiating temperature of the "cloud top" level as optical depth increases. Note that because all three channels are centered in window regions of the spectrum, surface temperatures are well simulated at zero optical depths. Maximum brightness temperature differences exist between the channels at around optical depth 0.5 to 0.8. If satellite radiances can be measured accurately, these differences may be used to delineate leads when optically thin ice crystal precipitation is present in the boundary layer, but brightness temperature differences and contrast between surface types is rapidly diminished as the optical depth increases beyond about 1.0, making it impossible to detect the underlying leads. This value is not at all unexpected as ice crystal precipitation optical depths of up to 20 have been reported [*Curry et al.*, 1990].

Figures 23c,d show the results assuming that a haze layer exists from the surface to a altitude of 2 km (the boundary layer aerosol model defined in LOWTRAN) over the same range of optical depths. Also shown in Figures 23g,h are the brightness temperatures for aerosols

(haze) during the day when channel 3 exhibits a significant contribution from reflected solar radiation. Multiple scattered solar radiation adds significantly to the upwelling radiances as optical depths of the haze layer increase while the infrared channels do not show any multiple scattering effects. All other input parameters to LOWTRAN are the same as for Figure 23a. In the haze simulations it is obvious that the brightness temperature differences between channel pairs are small when only thermal radiances are considered (nighttime) over the entire range of optical depths while large differences exist between channel 3, and channels 4 or 5 when solar radiation is accounted for during the day. Also, the contrast between surface types for each channel remain significant over the range of visible optical depths shown, particularly when only thermal radiances are considered. Gross differences between Figures 23a,b and 23c,d are due to markedly different properties of the haze and cirrus models defined for LOWTRAN.

The contrast between varying lead types and the multiyear ice pack can be expressed by the difference in simulated channel brightness temperature for a hypothetical lead temperature, say open water, 5 cm thick ice or 15 cm thick ice and the surrounding ice pack at any optical depth, normalized by the brightness temperature of the ice pack (here taken to be 2 m thick). Figures 24a-f show the normalized contrast for channel 4 assuming the conditions illustrated in Figures 23a-f. This relative measure of contrast may provide a means to detect leads using AVHRR data even at night, though it is apparent that if optically thick ice crystal precipitation exists that the contrast is essentially zero making it impossible to detect leads using such a method.

For cirrus clouds brightness temperatures again converged at the blackbody radiating temperature at cloud top for large optical depths, but the convergence was less dramatic than in the case of low level ice crystal precipitation. Channel 3 minus channel 4 brightness temperature differences at 50° viewing angle (not shown) were significant in this case reaching nearly 12 K over open leads at a 0.55 micron optical depth of about 2.6 with the difference being less than 5 K over the pack ice. Differences in these signatures when incorporated into image analysis algorithms in conjunction with ancillary information should be very useful in the detection of leads. Though the normalized contrast between surface types degrades with increasing cirrus optical depth, our simulations indicate that reasonable signatures should be detectable for a range up to about optical depth 4.0, that is, for most cirrus conditions expected to be observed in the Arctic region.

Combining brightness temperature differences with contrast will improve our ability to detect leads significantly. Developing an algorithm to do so presents a challenge for the future.

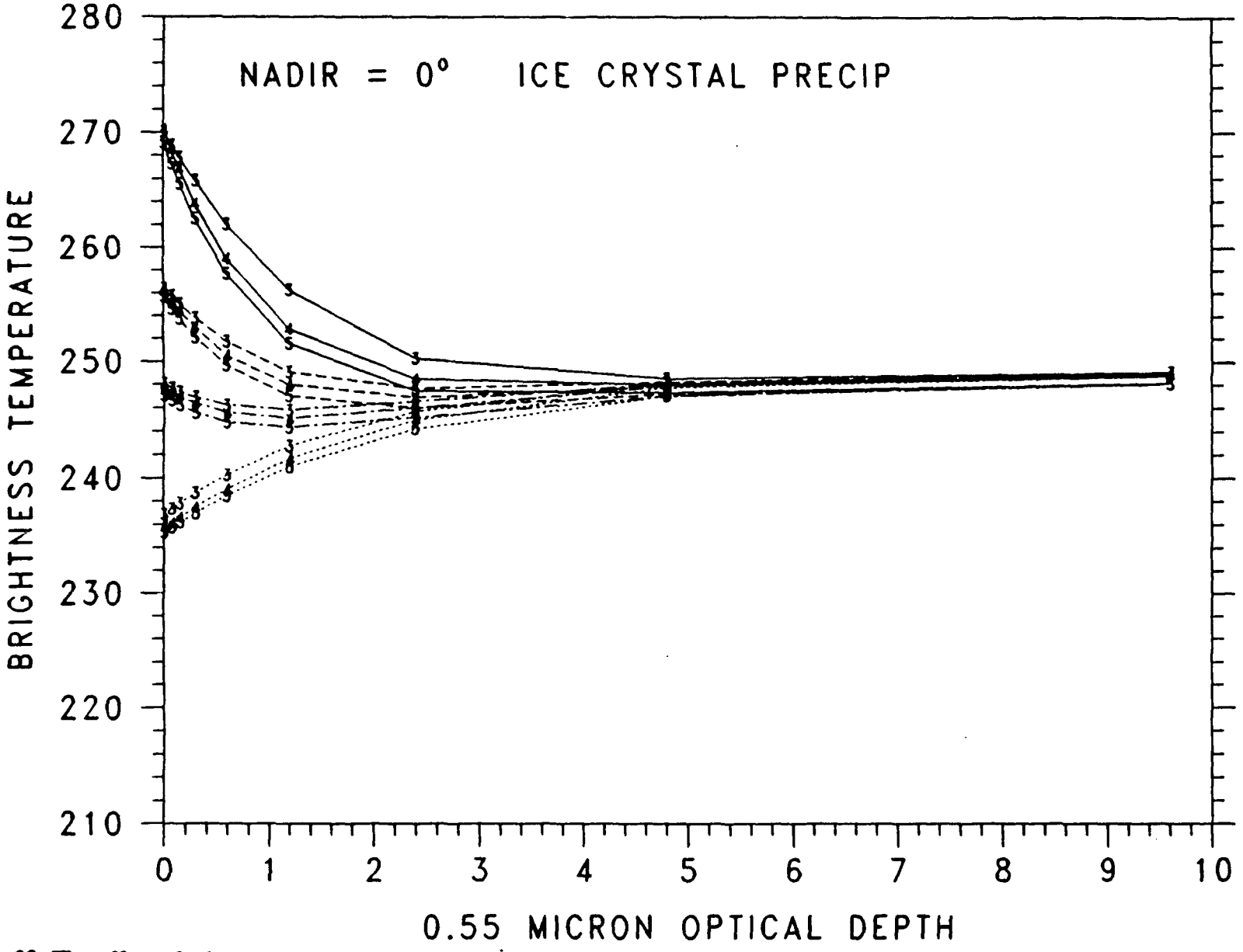

Figure 23. The effect of a layer of ice crystal precipitation, boundary layer haze, and high-level cirrus cloud on the three AVHRR thermal channels (3, 4, 5) at satellite view angles of 0° (a,c,e,g) and 50° (b,d,f,h). Optical depths (0.55 μm) are varied from 0 to 10. The tops of the ice crystal and haze layers are near the top of the inversion at a temperature of approximately 248 K. The brightness temperature change in each channel over each of the four surface types (ice thicknesses: 0, 5, 15, 200 cm from top to bottom) can readily be seen. Also shown (g,h) are the brightness temperatures for aerosols (haze) during the day when channel 3 exhibits a significant contribution from reflected solar radiation.

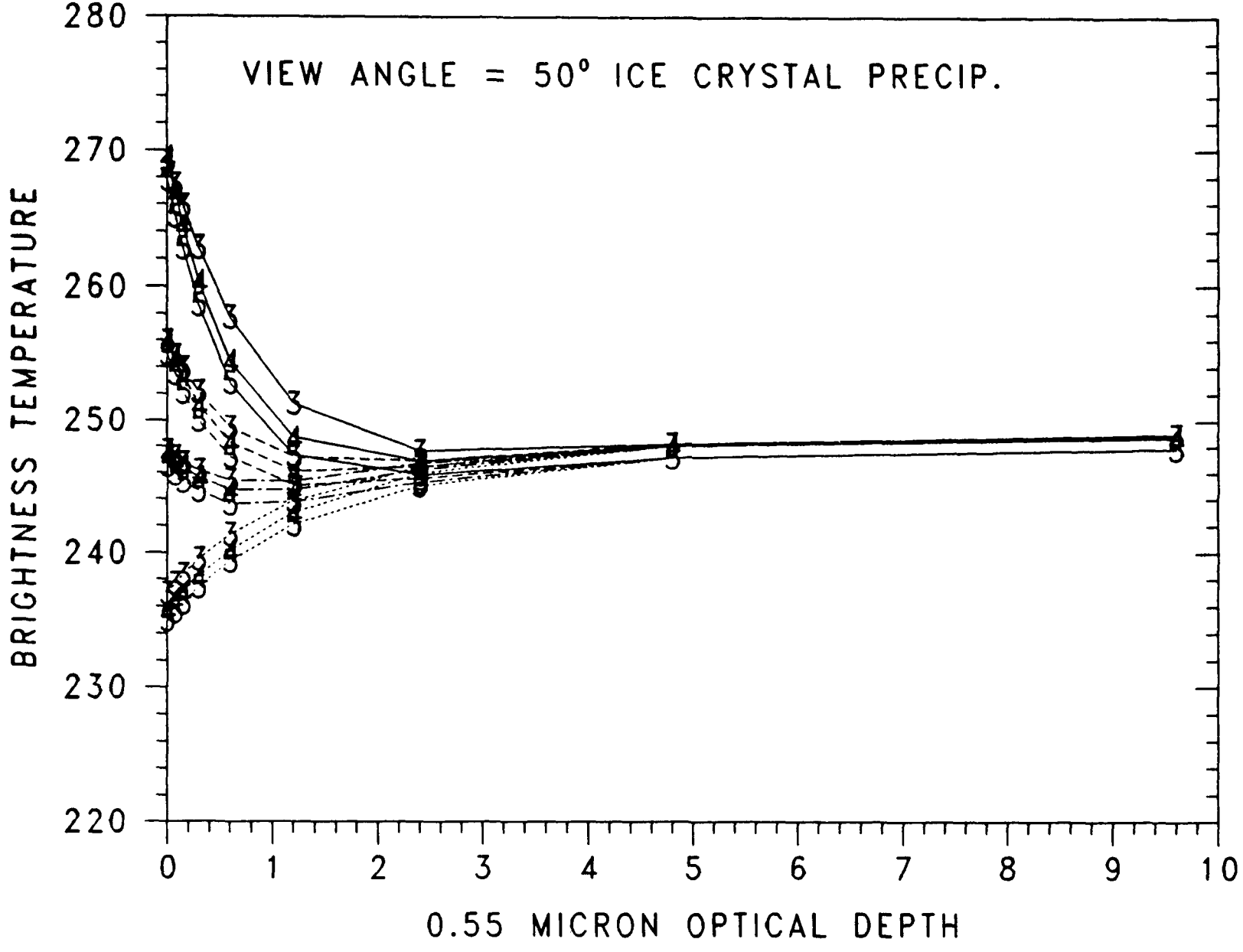
VIEW ANGLE = 50° ICE CRYSTAL PRECIP.
BRIGHTNESS TEMPERATURE
280
270
260
250
240
230
220
0
1
2
3
4
5
6
7
8
9
10
0.55 MICRON OPTICAL DEPTH

Figure 23b.

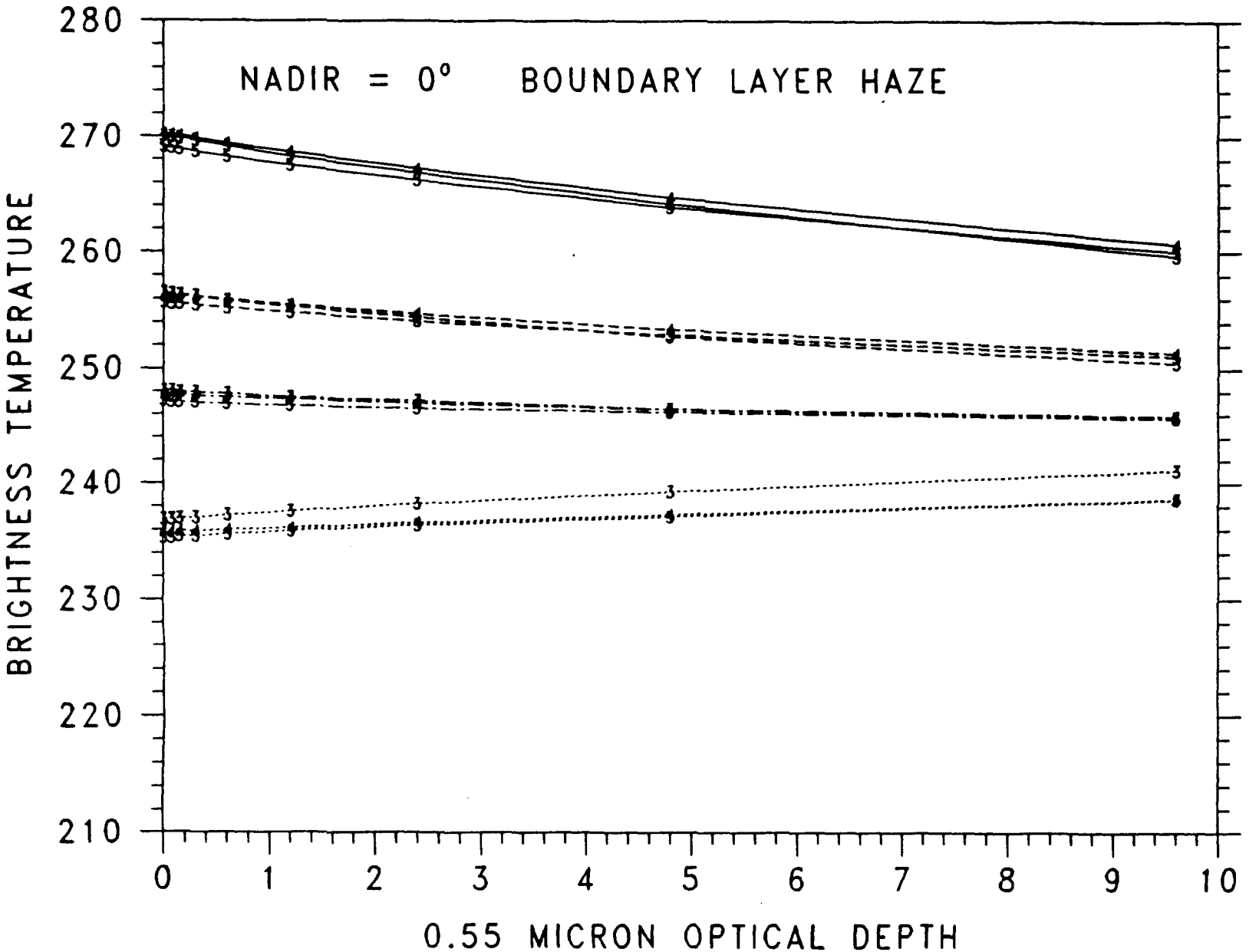
NADIR = 0° BOUNDARY LAYER HAZE
BRIGHTNESS TEMPERATURE
280
270
260
250
240
230
220
210
0
1
2
3
4
5
6
7
8
9
10
0.55 MICRON OPTICAL DEPTH

Figure 23c.

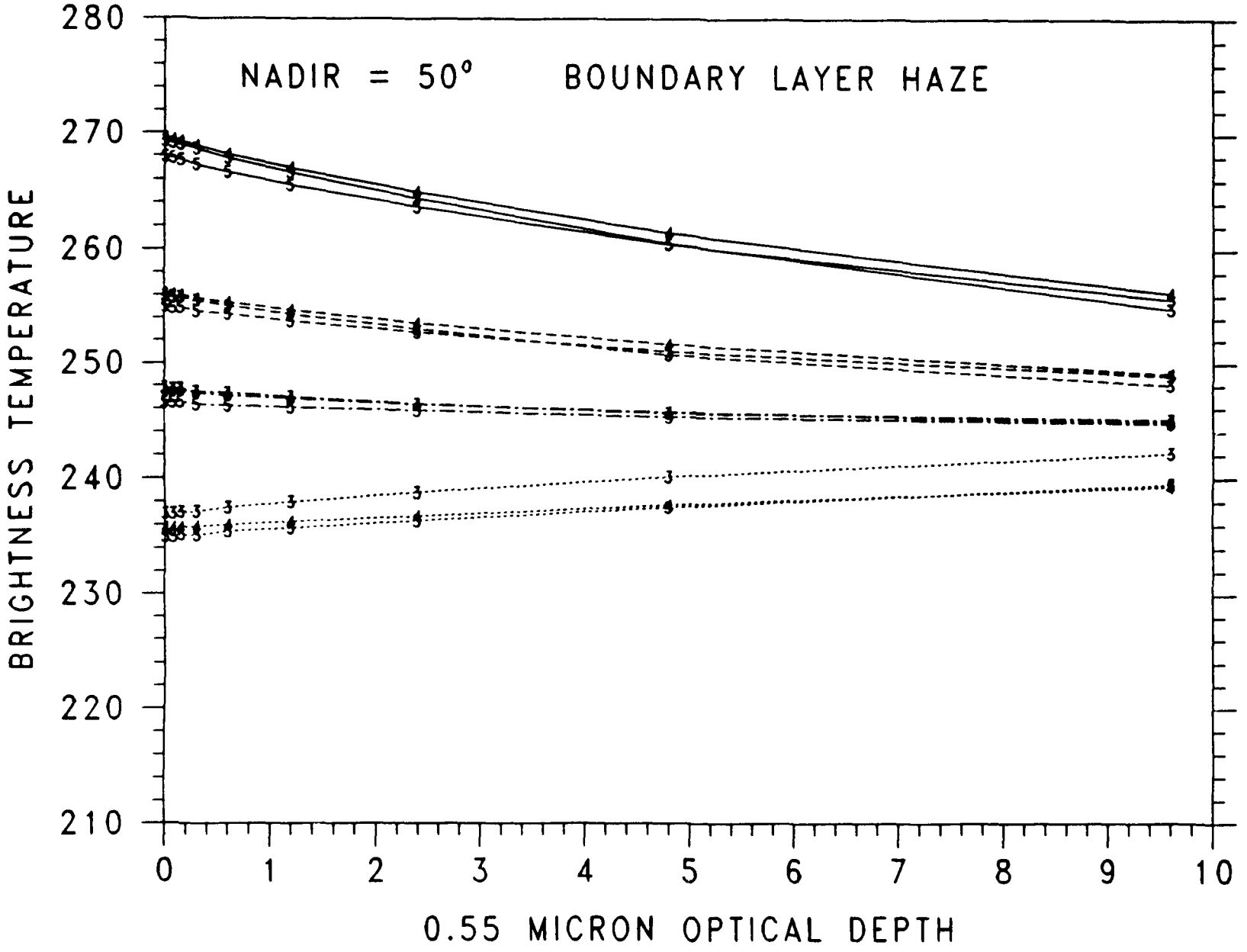
NADIR = 50°
BOUNDARY LAYER HAZE
BRIGHTNESS TEMPERATURE
280
270
260
250
240
230
220
210
0
1
2
3
4
5
6
7
8
9
10
0.55 MICRON OPTICAL DEPTH

Figure 23d.

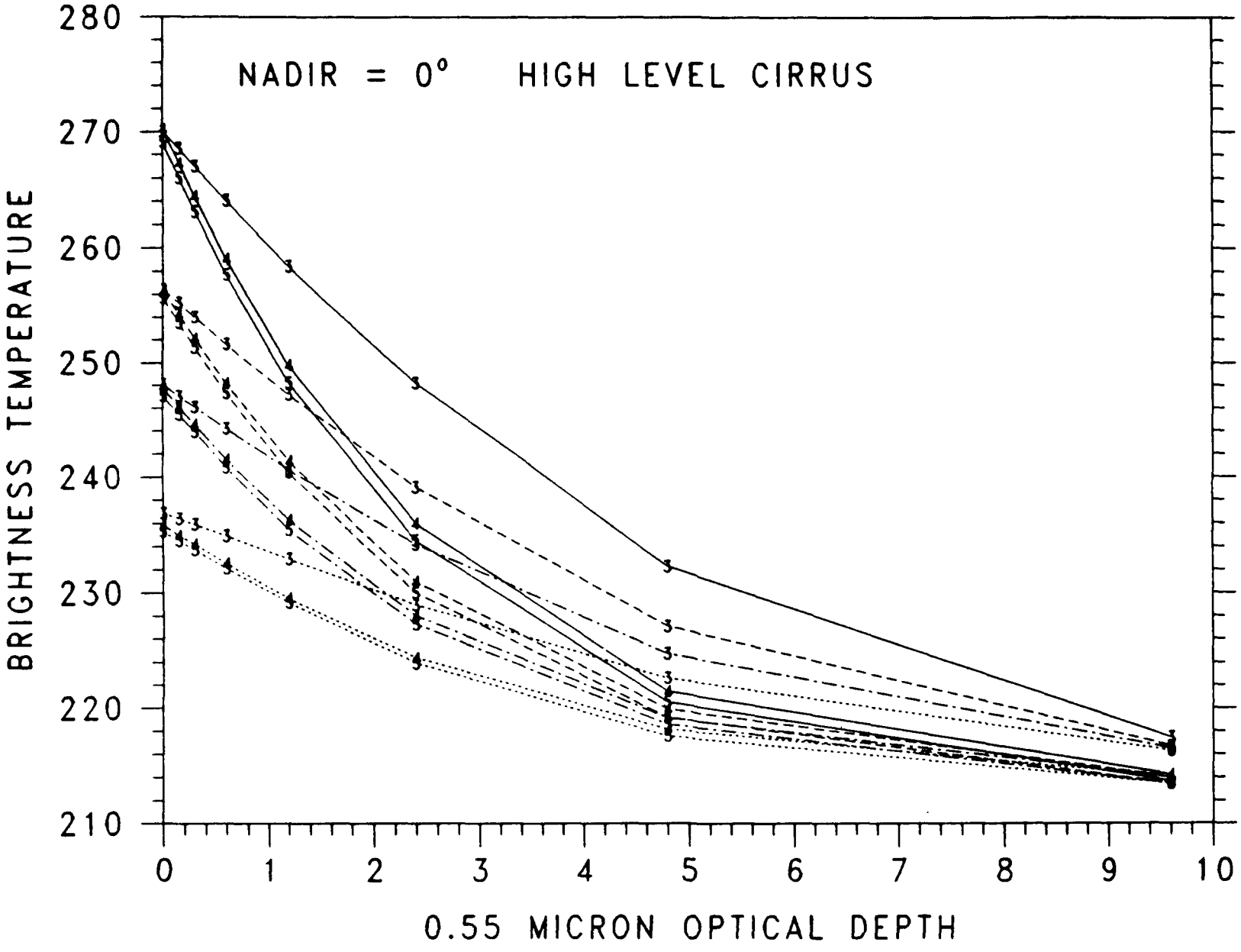
NADIR = 0° HIGH LEVEL CIRRUS
BRIGHTNESS TEMPERATURE
280
270
260
250
240
230
220
210
0
1
2
3
4
5
6
7
8
9
10
0.55 MICRON OPTICAL DEPTH

Figure 23e.

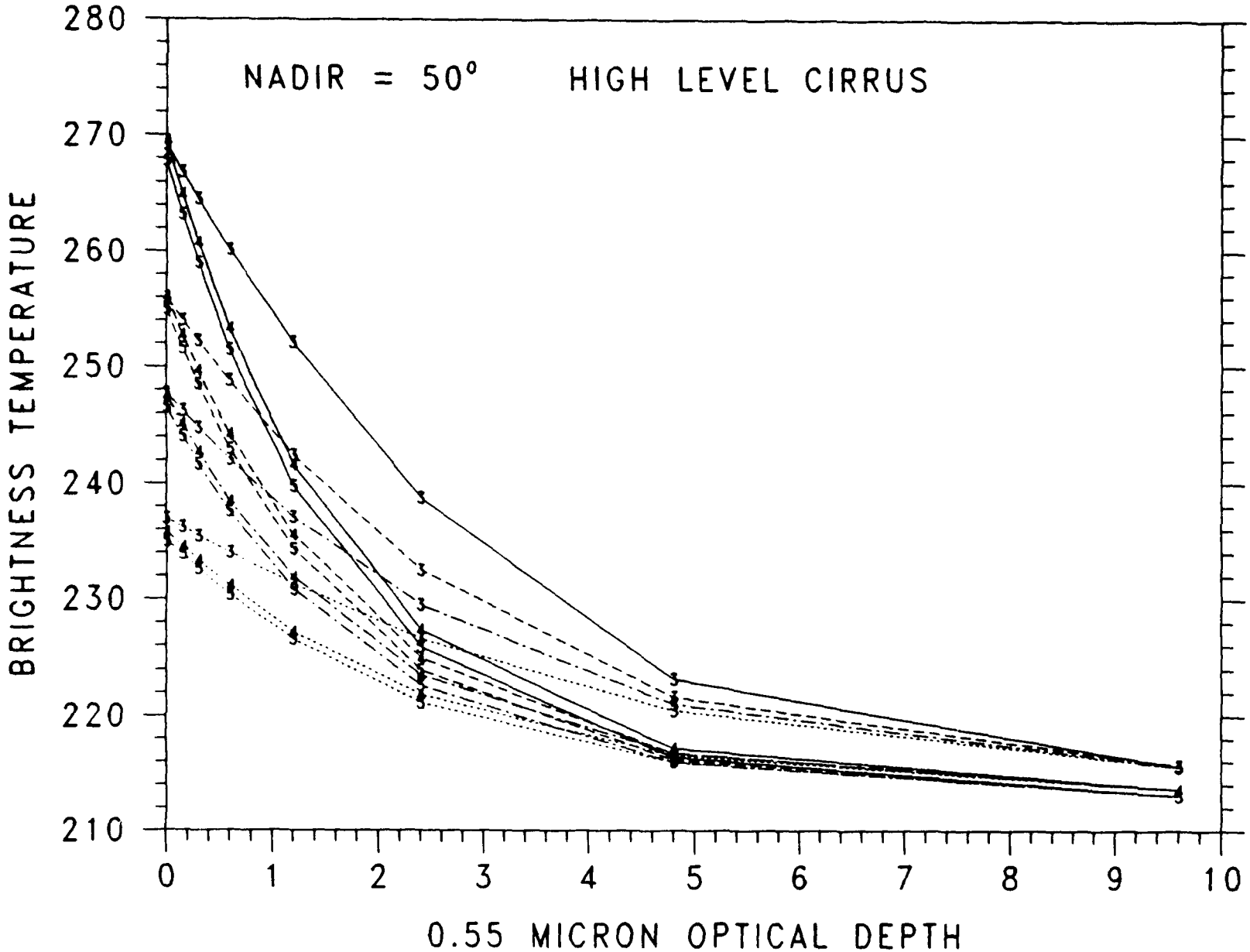
NADIR = 50°
HIGH LEVEL CIRRUS
BRIGHTNESS TEMPERATURE
280
270
260
250
240
230
220
210
0
1
2
3
4
5
6
7
8
9
10
0.55 MICRON OPTICAL DEPTH

Figure [illegible]f.

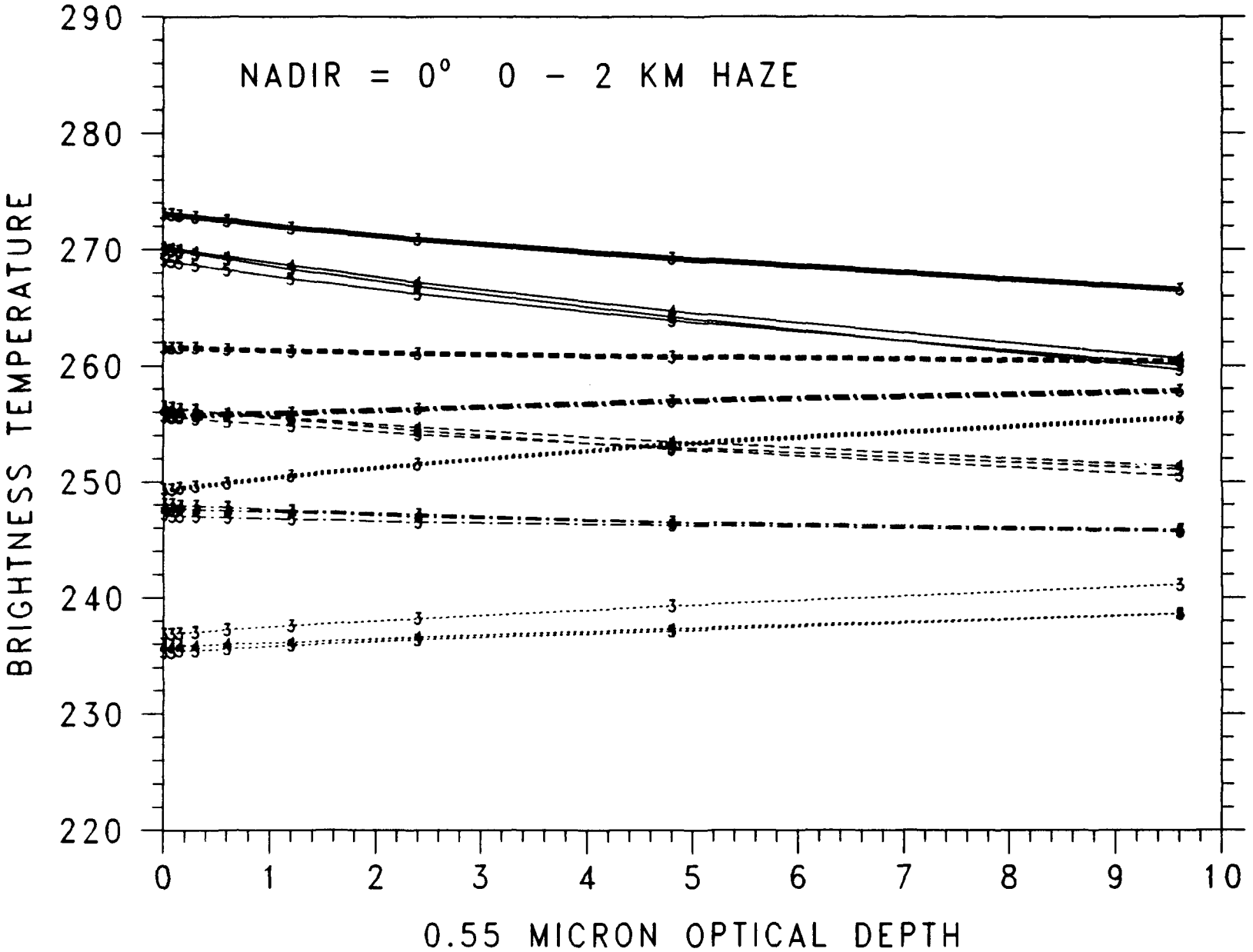
NADIR = 0° 0 - 2 KM HAZE
BRIGHTNESS TEMPERATURE
290
280
270
260
250
240
230
220
0
1
2
3
4
5
6
7
8
9
10
0.55 MICRON OPTICAL DEPTH

Figure 23g.

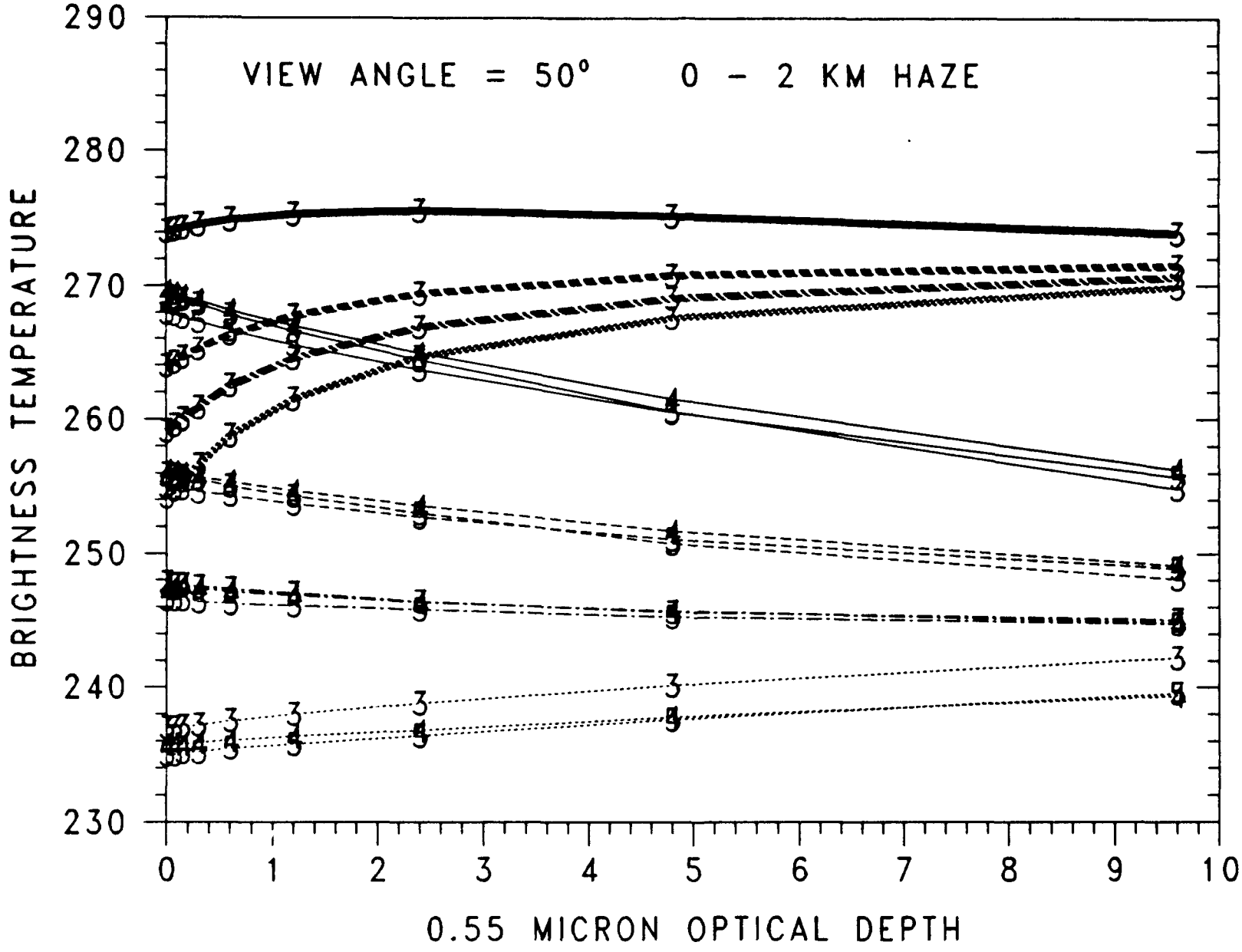
VIEW ANGLE = 50° 0 - 2 KM HAZE
BRIGHTNESS TEMPERATURE
290
280
270
260
250
240
230
0
1
2
3
4
5
6
7
8
9
10
0.55 MICRON OPTICAL DEPTH

Figure 23h.

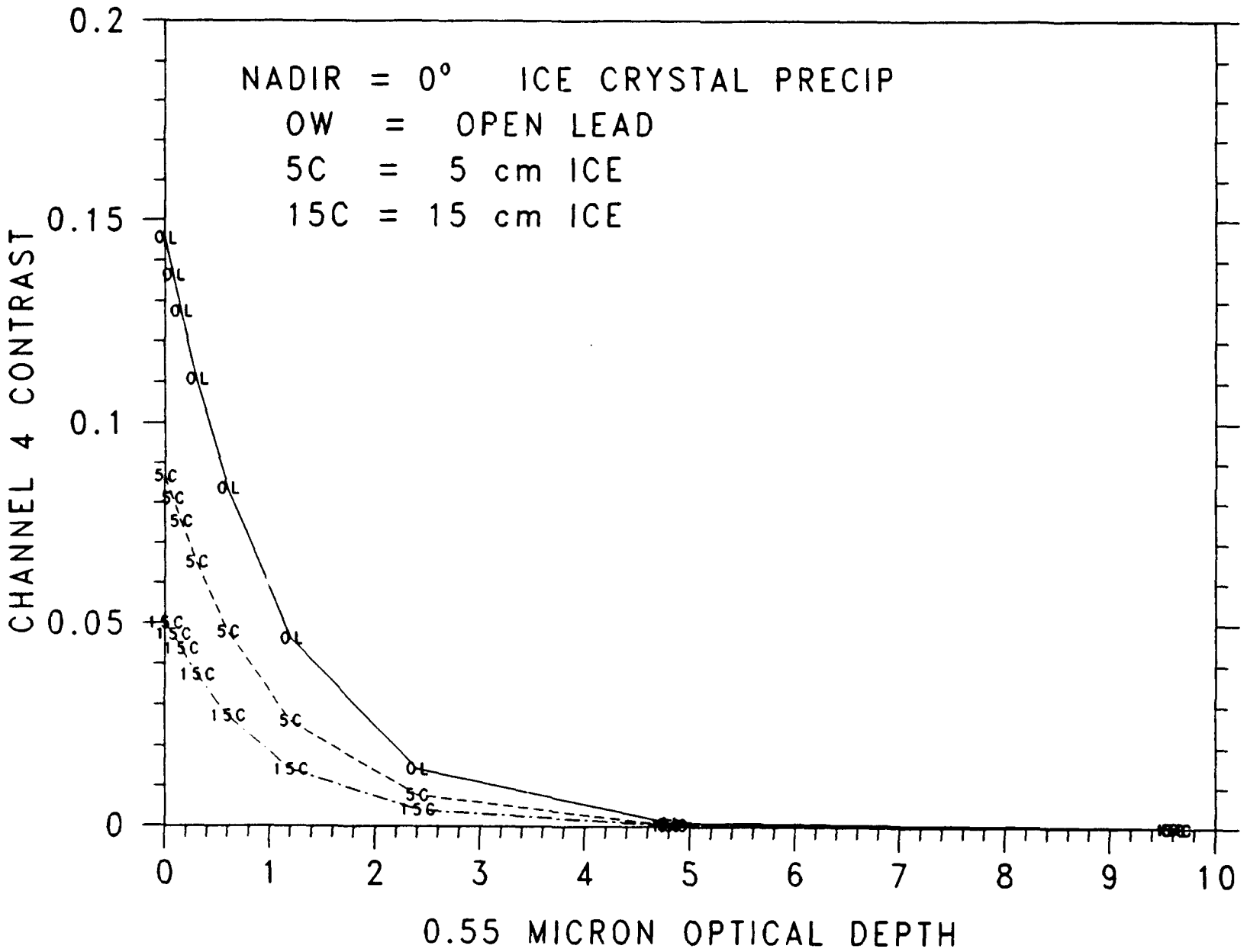

Figure 24. Normalized contrast between an open water lead and ice of two thicknesses for ice crystal precipitation, boundary layer haze, and high-level cirrus cloud at satellite view angles of 0° (a,c,e) and 50° (b,d,f). Conditions are mean January in the central Arctic.

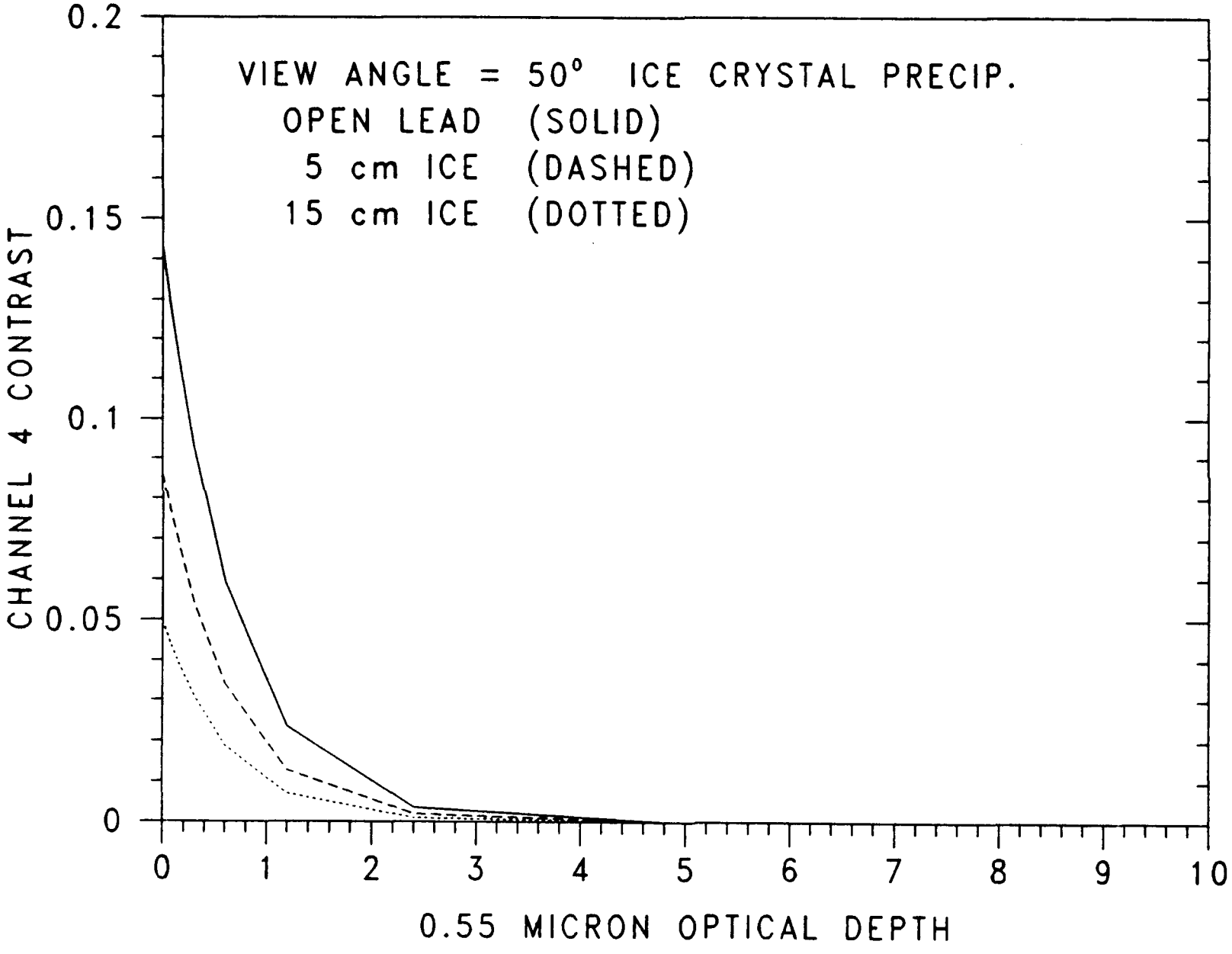
VIEW ANGLE = 50° ICE CRYSTAL PRECIP.
OPEN LEAD (SOLID)
5 cm ICE (DASHED)
15 cm ICE (DOTTED)
CHANNEL 4 CONTRAST
0.2
0.15
0.1
0.05
0
0 1 2 3 4 5 6 7 8 9 10
0.55 MICRON OPTICAL DEPTH

Figure 24b.

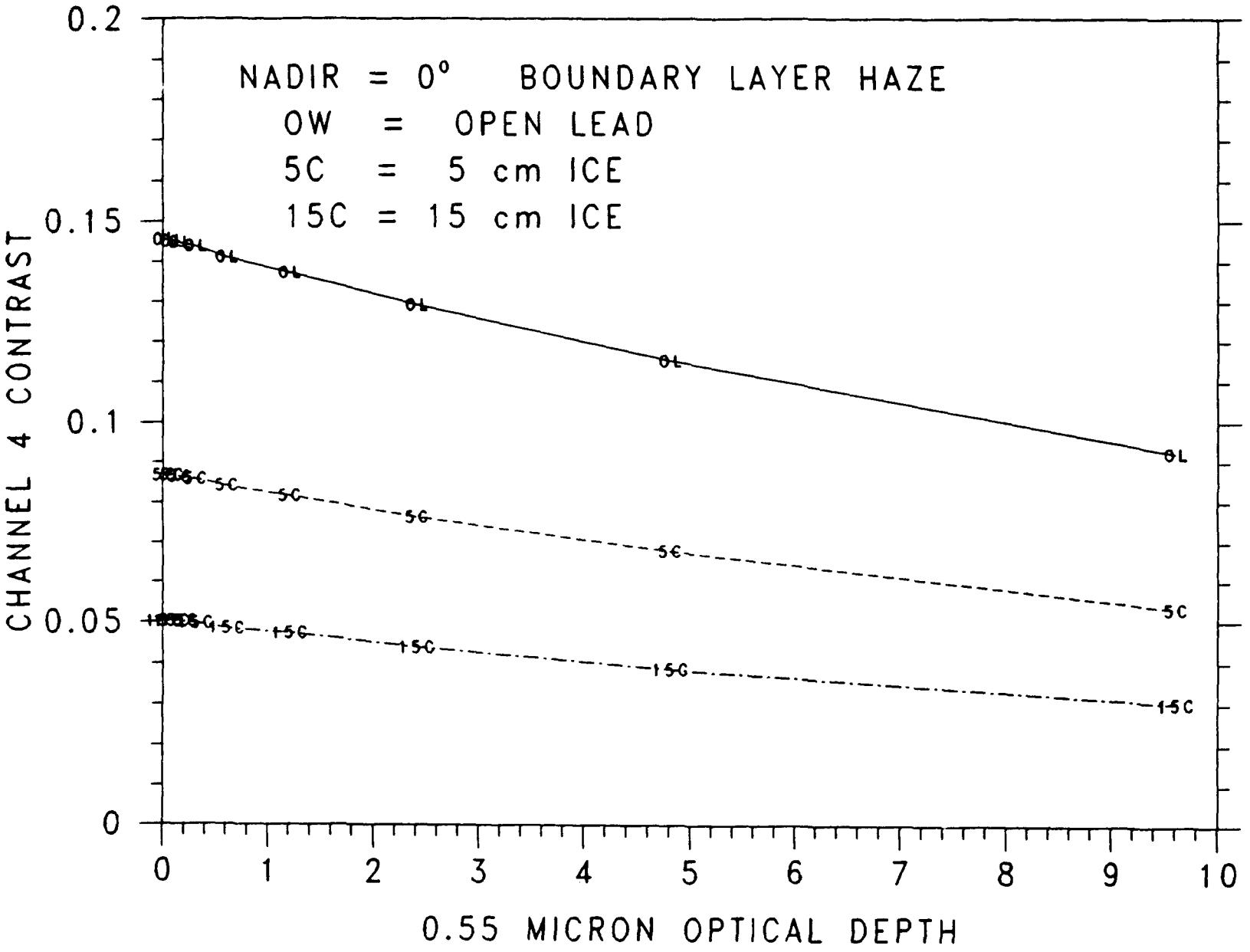
NADIR = 0° BOUNDARY LAYER HAZE
OW = OPEN LEAD
5C = 5 cm ICE
15C = 15 cm ICE
CHANNEL 4 CONTRAST
0.2
0.15
0.1
0.05
0
0 1 2 3 4 5 6 7 8 9 10
0.55 MICRON OPTICAL DEPTH
OL
5C
15C

Figure 24c.

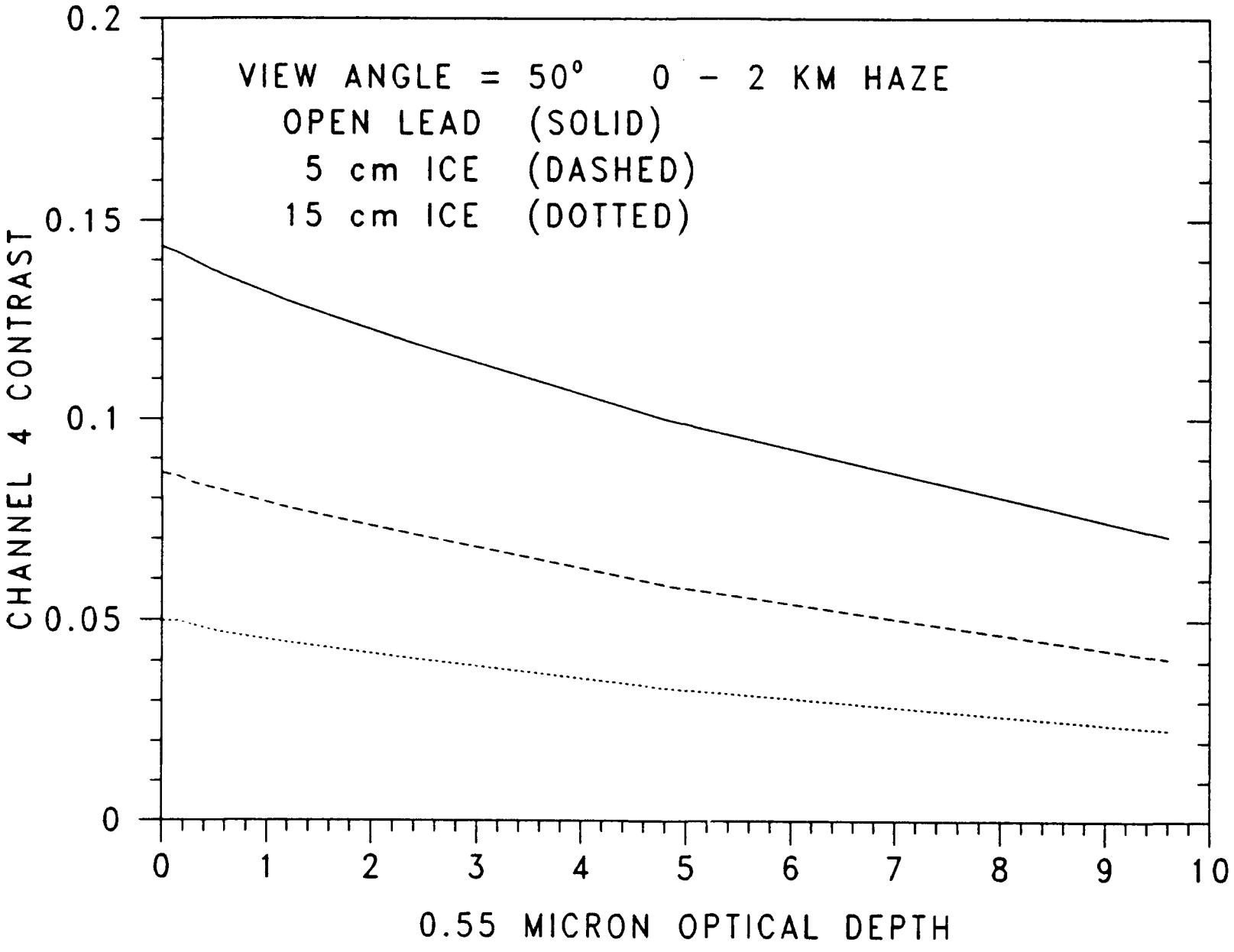
VIEW ANGLE = 50° 0 - 2 KM HAZE
OPEN LEAD (SOLID)
5 cm ICE (DASHED)
15 cm ICE (DOTTED)
CHANNEL 4 CONTRAST
0.2
0.15
0.1
0.05
0
0 1 2 3 4 5 6 7 8 9 10
0.55 MICRON OPTICAL DEPTH

Figure 24d.

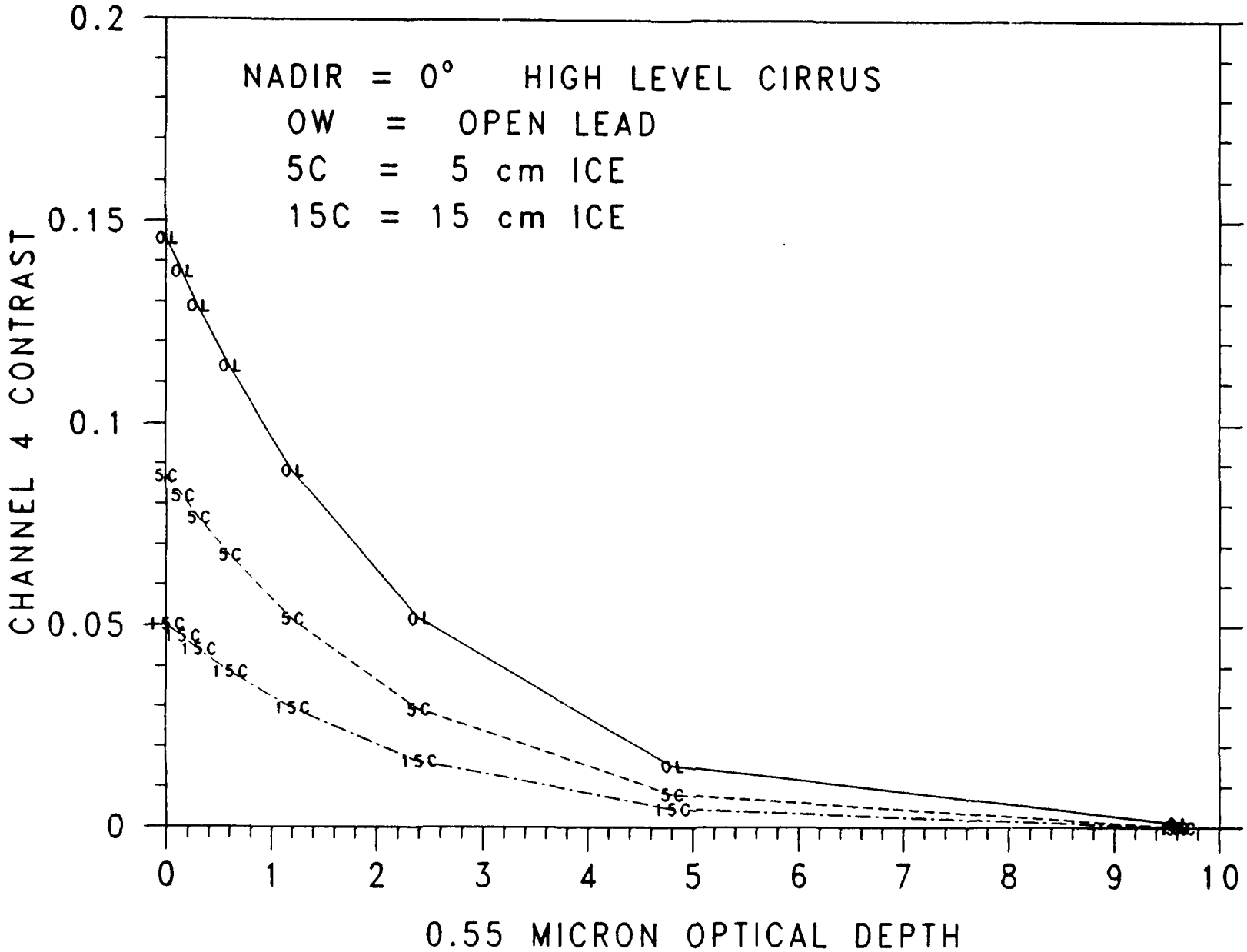
NADIR = 0° HIGH LEVEL CIRRUS
OW = OPEN LEAD
5C = 5 cm ICE
15C = 15 cm ICE
CHANNEL 4 CONTRAST
0.2
0.15
0.1
0.05
0
0 1 2 3 4 5 6 7 8 9 10
0.55 MICRON OPTICAL DEPTH

Figure 24e.

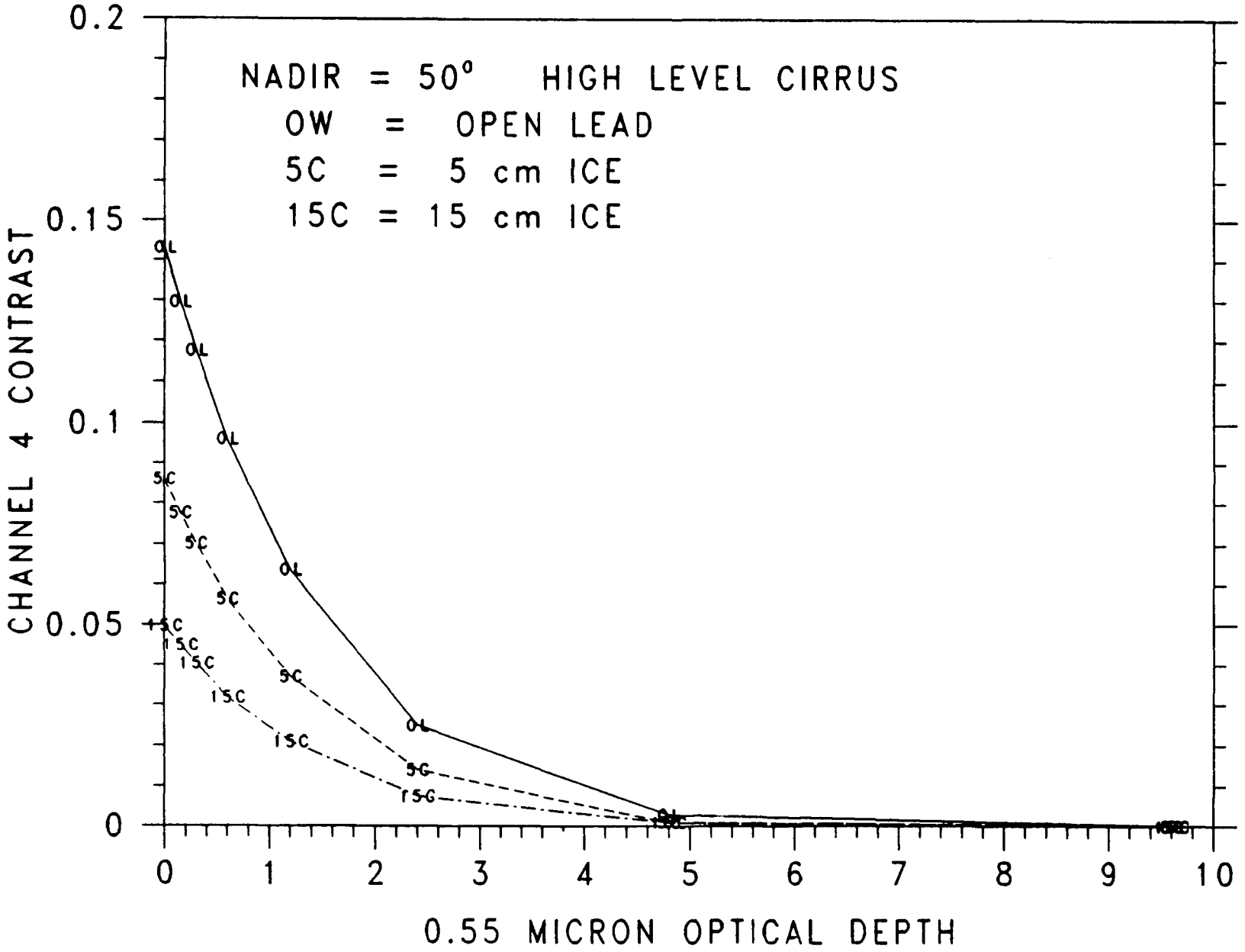
NADIR = 50° HIGH LEVEL CIRRUS
OW = OPEN LEAD
5C = 5 cm ICE
15C = 15 cm ICE
CHANNEL 4 CONTRAST
0.55 MICRON OPTICAL DEPTH
0.2
0.15
0.1
0.05
0
0
1
2
3
4
5
6
7
8
9
10
OL
5C
15C

Figure 24f.

II.2 *ICE SURFACE TEMPERATURE RETRIEVAL*

The ability to retrieve surface parameters from satellite data in the polar regions is constrained by our limited knowledge of atmospheric temperature, humidity, and aerosol profiles, the microphysical properties of polar clouds, and the spectral characteristics of the wide variety of surface types found there. In this section we present results in the retrieval of ice surface temperature (IST) from the thermal channels of the Advanced Very High Resolution Radiometer (AVHRR) sensors on-board the NOAA series satellites.

Sea and land surface temperature (SST and LST) retrieval algorithms have been developed using the thermal infrared window portion of the spectrum, with the degree of success dependent primarily upon the variability of the surface and atmospheric characteristics. The general approach to estimating surface temperature is to relate satellite observations to surface temperature observations with a regression model. Lacking sufficient observations, however, satellite radiances or brightness temperatures can be modeled by application of the radiative transfer equation. This approach is commonly used for SST retrieval.

To our knowledge, little effort has been directed to the retrieval of the sea ice surface temperature (IST) in the arctic, an area where the first effects of a changing climate are expected to be seen. The reason is not one of methodology, but rather our limited knowledge of atmospheric temperature, humidity, and aerosol profiles, the microphysical properties of polar clouds, and the spectral characteristics of the wide variety of surface types found there. We have developed a means to correct for the atmospheric attenuation of satellite-measured clear sky brightness temperatures used in the retrieval of ice surface temperature from the split-window thermal channels of the AVHRR sensors on-board three of the NOAA series satellites. These corrections are specified for three different "seasons" and as a function of satellite viewing angle, and are expected to be applicable to the perennial ice pack in the central Arctic Basin (Figure 21). We do not develop a completely new methodology; instead we modify a standard procedure for use with arctic-specific data. It is assumed that a valid cloud-clearing algorithm exists and that only clear sky radiances are being examined. The cloud clearing problem in polar satellite data is not trivial, however. For a review of polar cloud detection algorithms, see *Key and Barry* [1989] and *Sakellariou et al.* [1991].

For the retrieval of IST a multi-channel algorithm that uses empirical relationships to correct for water vapor absorption is employed:

$$T_{ice} = a + bT_4 + cT_5 + d[(T_4 - T_5)\sec\theta]$$

where T_4 and T_5 are the satellite-measured brightness temperatures (K) in the AVHRR thermal channels and θ is the sensor scan angle. The coefficients are determined through a least squares regression procedure, where surface temperatures are regressed against modeled brightness temperatures.

AVHRR thermal channel radiances are simulated with LOWTRAN as described

previously. Directional surface emissivities for snow are modeled [*Dozier and Warren*, 1982]: the single scattering albedo and asymmetry factor in the scattering phase function are calculated from the Mie equations and the directional, wavelength-dependent emissivities are derived from the delta-Eddington approximation to the equation of radiative transfer. The directional emissivities are then integrated with the response function for channel *i*:

$$\varepsilon_i(\theta) = \frac{\int_{\lambda_1}^{\lambda_2} \varepsilon(\lambda,\theta)\,\phi_i(\lambda)\; d\lambda}{\int_{\lambda_1}^{\lambda_2} \phi_i(\lambda)\; d\lambda}$$

where $\varepsilon(\lambda,\theta)$ is the emissivity in direction θ at wavelength λ and ϕ is the sensor response function which is 0 outside of $[\lambda_1,\lambda_2]$.

The use of the rawinsonde profiles in modeling the surface temperature requires an additional step since the first measurement in each profile is the shelter temperature, not the surface temperature. Therefore, the (unknown) surface temperature for each profile is assigned a series of values representing the range of possible surface temperatures for the observed conditions during the month to which the profile belongs. An energy balance model [*Maykut*, 1982] is used to determine these surface temperatures, based on the observed range of shelter temperatures and wind speeds (the mean ±1 standard deviation) in the ice island data for each month.

The seasonal dependence of the coefficients is illustrated in Table 7, where coefficients from each season were applied to data from every other season. Results are shown for NOAA 9 and indicate errors between 0.1 K for transition coefficients with winter data and 0.6 K when summer coefficients are used with winter data. Similarly, the satellite dependence of the coefficients is shown in Table 8 for summer conditions. On the average, errors ranging from 0.1 to 1.0 K, depending on season, can be expected when applying coefficients derived for one satellite to data from another, the smallest errors occurring between NOAA 7 and 9 coefficients and data. Using SST coefficients developed for the North Atlantic and the Greenland Sea area to estimate IST would result in an underestimate of up to 0.7 K, largest in winter and at scan angles of 40° and greater. While the sensor scan angle is included explicitly in the correction equation, its effect in the dry arctic atmosphere is small, generally less than 0.1 K.

Surface temperature measurements taken by a PRT-5 thermal radiometer during CEAREX in March 1989 were compared to estimated ISTs from NOAA 11 AVHRR data. The mean IST for a sample of four AVHRR pixels was 258.9 K while the mean PRT-5 temperature (adjusted for an emissivity of 0.998) of four consecutive measurements one kilometer apart was 259.04 K. Given the difficulties in comparing the two data sets these results are encouraging.

In summary, using the split window channels and scan angle, the rms error in the estimated ice surface temperature is less than 0.1 K in all seasons. Inclusion of channel 3 (3.7 μm) during the winter decreases the rms error by less than 0.003 K. Overall, employing the IST

coefficients results in increased accuracy of up to 0.6 K over SST coefficients developed for the North Atlantic and the Greenland Sea areas.

Additional details are provided in the Attachment.

TABLE 7. RMS error in applying coefficients (NOAA 9) developed for one season (left) to data from another (top).

	Data from:		
Coefficients:	Winter	Summer	Transition
Winter	0	0.403	0.128
Summer	0.587	0	0.342
Transition	0.117	0.219	0

TABLE 8. RMS error applying coefficients (summer) developed for one satellite (left) to data from another (top).

	Data from:		
Coefficients:	NOAA 7	NOAA 9	NOAA 11
NOAA 7	0	0.272	0.655
NOAA 9	0.296	0	1.017
NOAA 11	0.682	0.961	0

PART III: ACCOMPLISHMENTS AND PLANS

III.1 SUMMARY OF ACCOMPLISHMENTS TO DATE

During the first two years of the project, empirical studies concerning scale relationships in the retrieval of sea ice lead statistics have been undertaken, as have modeling investigations of atmospheric influences on the satellite signal. Additionally, we have begun the development of statistical models that describe the scaling properties of leads. The empirical studies have been based on Landsat imagery, while the atmospheric models have been specific to the AVHRR. Submarine sonar data have been used in the statistical model development. Specific accomplishments to date include:

(1) The parameterizations of clouds, haze, and atmospheric chemical constituents in the LOWTRAN 7 radiative transfer model have been reviewed. Atmospheric temperature and humidity profiles for the arctic have been constructed from Soviet ice island data and are being used in the model.

(2) Resampling methods have been tested on simulated, AVHRR, and Landsat images, as have the effects of digital enhancements.

(3) Procedures for the retrieval of lead statistics have been developed and applied to Landsat imagery successively degraded to more coarse resolutions.

(4) The relationship between "apparent" lead widths measured along a transect (e.g., from submarine sonar or as a sampling method for satellite imagery) and the "true" lead width distribution has been formalized in a statistical sense, so that one distribution may be obtained from the other. Submarine sonar data from the Canada Basin during summer and fall has been analyzed in this context.

(5) A statistical model has been developed for the retrieval of lead area fraction from measurements along a line; e.g., a submarine sonar transect or a lineal sampling method for satellite images.

(6) The effect of atmosphere/surface conditions on the AVHRR-measured radiance in the thermal channels has been examined. Surfaces include open water, 5 cm, 15 cm, and 2 m thick ice. Atmospheric conditions included clear sky with haze, cirrus, and low-level ice crystal plumes.

(7) Additional KRMS data has been acquired from D. Eppler (NOARL) for a time period in which DMSP OLS data is currently being used in the analysis of lead patterns.

Two graduate students (E. Ellefsen and S. Peckham) were supported in part by this project. As a consequence of their involvement, one paper has been published and another will soon be submitted for publication.

Additionally, J. Key and R. Stone have just completed sun photometer measurements on

the NOAA P-3 during LEADEX. These data will be used to determine typical (during LEADEX) aerosol properties, in particular optical depths. This information is critical in the radiative transfer modeling discussed earlier.

Lastly, two workshops for the satellite remote sensing investigators of the Leads ARI have been hosted by this group in Boulder. Report on the highlights of those meeting were sent to C. Luther and T. Curtin late in 1990. Recommendations for aircraft instrumentation during LEADEX'92 were made.

III.2 PAPERS SUPPORTED IN WHOLE OR IN PART BY N00014-90-J-1840 (See Attachments)

Key, J. and S. Peckham, 1991. Probable errors in width distributions of sea ice leads measured along a transect. *J. Geophys. Res.*, 96(C10), 18417-18423.

Key, J. and M. Haefliger, 1991. Retrieval of ice surface temperature, outgoing longwave radiation, and cloud cover from AVHRR data. WMO Report on **Polar Radiation Fluxes and Sea Ice Modeling**, WCRP-62, WMO/TD-No. 442, C22-C28.

Key, J. and M. Haefliger. Arctic ice surface temperature retrieval from AVHRR thermal channels. *J. Geophys. Res.*, in press (expected April 1992).

Key, J., R. Stone, J. Maslanik, and E. Ellefsen, 1992, The Detectability of Sea Ice Leads in Satellite Data as a Function of Atmospheric Conditions and Measurement Scale, *Annals Glaciol.*, submitted (March 1992).

Papers *in Preparation* Acknowledging N00014-90-J1840 (tentative titles; short versions are given in the previous sections):

- The Effect of Sensor Resolution on the Observed Fractional Area Coverage of Geophysical Variables
- Estimation of the Area Fraction of Sea Ice Leads from Measurements Along a Transect
- The Detectability of Winter Sea Ice Leads in Thermal Satellite Data Under Varying Atmospheric Conditions

III.3 PLANNED ACTIVITIES FOR YEAR 3

During LEADEX a comprehensive suite of measurements will be taken, many of which can be used for the validation of geophysical retrieval algorithms developed for use with satellite data. The measurements will be taken by a variety of investigators and include atmospheric and surface physical and radiative properties, collected using ground-based and airborne sensors. Additionally, a variety of satellite data will be collected throughout the experiment. During year 3 we will obtain from the various investigators all data pertinent to the retrieval of lead information from satellite data, primarily the AVHRR, and use these data in the validation of the retrieval algorithms developed in the first two years of this project based on radiative transfer modeling to simulate AVHRR radiances as well as empirical models of the dependence of lead statistics (geometrical) on measurement scale.

In May 1992, J. Key, J. Maslanik, and two others at CIRES will participate in the Canadian SIMMS field program in the Baffin Strait/Lancaster Sound area. The purpose of the program is to collect data that can be used for the validation of satellite retrieval algorithms, in particular those related to ERS-1 SAR. Our objectives are to collect data that can be used with visible and thermal satellite data, in particular the AVHRR. The data will be an important complement to the measurements taken during LEADEX.

The objective of year 3 is to validate algorithms and empirical models developed previously for the retrieval of lead-related parameters from satellite data. This validation requires a comprehensive set of surface, aircraft, and satellite data that includes a complete (or as complete as possible) characterization of the surface radiative and geometrical properties and the atmospheric physical and radiative properties. Specifically, our objectives are to:

(1) Compile a complete satellite validation data set of surface, aircraft, and satellite observations.

(2) Use this data set to validate algorithms previously developed (in the first two years of this project) for the retrieval of

   a. ice surface temperature (IST),
   b. thermal contrast between leads and the surrounding ice,
   c. lead width distributions as a function of measurement scale, and
   d. the "true" lead width distribution from low-resolution measurements alone.

Additionally, we will examine spectral reflectance measurements of the surface and relate them to the AVHRR shortwave channels for selected case studies.

REFERENCES

Blanchet, J. and R. List, Estimation of optical properties of arctic haze using a numerical model, *Atmos.-Ocean*, 21, 444-465.

Curry, J.A., F.G. Meyer, L.F. Radke, C.A. Brock, and E. Ebert, 1990: Occurrence and characteristics of lower tropospheric ice crystal in the Arctic. *Int. J. Climatology*, 10, 749-764.

De Cola, L., Fractal analysis of a classified Landsat scene, *Photogram. Eng. Remote Sens.*, 55 (5) 601-610, 1989.

Dozier, J. and S.G. Warren, Effect of viewing angle on the infrared brightness temperature of snow, *Water Resources Res.*, 18(5), 1424-1434, 1982.

Eppler, D.T. and W.E. Full, 1992, Polynomial trend surface analysis applied to AVHRR images to improve definition of Arctic leads. *Remote Sensing of Environ.*, in press.

Jones, J.G., R.W. Thomas, and P.G. Earwicker, Multiresolution analysis of remotely sensed imagery, *Int. J. Remote Sensing*, 12 (1), 107-124, 1991.

Justice, C.O., B.L. Markham, J.R.G. Townshend, and R.L. Kennard, 1989. Spatial degradation of satellite data. *Int. J. Remote Sens.*, 10 (9), 1539-1561.

Key, J., A.J. Schweiger, and J.A. Maslanik, 1990. Mapping sea ice leads with a coupled numeric/symbolic system. **ACSM/ASPRS Proceedings, Vol. 4**, Denver, Colorado, March 18, 228-237.

Key, J. and R.G. Barry, Cloud cover analysis with arctic AVHRR data: 1. cloud detection, *J. Geophys. Res.*, 94(D15), 18521-18535, 1989.

Key, J. and M. Haefliger. Arctic ice surface temperature retrieval from AVHRR thermal channels. *J. Geophys. Res. (Atmospheres)*, ???.

Kneizys, F.X., E.P. Shettle, L.W. Abreu, J.H. Chetwynd, G.P. Anderson, W.O. Gallery, J.E.A. Selby, and S.A. Clough, 1988, Users Guide to LOWTRAN 7, AFGL- TR-88-0177, *Environmental Research Papers*, No. 1010, 137 pp.

Lovejoy, S., Area-perimeter relation for rain and cloud areas, *Science*, 216, 185-187, 1982.

Maykut, G.A., Large-scale heat exchange and ice production in the central Arctic, *J. Geophys. Res.*, 87(C10), 7971-7984, 1982.

Miles, R.E., Random polygons determined by random lines in a plane, *Proc. National Academy Sci.*, 52, 901-907, 1964.

Robert, A. and A.G. Roy, On the fractal interpretation of the mainstream length-drainage area relationship, *Water Resources Res.*, 26 (5), 839-842, 1990.

Rothrock, D.A. and A.S. Thorndike, Measuring the sea ice floe size distribution, *J. Geophys. Res.*, 89 (C4), 6477-6486, 1984.

Sakellariou, N.K., H.G. Leighton, and Z. Li, Identification of clear and cloudy pixels at high latitudes from AVHRR radiances, *Int. J. Remote Sensing*, in press.

Shenk, W.E. and V.V. Salomonson, A simulation study exploring the effects of sensor spatial resolution on estimates of cloud cover from satellites, *J. Appl. Meteor.*, 11, 214-220, 1972.

Stamnes, K., S-C Tsay, W. Wiscombe, and K. Jayaweera, 1988, Numerically stable algorithm for discrete-ordinate-method radiative transfer in multiple scattering and emitting layered media, *Applied Optics*, 27, 2502-2509.

Stoyan, D., W.S. Kendall, and J. Mecke, Stochastic Geometry and its Applications. New York: Wiley, 345 pp., 1989.

Townshend, J.R.G. and C.O. Justice, Selecting the spatial resolution of satellite sensors required for global monitoring of land transformations, *Int. J. Remote Sensing*, 9 (2), 187-236, 1988.

Tsay, S.C., K. Stamnes, and K. Jayaweera, 1989. Radiative energy budget in the cloudy and hazy arctic. *J. Atmos. Sci.*, 46 (7), 1002-1018.

Wielicki, B.A. and R.M. Welch, Cumulus cloud properties derived using Landsat satellite data, *J. Clim. Appl. Meteorol.*, 25, 261-276, 1986.

Woodcock, C.E. and A.H. Strahler, The factor of scale in remote sensing, *Remote Sensing Environ.*, 21, 311-316, 1987.

ATTACHMENTS

1. Retrieval of Ice Surface Temperature, Outgoing Longwave Radiation, and Cloud Cover from AVHRR Data (WMO Report)

2. Probable Error in Lead Width Distributions Measured Along a Transect (JGR)

3. Ice Surface Temperature Retrieval from AVHRR Thermal Channels (JGR)

4. The Detectability of Sea Ice Leads in Satellite Data as a Function of Atmospheric Conditions and Measurement Scale (Annals of Glaciology)

RETRIEVAL OF ICE SURFACE TEMPERATURE, OUTGOING LONGWAVE RADIATION, AND CLOUD COVER FROM AVHRR DATA

J. Key and M. Haefliger

Cooperative Institute for Research in Environmental Sciences
University of Colorado
Boulder, Colorado 80309-0449

INTRODUCTION

Satellite data for the estimation of radiative and turbulent heat fluxes is becoming an increasingly important tool in large-scale studies of climate. The ability to measure parameters needed for flux estimation in the polar regions is constrained by our limited knowledge of atmospheric temperature, humidity, and aerosol profiles, the microphysical properties of polar clouds, and the spectral characteristics of the wide variety of surface types found there. In this paper we present preliminary results of experiments in the retrieval of ice surface temperature (IST) and outgoing longwave radiation (OLR) from the thermal channels of the Advanced Very High Resolution Radiometer (AVHRR) sensors on-board the NOAA series satellites. The status of polar cloud retrieval from AVHRR data is also discussed. Inadequacies in our ability to measure essential parameters are identified and future directions are suggested.

DATA AND METHODS

Analyses are based on atmospheric temperature and humidity profiles collected by radiosonde from the Soviet ice islands RVAB (approximately 80°N 160°W) during 1979-83 and EMIO (approximately 87°N 175°E) during 1983-1987. Generally two observations per day were collected covering a vertical range of 0 to 25 km. Profiles that had more than 10 levels were retained in the analyses. Observations include temperature, dew point depression, wind speed, and wind direction. For the years 1986-87 cloud observations are also available for EMIO. These observations include low, middle, and high cloud types, height of the cloud base, and cloud fraction.

Mean summer and winter temperature profiles for clear, cloudy, and mixed conditions are shown in Figures 1, 2, and 3, respectively. Cloud radiative forcing is evident in the summer and winter clear and cloudy profiles where tropospheric temperatures are higher under cloud cover in the winter and lower under summer cloud cover. In addition, the summer surface inversion disappears under cloud cover. The standard subarctic winter temperature profile is shown in Figure 4. Standard deviation at all levels was computed for each parameter. The maximum winter standard deviations in temperature and dew point depression were 6.8 K and 3.3 K, respectively between 0 and 10 km. In summer the corresponding values are 6.0 K and 5.8 K. Interpretation of dew point depression variability requires care since the mean water vapor content is very low, generally less than 0.6 gm m^{-3}.

For IST and OLR retrieval, the individual profiles are used with the LOWTRAN-7 radiative transfer model to estimate radiances in the three AVHRR thermal bands (channels 3, 4, and 5 at 3.7μm, 11μm, and 12μm, respectively). To avoid contamination of solar radiation in channel 3, summer analyses are limited to nighttime. To examine the effect of vertical temperature structure on upwelling longwave radiation, radiances in the three channels

were estimated using the arctic mean and subarctic standard winter and summer profiles with identical seasonal surface temperatures. The maximum difference in radiances was 0.05 W m^{-2} sr^{-1} indicating that the vertical temperature distribution of the relatively dry arctic atmosphere plays a very small role in the attenuation of upwelling longwave radiation.

ICE SURFACE TEMPERATURE RETRIEVAL

For the retrieval of IST we employ a multi-channel SST algorithm that uses empirical relationships to correct for water vapor absorption (Barton et al., 1989):

$$T_{ice} = a_0(\theta) + \sum_{k=1}^{n} a_k(\theta)T_k + a_w(\theta)W \qquad (1)$$

where $a_i(\theta)$ are satellite zenith angle-dependent coefficients, T_k are the satellite-measured brightness temperatures in the thermal channels, and W is the vertical water vapor column. Atmospheric profiles under clear sky conditions for 1986-87 are used in the analysis.

Coefficients are determined separately for summer and winter, and for various combinations of the three thermal channels. Additionally, the scan angle dependence was investigated for the winter months. Results are given in Table 1 for selected channel and viewing angle combinations.

Table 1. Regression coefficients for the estimation of IST based on AVHRR thermal channels.

	Coefficients				
	R^2	Intercept	a_{ch3}	a_{ch4}	a_{ch5}
Summer, T_4, T_5; θ=0°	0.99	-2.06	---	3.01	-1.99
Summer, T_3, T_4, T_5; θ=0°	1.00	-4.08	0.39	2.65	-2.02
Winter, T_4, T_5; θ=0°	1.00	-3.08	---	3.06	-2.05
Winter, T_3, T_4, T_5; θ=0°	1.00	-2.21	-0.14	2.69	-1.54
Winter, T_3, T_4, T_5; θ=20°	1.00	-2.01	-0.16	2.63	-1.45
Winter, T_3, T_4, T_5; θ=40°	1.00	-2.11	-0.15	2.71	-1.54

The large coefficients of variation (R^2) in Table 1 indicate that the attenuation of upwelling radiation in the polar atmosphere is minimal, especially in summer. Either of channels 4 or 5 alone could be used in the estimation of IST. Not correcting for atmospheric effects would result in an IST underestimate of 1.5-2.1 K in channel 4 and 1.9-3.2 K in channel 5, summer or winter. The relationship between surface temperature and channel 4 brightness temperature is shown in Figure 5.

REMAINING PROBLEMS

The primary problem in using the ice island atmospheric data set concerns the difference between "surface" temperature as reported, and the skin temperature. The actual

height of the first measurement is unknown, but may be a few meters above the surface. The difference between this value and the skin temperature can be positive or negative. We would expect the difference to be smallest over multiyear ice in winter and largest in the summer when the surface is melting. Until more complete data are available this will remain a problem. In the discussions that follow, the "surface" temperature refers to the temperature at the level of the first measurement. A second problem concerns the unknown emissivity of the surface, as well as its bidirectional emittance characteristics.

Future work will include an investigation of methods for estimating the skin temperature based on the radiosonde data. Such a method may be simply an extrapolation of the lapse rate back to the surface, or may take an energy balance approach. A new data set acquired over Greenland is currently being analyzed, and should prove useful in this regard. The CEAREX '89 and MIZEX '84 data sets will also be useful for validation. Multi-angle methods of IST retrieval, which are based on the differential absorption due to different atmospheric path lengths when the same object is seen from two different view angles, will be investigated when data from the Along Track Scanning Radiometer (ATSR) on-board the ERS-1 become available.

STATUS OF CLOUD PARAMETER RETRIEVAL

Polar cloud detection algorithms based on satellite data have used spectral, spatial, and temporal information, yet no single method has become generally accepted. One visible and one thermal channel do not generally provide an unambiguous solution to the problem, especially for low clouds over snow or ice surfaces. Therefore, snow and ice cover data have been used as have passive microwave products. Some of the basic ideas of the cloud detection portion of the International Satellite Cloud Climatology Project (ISCCP) algorithm (Rossow *et al.*, 1988) have been adapted for use with polar AVHRR and SMMR (Scanning Multichannel Microwave Radiometer) data as shown in Figure 6 (Key and Barry, 1989). In test cases with synthetic and actual data, this algorithm has demonstrated the importance of additional spectral information (AVHRR channel 3 and the differences between 3 and 4) in polar cloud identification. Winter data requires a separate algorithm, in part due to the lack of visible data and in part due to the differences in the vertical temperature structure.

While this algorithm can provide rough estimates of cloud fraction, a more accurate determination of this parameter as well as the retrieval of cloud top height and cloud optical thickness requires knowledge of the temperature profile. Such information could be derived from TOVS, although further validation over polar regions is necessary. Instead, given sufficiently small variability in the vertical temperature structure for a homogeneous region, mean monthly temperature and humidity profiles may provide enough information for cloud detection.

REMAINING PROBLEMS

Unfortunately, the multispectral thresholds used in the cloud detection algorithm were chosen through experimentation, and lack a sound theoretical basis. Additionally, co-locating SMMR (or SSM/I) data with the AVHRR image is computationally intensive.

Future work includes the use of TOVS data for the retrieval of temperature profiles in the polar regions, although this will require a significant validation effort (which is currently in progress at the Laboratoire de Meteorologie Dynamique, the University of Washington, and the University of Colorado). With the possible exception of arctic stratus, the microphysical

characteristics of polar clouds and haze have not been studied adequately, in spite of their importance in polar climates. The retrieval of sub-pixel cloud fraction using a multi-channel approach needs further exploration.

OUTGOING LONGWAVE RADIATION FROM NARROW BAND MEASUREMENTS

Estimates of total longwave radiation flux are obtained by application of a regression equation to the thermal window radiances (Ohring et al., 1984). This relationship takes the form

$$T_f = a_0 + \sum_{k=1}^{n} a_k T_k + b_k T_k^2 \qquad (2)$$

where T_f is the flux equivalent brightness temperature (K), and n is the number of thermal channels. It may also be useful to include the difference between brightness temperatures in channels 4 and 5, which accounts for the effects of water vapor loading. This form applies only to nadir views, which may be estimated by means of a limb-darkening function. Equation (2) shows a quadratic form of the relationship, although the linear form may be sufficient and is used here. An example of this relationship is shown in Figure 7, which relates T_f to T_4.

As with IST retrieval, coefficients are determined separately for summer and winter. Results are given in Table 2 for channels 4 and 5, and for all three thermal channels. Scan angle dependencies have not yet been investigated for cloudy conditions.

Table 2. Regression coefficients for the estimation of OLR based on AVHRR thermal channels.

	Coefficients				
	R^2	Intercept	a_{ch3}	a_{ch4}	a_{ch5}
Winter, T_4, T_5	0.87	74.33	---	1.42	-0.76
Winter, T_3, T_4, T_5	1.88	67.71	0.32	0.66	-0.29

REMAINING PROBLEMS

While the results presented above for the three thermal channels are encouraging, the estimation procedure could, in theory, be improved by sampling the longwave portion of the spectrum at additional wavelengths. Using other thermal channels from sensors such as the HIRS sounder has been investigated elsewhere (cf., Ellingson et al., 1990) and has demonstrated increased accuracy.

Future work includes an investigation of scan angle dependence and limb darkening functions, and a comparison of the modeled broadband irradiances to those measured by the Earth Radiation Budget (ERB) satellite.

Acknowledgements. J. Key was supported under University of Washington subcontract #721557 (NASA) and ONR grant N00014-90-J-1840. M. Haefliger was supported under NASA grant NAGW-2158. Thanks are due to M. Serreze and J. Kahl for providing the ice island atmospheric data.

REFERENCES

Barton, I.J., A.M. Zavody, D.M O'Brien, D.R. Cutten, R.W. Saunders, and D.T. Llewellyn-Jones, Theoretical algorithms for satellite-derived sea surface temperatures, *J. Geophys. Res.*, 94 (D3), 3365-3375, 1989.

Ellingson, R.G., H-T. Lee, and A. Gruber, Validation of a technique for estimating outgoing longwave radiation from HIRS radiance observations, **Seventh Conference on Atmospheric Radiation**, July 23-27, 1990, San Francisco, 111-112.

Key, J. and R.G. Barry, Cloud cover analysis with arctic AVHRR data: 1. cloud detection, *J. Geophys. Res.*, 94 (D15), 18521-18535.

Ohring, G. and A. Gruber, Satellite determinations of the relationship between total longwave radiation flux and infrared window radiance, *J. Climate Appl. Meteorol.*, 23, 415-425, 1984.

Rossow, W.B., L.C. Garder, P.-J. Lu, and A. Walker, The International Satellite Cloud Climatology Project documentation of cloud data, *Rep. WMO TD266*, World Meteorol. Org., December 1988.

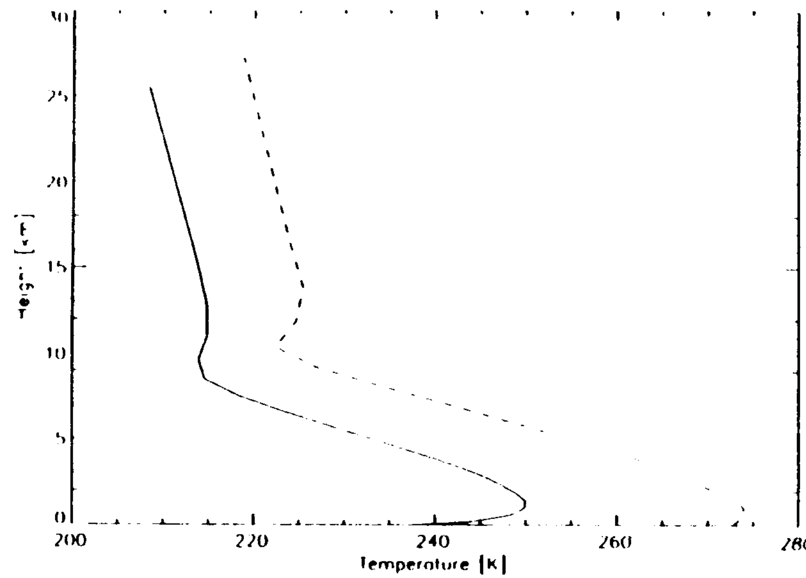

Fig. 1 Clear sky summer (June-August, 1986-87, dashed line) and winter (December-February, 1986-87; solid line) temperature profiles for the EMIO ice island. Mean profiles are based on 123 winter and 34 summer observations.

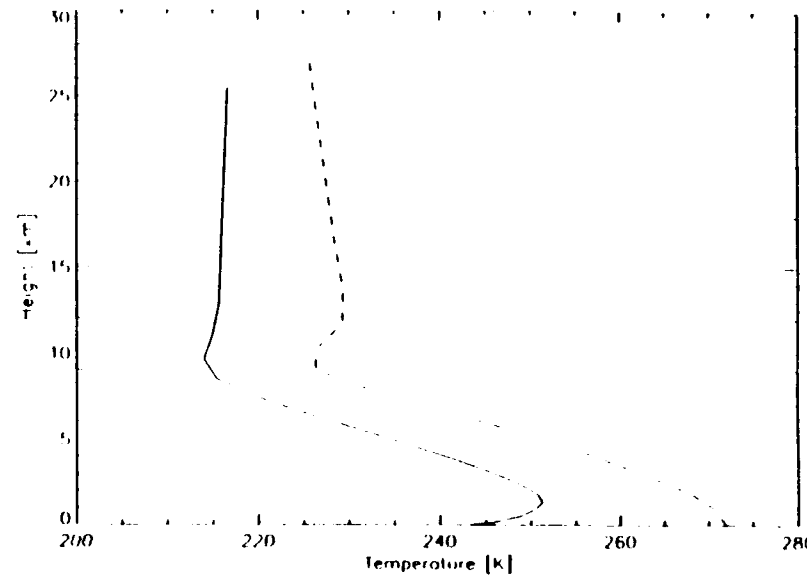

Fig. 2 Cloudy sky summer (June-August, 1986-87; dashed) and winter (December-February, 1986-87; solid) temperature profiles for the EMIO ice island. Mean profiles are based on 94 winter and 155 summer observations.

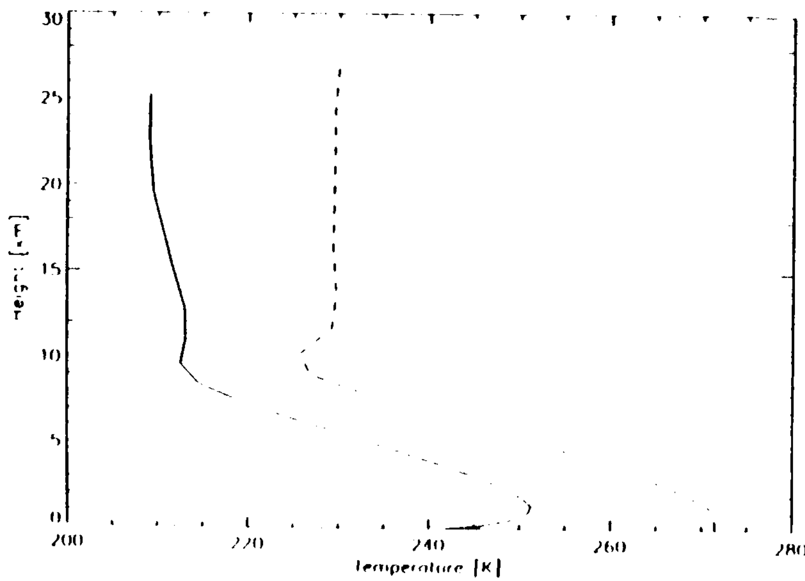

[redacted] [redacted] Fig. 3 Summer (June-August, dashed) and winter (December-February; solid) clear and cloudy [redacted] mper[redacted]ofiles[redacted] EMI[redacted]RVA[redacted]ands [redacted] profi[redacted]based[redacted] winter and 976 summer observations collected between 1979 and 1987.

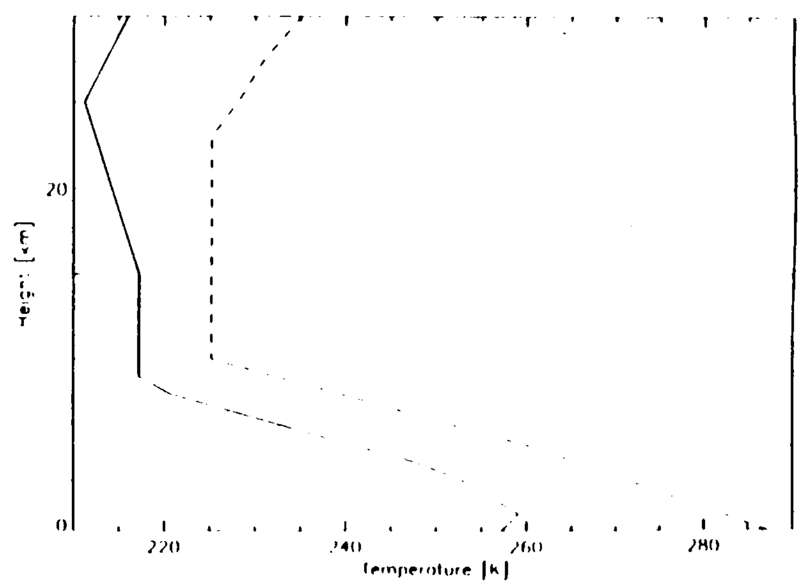

[redacted] Fig. 4. [redacted]d sub[redacted]ummer[redacted]hed) a[redacted]er te[redacted]e (so[redacted]files [redacted] [redacted]

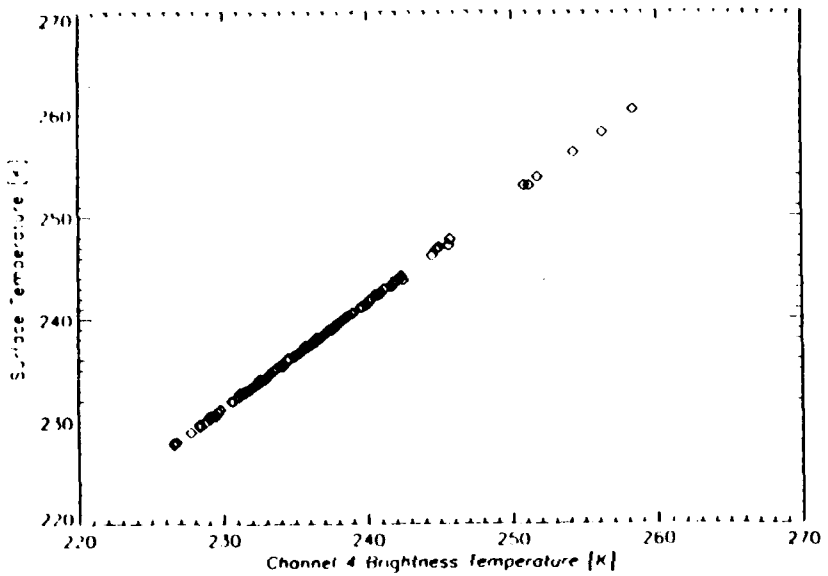

Fig 5 Surface temperature vs. channel 4 (11μm) brightness temperature for the EMIO ice island in winter

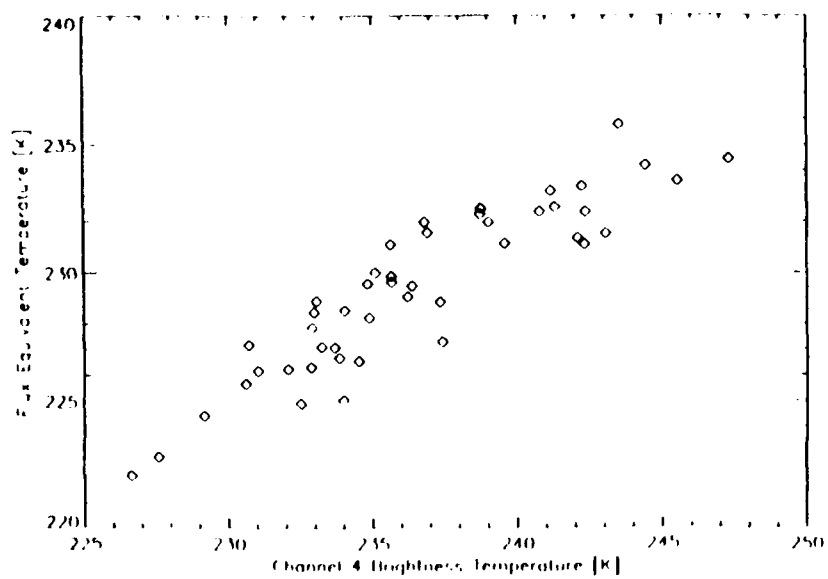

Fig 7 Flux equivalent brightness temperature (4-50 μm) as a function of AVHRR channel 4 brightness temperature for winter clear and cloudy observations

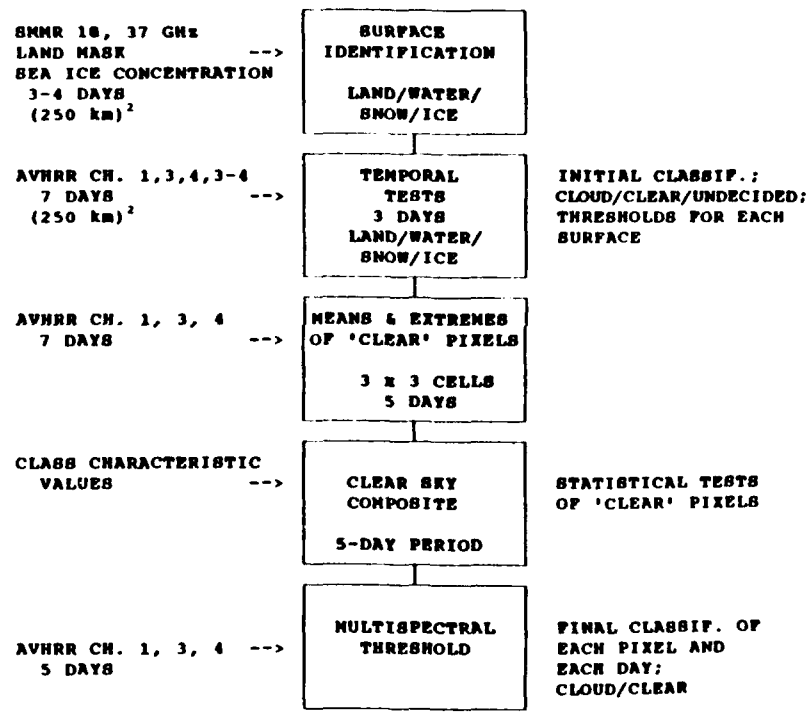

Fig. 6. Flow chart of a polar cloud detection algorithm based on AVHRR data but utilizing ancillary information for the identification of surface types. From Key and Barry (1989)

JOURNAL OF GEOPHYSICAL RESEARCH, VOL. 96, NO. C10, PAGES 18,417-18,423, OCTOBER 15, 1991

Probable Errors in Width Distributions of Sea Ice Leads Measured Along a Transect

J. KEY

Cooperative Institute for Research in Environmental Sciences, University of Colorado, Boulder

S. PECKHAM

Cooperative Institute for Research in Environmental Sciences, and Department of Geology, University of Colorado, Boulder

The degree of error expected in the measurement of widths of sea ice leads along a single transect are examined in a probabilistic sense under assumed orientation and width distributions, where both isotropic and anisotropic lead orientations are examined. Methods are developed for estimating the distribution of "actual" widths (measured perpendicular to the local lead orientation) knowing the "apparent" width distribution (measured along the transect), and vice versa. The distribution of errors, defined as the difference between the actual and apparent lead width, can be estimated from the two width distributions, and all moments of this distribution can be determined. The problem is illustrated with Landsat imagery and the procedure is applied to a submarine sonar transect. Results are determined for a range of geometries, and indicate the importance of orientation information if data sampled along a transect are to be used for the description of lead geometries. While the application here is to sea ice leads, the methodology can be applied to measurements of any linear feature.

1. INTRODUCTION

Polar sea ice is an important factor in the complex interaction of ocean and atmosphere. Reduction in the extent and thickness of sea ice due to global warming, and the consequent increase in the number of cracks in the ice (hereafter "leads"), is expected to further increase global temperatures. This positive feedback is a result of reduced albedo and the increase in heat transfer from the ocean to the atmosphere. Model estimates indicate that an increase of 4% in the area covered by leads during winter could produce a hemisphere-wide warming of 1 degree Kelvin [*Ledley*, 1988]. Understanding lead formation processes as well as the geographical and temporal distribution of lead networks is therefore important to studies of global climate.

Measurements of ice thickness and lead coverage are commonly made along transects using upward-looking submarine sonar. The footprint of the sonar beam used by submarines to observe ice conditions is of sufficiently high resolution, often 3 m or less as opposed to 25 m or more for satellite sensors, to make it a potentially useful instrument for gathering lead statistics. In fact, sonar data have shown that the largest number of lead widths are in the 10-20 m range. Lead width statistics derived from submarine sonar data have been reported in the literature [e.g., *McLaren*, 1989; *Wadhams*, 1981; *Wadhams and Horne*, 1980], but when lead orientation and width statistics are not available, the error in these analyses cannot be accessed. This error may be relatively small if leads are narrow or randomly oriented, but may be large in the case of wide leads or leads with a preferred orientation. While it may not be possible to determine the actual error for much of the archived sonar data, an important question concerns whether or not the data can be used for lead geometry statistics, and if so, what is the magnitude of the maximum error. In this paper a probabilistic determination of this error is described, providing a starting point for the application of stochastic geometry theorems in the analysis of lead geometries. Errors in statistics derived for other lead and keel features are discussed briefly. While the application is to sea ice leads and sonar data, the methods also apply to the general problem of sampling linear features along a transect.

Paper number 91JC01843.
0148-0227/91/JC-01843$05.00

2. DEFINITIONS, NOTATION, AND AN ILLUSTRATION

In the following discussions, notation follows that used in probability theory, where $F_Z(z)$ denotes the distribution function (df) for the population random variable Z with specific instance z (i.e., $F_Z(z) \equiv P[Z < z]$) and $f_Z(z)$ is the probability density function (pdf). Additionally, $E[Z]$ and $\mathrm{Var}[Z]$ are the expected value and variance of Z.

The problem is to relate a distribution of lead widths taken along a line perpendicular to the local orientation of a lead (the "actual" width) to the lead widths measured along a transect (the "apparent" lead width), taking into account lead orientations, and lead crossing angles. As illustrated in Figure 1, the following continuous random variables are defined: X is actual lead width, X' is apparent lead width measured along a transect, Θ is lead orientation ($0 \le \Theta < \pi$), and A is lead intersection angle ($0 \le A < \pi$), with specific realizations x, x', θ, and α. Additionally, let ϕ be the transect orientation ($0 \le \phi < \pi$). The position and orientation of a lead within the plane are uniquely specified by the length of the perpendicular that connects the lead to the origin, and the angle that it makes with a fixed reference line. The intersection angle A is measured between the transect and the lead, anticlockwise, and is the difference between their orientations.

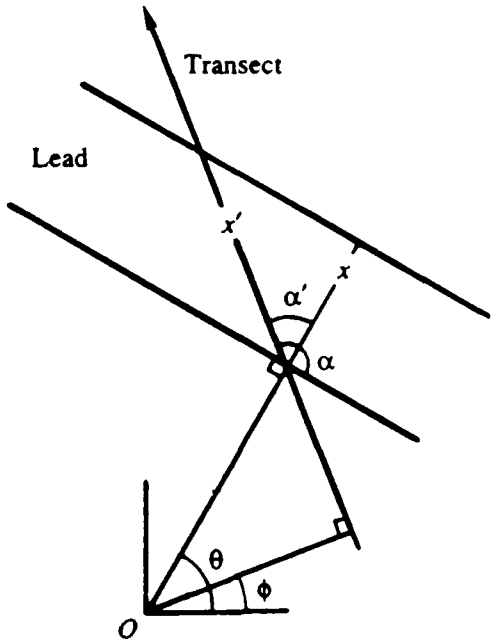

Fig. 1. The geometrical relationships between a lead and a transect. See text for definition of angles and length variables.

Finally, define $A' = |\pi/2 - A|$ to be the crossing angle (α' in Figure 1) measured between the transect and a perpendicular to the lead orientation ($0 \le A' \le \pi/2$). The relationship between apparent and actual lead widths is

$$X' = \frac{X}{\cos(A')} \qquad (1)$$

where $X \le X'$. Rearranging terms, a lead crossing angle can be determined from the lead widths by

$$A' = \cos^{-1}\left(\frac{X}{X'}\right)$$

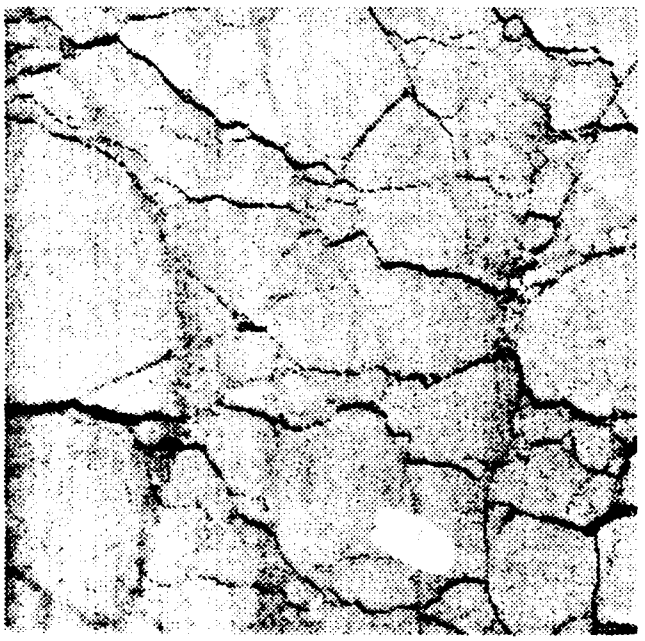

Fig. 2. Landsat MSS band 4 scene of the ice pack north of Alaska in March 1988. Area covered is approximately (80 km)^2. Field-of-view is 80 m.

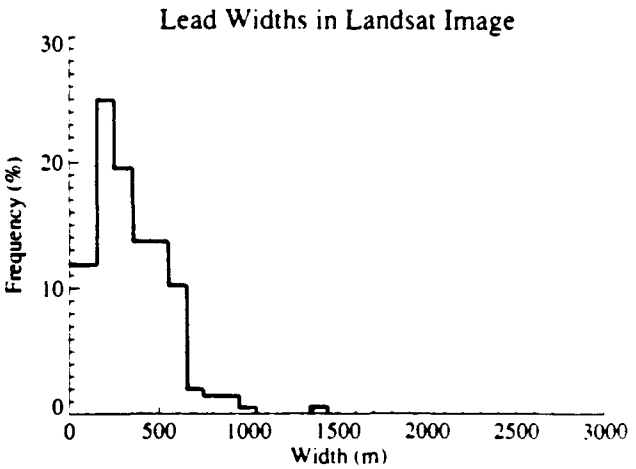

Fig. 3. Lead width distribution for the scene in Figure 2. Widths are measured along a perpendicular to the local orientation of the lead, and are grouped in 100 m bins. The mean width is 348 m, the standard deviation 201 m, and maximum width 1376 m.

The potential inaccuracies of measuring lead widths along a transect can be illustrated by randomly choosing a transect orientation and location on a satellite image. Here we provide an example with a Landsat Multispectral Scanner (MSS) band 4 (0.5-0.6 μm) scene of the Beaufort Sea, March 1988 (Figure 2). The pixel size is 80 m; image size is 80 x 80 km, a subset of a Landsat scene. To increase the sample size of lead widths measured along the transect, multiple transects of the same orientation are placed randomly on the image. It is assumed that the pattern of leads is similar beyond the image boundaries. Processing of the Landsat data for the retrieval of lead statistics is as follows. A dynamic threshold procedure is applied that estimates the probability density function of a mixture population (lead/ice) for small regions within the image, and a binary image results. Valid lead fragments are identified, where "valid" refers to a linear feature for which a meaningful width and orientation can be determined. Linearity is determined through correlation/regression analysis. Lead widths are measured perpendicular to the regression line, every kilometer along the lead length, and the slope of the regression line is a measure of the

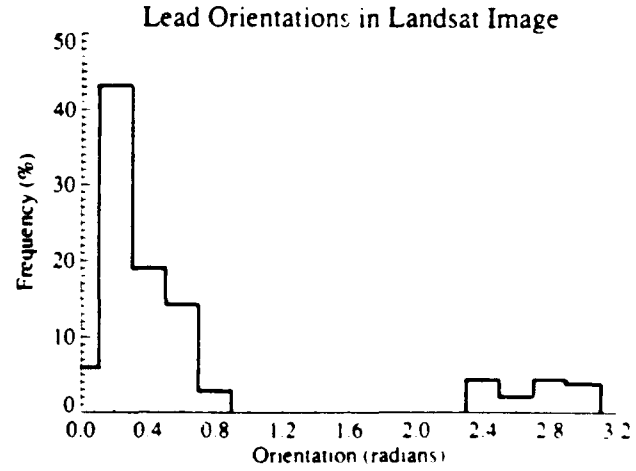

Fig. 4. Lead orientations for the scene in Figure 2. The mean orientation is 0.67^r (38.4°) with standard deviation 0.87^r (49.8°).

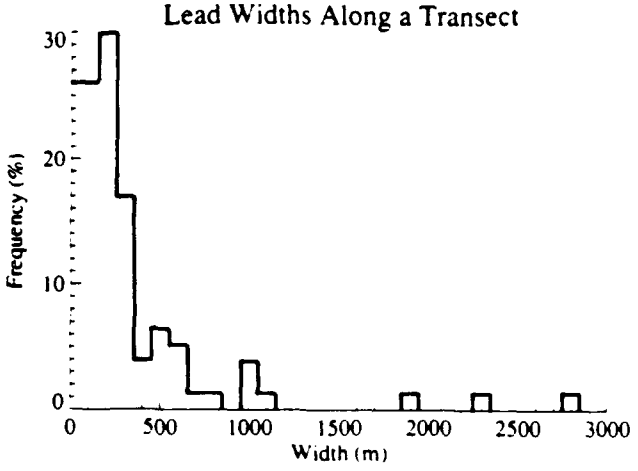

Fig. 5. Lead widths from a randomly chosen transect across Figure 2. Transect orientation is 3.0^r (172°) or approximately south-southwest to north-northeast where the top of the image is north. The mean width is 368 m, the standard deviation 474 m, and maximum width 2818 m.

lead orientation. Further details of this procedure are given in *Key et al.* [1990].

The distribution of these actual lead widths x is shown in Figure 3 and orientations θ in Figure 4. The mean lead orientation is 0.67 radians (38°, approximately southeast to northwest where the top of the image is north). For a transect orientation ϕ=3.0 radians (172°, south-southwest to north-northeast), the distribution of apparent lead widths x' is illustrated in Figure 5, with crossing angles α' shown in Figure 6. The mean actual width is 348 m with a standard deviation of 201 m, while the mean apparent width is 368 m with a standard deviation of 474 m. Additionally, the maximum actual lead width in the image is 1376 m, while the maximum width measured along the transect is 2818 m. With a transect orientation of 0.13 radians (7.4°) the difference between the actual and apparent mean widths is 139 m and the maximum width is 2670 m. From this example it is clear that significant errors can result from sampling along a transect. The following section presents a method to assess this error.

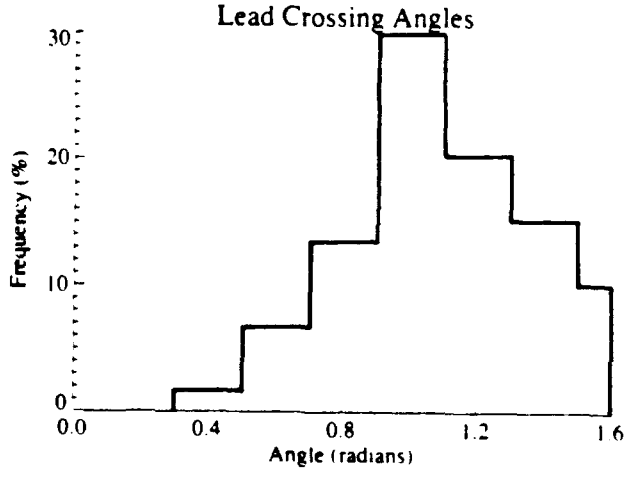

Fig. 6. Lead crossing angles for a transect across Figure 2. Transect orientation is the same as in Figure 5. The mean crossing angle is 1.09^r (62°) with standard deviation 0.23^r (13°).

3. PROBABILITY MODELS

Theorems of stochastic geometry that are applicable here have been developed through the study of fibers as a stationary random process in the plane. If we use this analogy with lead networks, then after *Stoyan et al.* [1987, p. 240] the df of intersection angles is

$$F_A(\alpha) = \frac{\int_{\phi}^{\phi+\alpha} \sin(\theta' - \phi)\, dF_\Theta(\theta')}{\int_0^{\pi} |\sin(\theta' - \phi)|\, dF_\Theta(\theta')} \qquad (2)$$

where $F_A(\alpha)$ is the probability of intersection angles between 0 and α, $F_\Theta(\theta)$ is distribution function for lead orientations, $dF_\Theta(\theta) = f_\Theta(\theta)\, d\theta$, α increases in an anticlockwise sense, and in the integral $F_\Theta(\pi + \alpha) = 1 + F_\Theta(\alpha)$. The pdf $f_\Theta(\theta)$ may be an assumed mathematical distribution or may be based on an observed rose of direction.

If the leads are isotropic then the corresponding orientations have a simple uniform probability distribution in the interval $0 \le \theta < \pi$; i.e., $f_\Theta(\theta)=1/\pi$ for all θ. In this case the distribution of intersection angles is independent of the transect orientation. The probability of crossing a lead that is oriented across the transect ($\alpha \to \pi/2$) is greater than for one running more parallel ($\alpha \to 0$ or π). The associated intersection angles have density

$$f_A(\alpha) = \tfrac{1}{2} \sin \alpha \quad , 0 \le \alpha \le \pi$$

which is not uniform but is symmetrical about $\alpha = \pi/2$. The corresponding distribution function is

$$F_A(\alpha) = \int_0^{\alpha} f_A(\psi)\, d\psi = \tfrac{1}{2}(1 - \cos \alpha) \quad , 0 \le \alpha \le \pi$$

which is a special case of (2) for $f_\Theta(\theta) = 1/\pi$. In the anisotropic (preferred orientation) case we use (2) for the distribution of intersection angles, and the corresponding densities are determined numerically.

Two different intersection angles correspond to each crossing angle so that the distribution and density functions for the crossing angle are

$$\begin{aligned} F_{A'}(\alpha') &\equiv P[A' \le \alpha'] \\ &= P[|\tfrac{\pi}{2} - A| \le \alpha'] \\ &= P[-\alpha' \le (A - \tfrac{\pi}{2}) \le \alpha'] \\ &= P[(\tfrac{\pi}{2} - \alpha') \le A \le (\tfrac{\pi}{2} + \alpha')] \\ &= F_A(\tfrac{\pi}{2} + \alpha') - F_A(\tfrac{\pi}{2} - \alpha') \end{aligned}$$

and

$$f_{A'}(\alpha') = \frac{dF_{A'}}{d\alpha'} = f_A(\tfrac{\pi}{2} + \alpha') + f_A(\tfrac{\pi}{2} - \alpha')$$

which in the isotropic case yields $F_{A'}(\alpha') = \sin \alpha'$ and $f_{A'}(\alpha') = \cos \alpha'$.

3.1. *Width Distributions*

An expression for the joint density function of the apparent and actual lead widths can be derived. Suppose that the joint pdf of X and A' are known, which will be $f_{X,A'}(x,\alpha') = f_X(x) f_{A'}(\alpha')$ if the two variables are independent. Then if Y and Z are two new random variables that are functions of X and A' such that $Y = X$ and $Z = X' = X/\cos A'$, then the joint pdf of Y and Z can be computed using a standard theorem [*Ross*, 1984, p. 217]:

$$f_{Y,Z}(y,z) \equiv f_{X,X'}(x,x')$$
$$= f_{X,A'}[x,\cos^{-1}(\frac{x}{x'})]\ \frac{x}{x'}\ [(x')^2 - x^2]^{-1/2}$$
$$= f_X(x)\ f_{A'}[\cos^{-1}(\frac{x}{x'})]\ \frac{x}{x'}\ [(x')^2 - x^2]^{-1/2} \quad (3)$$

The first of these expressions is valid whether or not X and A' are independent. If, however, future research indicates that large leads are oriented differently than small leads, for example, then the joint density function must be determined in another manner (possibly from observations). Using (3), the pdf of apparent lead widths can be obtained:

$$f_{X'}(x') = \int_0^\infty f_{X,X'}(x,x')\ dx$$
$$= \int_0^{x'} f_X(x)\ \{f_{A'}[\cos^{-1}(\frac{x}{x'})]\ \frac{x}{x'}$$
$$\times\ [(x')^2 - x^2]^{-1/2}\}\ dx \quad (4)$$

The df of apparent lead widths can be obtained by integrating (4) or by conditioning on the value of X, again assuming that X and A' are independent. The latter method yields

$$F_{X'}(x') = \int_0^{x'} F_{A'}[\cos^{-1}(\frac{x}{x'})]\ f_X(x)\ dx \quad (5)$$

which is based on the df rather than the pdf of A'.

Determining the distribution of actual lead widths given the apparent lead width distribution must be approached differently. Letting $Y = 1/\cos A'$, then (1) can be rewritten as

$$X' = XY$$
$$\log X' = \log X + \log Y$$

X and A' are assumed to be independent, hence so are $\log X$ and $\log A'$, so that $\log X'$ is a sum of two independent random variables. This allows us to write

$$f_{\log X'} = f_{\log X} * f_{\log Y} \quad (6)$$

or

$$F_{\log X'} = F_{\log X} * f_{\log Y} \quad (7)$$

where the asterisk represents convolution [*Ross*, 1984, p. 202]. The Laplace transform may be used with either (6) or (7). The Fourier transform may be used with (6) but not with (7) because the pdfs are absolutely integrable but the df is not. Using $\varphi[f]$ to denote the Fourier transform of f, then with (6)

$$\varphi[f_{\log X'}] = \varphi[f_{\log X} * f_{\log Y}] = \varphi[f_{\log X}]\varphi[f_{\log Y}]$$
$$f_{\log X} = \varphi^{-1}\left\{\frac{\varphi[f_{\log X'}]}{\varphi[f_{\log Y}]}\right\}$$

from which the actual lead width distribution is

$$f_X(x) = \frac{1}{x}\ \varphi^{-1}\left\{\frac{\varphi[f_{\log X'}]}{\varphi[f_{\log Y}]}\right\}(\log x) \quad (8)$$

The derivation of (8) is given in the appendix. This expression shows that when the appropriate transforms exist, then the pdf of X is uniquely determined in terms of the pdfs of X' and A'. However, it is only useful for computations if the Fourier transforms and inverse transforms shown can be performed analytically. This is because in practice the inverse transform is an array of numbers that must be evaluated at $\log x$, which becomes a sampling problem with discrete data; i.e., a very large number of observations sampled at small intervals would be necessary for any reasonable degree of success with this approach.

Fortunately, there is another way to approach the problem. Referring back to (4) and (5), $f_{X'}$ and $F_{X'}$ can be viewed as the result of applying an integral operator to f_X. The functions can be discretized as arrays and the integral in (5) approximated as a sum:

$$F_{X'}(j) = \Delta \sum_{i=1}^{j} F_{A'}(j,i)\ f_X(i), \quad (9)$$
$$i, j \in [1,N],\ x = i\Delta,\ y = j\Delta$$

where $F_{A'}(j,i) = F_{A'}[\cos^{-1}(i/j)]$, N is the number of discrete observations and Δ is the increment between observations. If these functions are expressed as matrices, (9) becomes

$$\boldsymbol{F}_{X'} = \Delta\ \boldsymbol{F}_{A'}\ \boldsymbol{f}_X$$
$$\boldsymbol{f}_X = \frac{1}{\Delta}\ \boldsymbol{F}_{A'}^{-1}\ \boldsymbol{F}_{X'}$$

whose derivation is given in the appendix.

3.2. *Error Distribution*

In this study the error in measured lead width is defined as X'-X (which is always positive), although other definitions such as X/X' would also be useful. Equation (3) allows us to compute the distribution of the error as follows:

$$F_{X'-X}(a) \equiv P[X'-X \le a]$$
$$= \int_0^\infty \int_x^{a+x} f_{X,X'}(x,x')\ dx'\ dx\ , \qquad a \ge 0$$

For the isotropic case

$$F_{X'-X}(a) = \int_0^\infty f_X(x)\ \sqrt{a}\left[\frac{\sqrt{2x+a}}{x+a}\right] dx$$

All moments of X'-X can be computed from $f_{X'-X}$.

4. APPLICATION

These models are now applied. First, a lead width distribution measured from sonar data is used to estimate the actual lead width distribution, for both isotropic and anisotropic orientations. Lead orientation and actual width distributions are then assumed known, and expected error in lead width is determined for a variety of situations.

Lead width distributions have been described by power laws [*Wadhams*, 1981; *Steffen*, 1987] as have floe sizes [*Rothrock and Thorndike*, 1984]. The negative exponential distribution has also been used [*Dickins et al.*, 1986]:

$$f_X(x) = e^{-x/\lambda}\ /\ \lambda$$

with mean lead width λ and variance λ^2. The exponential model implies that there are a finite number of small leads, and that the field is characterized by a length scale λ. In fact, the lead width distribution may be scale-free, in which case a power law would be appropriate. There is, of course, a lower limit imposed by the resolution of the measuring instrument, and for this reason as well as for clarity of illustrating expected values, we use the negative exponential model.

Lead orientations may be random or may have a preferred orientation. A Gaussian model is used here for

TABLE 1. Expected Error in Lead Widths (in Meters) Under a Variety of Assumed Distributions and Mean Values

Case	f_X^*	$f_{X'}$	f_Θ	ϕ^r	$E(X - X')$	$\mathrm{Var}(X - X')$
1	?	Sonar	Uniform	—	65.7	1466.1
2	λ=20m	?	Gaussian†	2.36 (135°)	3.7	3.1
3	λ=20m	?	Gaussian†	0.52 (30°)	32.5	165.9
4	λ=40m	?	Gaussian†	2.36 (135°)	4.8	6.4
5	λ=40m	?	Gaussian†	0.52 (30°)	36.0	345.3
6	λ=20m	?	Uniform	—	43.2	653.1
7	λ=40m	?	Uniform	—	64.2	1391.2

Question marks refer to the unknown distribution.
* Width distribution model is negative exponential.
† Parameters of the Gaussian model are $\mu=\pi/4^r$ (45°) and $\sigma=0.3^r$ (17°).

preferred orientations. It is recognized, however, that the actual shape of the distribution may be bimodal, where large leads with one orientation are intersected by smaller leads at another. Intersection angles of approximately 28° have been observed elsewhere [*Marko and Thomson*, 1977]. This situation is not obvious in Figure 4, although the distribution is not strictly Gaussian either.

Table 1 lists the expected error for a variety of conditions, where error is defined by the difference between the actual and measured lead widths. Case 1 considers the situation where the apparent lead width distribution is known. The apparent lead widths are based on submarine sonar data recorded by the USS QUEENFISH in August of 1970 in the central Canada Basin [*McLaren*, 1989]. Ice draft data were measured by an upward-beamed fathometer with a footprint diameter of approximately 2.7 m and a vertical accuracy of ±10 cm. Sequences of continuous points with drafts ≤30 cm constitute leads, an example of which is given in Figure 7. The apparent width distribution was determined for a 100 km section and is shown in Table 2. Given a mean apparent lead width of 60.6 m, the expected value of the error is 65.7 m with a variance of 1466.1 m^2. For cases 2-7 in Table 1 the actual width density function is assumed known, and the apparent lead width distribution is estimated. For cases 2 and 3, the crossing angle distributions are shown in Figure 8, and the error distributions in Figure 9. In the preferred orientation cases (2-5) the error means and variances are clearly dependent upon transect orientation.

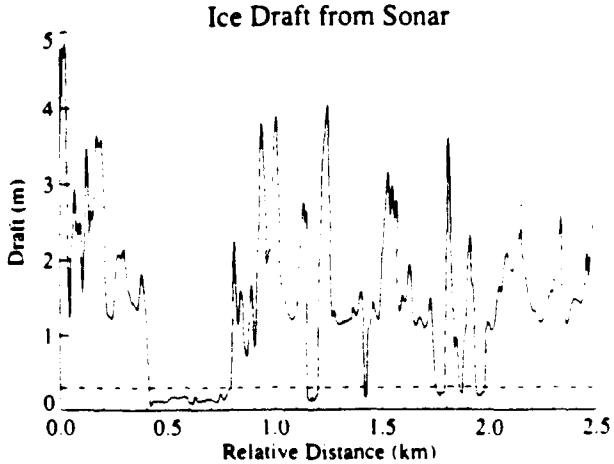

Fig. 7. Submarine sonar ice draft data for a 2.5 km section within the Canada Basin north of Alaska. Leads are defined as continuous sequences of points with drafts no greater than 0.3 m (dashed line); six leads occur in this section.

5. CONCLUSIONS

A methodology has been presented for determining width distributions of linear features from measurements along a transect through a network of such features. Both isotropic and anisotropic orientations of the linear features have been considered. In the anisotropic case, the orientation distribution of the lines must be known. In both cases if the distribution of actual widths and the orientations are viewed as independent random variables then the actual width distribution can be determined from the

TABLE 2. Lead Widths (Bin Midpoint) and Number of Leads per Bin, Measured by Submarine Sonar

Width	N	Relative Frequency
20.00	134	0.441
40.00	63	0.207
60.00	18	0.059
80.00	25	0.082
100.00	22	0.072
120.00	12	0.039
140.00	4	0.013
160.00	4	0.013
180.00	5	0.016
200.00	5	0.016
220.00	3	0.010
240.00	2	0.007
260.00	0	0.000
280.00	0	0.000
300.00	3	0.010
320.00	0	0.000
340.00	1	0.003
360.00	3	0.010

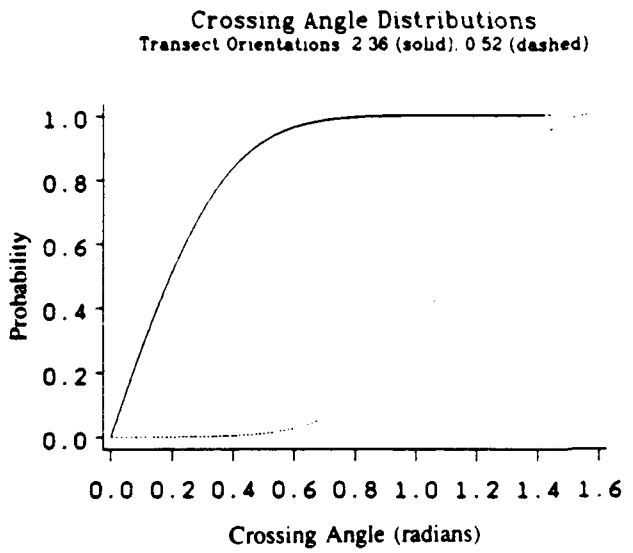

Fig. 8. The distribution functions of crossing angles F_A, for cases 2 (solid) and 3 (dashed) in Table 1.

apparent widths and vice versa. Furthermore, if the actual widths and the orientations vary jointly then the apparent width can be determined from the joint distribution. The application presented was to measurements of sea ice leads made by submarine sonar. The width distributions measured from sonar illustrated that the general shape is similar to those derived from satellite imagery, but that the errors in widths can be significant. Unfortunately, it is not possible to determine the actual error in lead widths derived from much of the archived sonar data. However, if lead "climatologies" can be compiled for various locations and seasons, or if significant relationships between lead orientation and geostrophic winds can be developed, then at least we can determine the probable error.

Of course, the potential error is not an issue if adequate two-dimensional data are available. For example, side-scan sonar may permit a more accurate retrieval of lead and keel statistics [*Wadhams*, 1988]. Sonar data with concurrent overhead imagery from aircraft or satellite is also a potentially valuable source of information. However, lead width distributions derived from satellite data may not be accurate since very small leads are not resolved. This is particularly true for medium resolution data such as that from the Defense Meteorological Satellite Program (DMSP) or the Advanced Very High Resolution Radiometer (AVHRR) on-board the TIROS-N satellites. One solution might be to retrieve the orientation information from satellite data where small lead widths cannot be resolved, and the width information from submarine sonar transects.

Other applications of this procedure are possible. For example, laser profilometer transects are analogous to sonar transects, and the methods outlined above could be used for lead and ridge spacing distributions and their associated errors. As in the illustration with Landsat data, transect sampling of satellite imagery is a natural application. Similarly, heat flux through leads is in part a function of fetch, and fetch is a function of the actual lead width and the crossing angle of the wind. If the wind direction is constant as it travels across the network of leads, then the distribution of fetches can be determined from the distribution of actual lead widths. Finally, it may be possible to estimate open water fraction over a large area from the apparent lead width and spacing distributions measured along a transect. This research is currently in progress, with results to be presented subsequently.

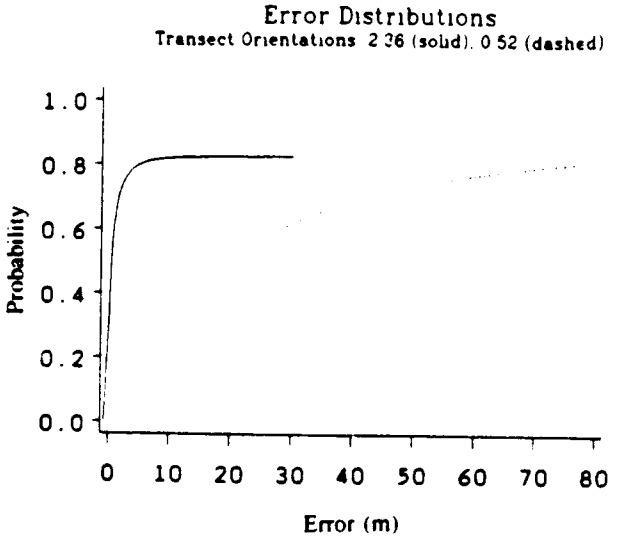

Fig. 9. The distribution functions of the lead width errors, $F_{X'-X}$, for cases 2 (solid) and 3 (dashed) in Table 1.

APPENDIX

Derivation of f_X From $f_{\log X}$

Equation (6) gives an expression for $f_{\log X}$. However, we are interested in f_X rather than $f_{\log X}$, so we use the identity

$$f_{\log Y}(\log y) = y\, f_Y(y) \tag{A1}$$

which is proven by

$$\begin{aligned} F_{\log Y}(\log y) &= P[\log Y \le \log y] \\ &= P[e^{\log Y} \le e^{\log y}] \\ &= P[Y \le y] \\ &= F_Y(y) \end{aligned}$$

The derivative of both sides with respect to y produces (A1).

Using (A1) and (6), an expression for the actual lead width distribution can be obtained:

$$f_{\log X}(\log x) = \varphi^{-1}\left\{\frac{\varphi[f_{\log X'}]}{\varphi[f_{\log Y}]}\right\}(\log x) \tag{A2}$$

$$f_X(x) = \frac{1}{x}\,\varphi^{-1}\left\{\frac{\varphi[f_{\log X'}]}{\varphi[f_{\log Y}]}\right\}(\log x)$$

Matrix Formulation of f_X

Expressing equation (5) in terms of matrices provides a way to solve for f_X. The functions can be discretized as arrays and the integral approximated as a sum as shown in (9), which is repeated here:

$$F_{X'}(j) = \Delta \sum_{i=1}^{j} F_A(j,i) f_X(i), \tag{9'}$$

$$i, j \in [1, N],\ x = i\Delta,\ y = j\Delta$$

where $F_{A'}(j,i) = F_{A'}[\cos^{-1}(i/j)]$, N is the number of discrete observations and Δ is the increment between observations. Suppose we now form an N x N matrix, M, as follows:

$$M(j,i) = \Delta\, F_{A'}(j,i), \quad 1 \le i \le j \le N$$
$$M(j,i) = 0, \quad 1 \le j < i \le N$$

where the first expression refers to elements on or below the diagonal. It follows that

$$\Delta \sum_{i=1}^{j} F_{A'}(j,i)\, f_X(i) = \sum_{i=1}^{N} M(j,i)\, f_X(i) \qquad \text{(A3)}$$

or

$$F_{X'}(j) = \sum_{i=1}^{N} M(j,i)\, f_X(i) \qquad \text{(A4)}$$

This is equivalent to the matrix equation

$$F_{X'} = M\, f_x \qquad \text{(A5)}$$

From this it can be seen that the problem is solved if M is invertible. However, since $M(j,j) = F_{A'}(j,j) = 0$ for all j (from the definition of $F_{A'}$), the matrix M has zeros on as well as above the diagonal, therefore the first row and last column contain all zeros, so that $\det(M) = 0$, or M is not invertible.

This difficulty is overcome by defining a new N-1 x N-1 matrix M_2 to be the submatrix formed by deleting the first row and last column from M. This gives

$$\begin{pmatrix} f_1 \\ f_2 \\ \cdots \\ f_{N-1} \end{pmatrix} = M_2^{-1} \begin{pmatrix} F_2 \\ F_3 \\ \cdots \\ F_N \end{pmatrix} \qquad \text{(A6)}$$

where $f_X = (f_1, f_2, \ldots, f_N)$ and $F_{X'} = (F_1, F_2, \ldots, F_N)$. Since $F_1 = 0$, it is not needed to find $f_1, \ldots f_N$. Furthermore, if N and Δ are chosen properly, then $f_N = 0$ because f is a pdf.

Acknowledgments. J. Key was supported by Office of Naval Research (ONR) grant N00014-90-J-1840. S. Peckham was supported under a NASA Global Change Research Student Fellowship. Thanks are due to A.S. McLaren for providing the submarine sonar data (ONR University Research Initiative Program contract N00014-86-K-0695). We thank D. Rothrock for comments on an earlier version of this paper.

REFERENCES

Dickins, D., A. Dickinson, and B. Humphrey, Pack ice in Canadian waters: dimensions and dynamics of leads and floes, unpublished report to the Environmental Emergencies Technology Division, Environmental Protection Service, Ottawa, Ontario, 62 pp., April 1986.

Key, J., A.J. Schweiger, and J.A. Maslanik, Mapping sea ice leads with a coupled numeric/symbolic system, in *Image Processing/Remote Sensing. ACSM/ASPRS Proceedings*, vol. 4, pp. 228-237, American Congress on Surveying and Mapping and American Society for Photogrammetry and Remote Sensing, Bethesda, MD, 1990.

Ledley, T., A coupled energy balance climate-sea ice model: impact of sea ice and leads on climate, *J. Geophys. Res.*, *93*(D12), 15,919-15,932, 1988.

Marko, J.R., and R.E. Thomson, Rectilinear leads and internal motions in the ice pack of the western Arctic Ocean, *J. Geophys. Res.*, *82*(6), 979-987, 1977.

McLaren, A.S., The under-ice thickness distribution of the Arctic Basin as recorded in 1958 and 1970, *J. Geophys. Res.*, *94*(C4), 4971-4983, 1989.

Ross, S., *A First Course in Probability*, 2nd ed., 392, Macmillan, New York, 1984.

Rothrock, D.A., and A.S. Thorndike, Measuring the sea ice floe size distribution, *J. Geophys. Res.*, *89*(C4), 6477-6486, 1984.

Steffen, K., Fractures in arctic winter pack ice (North Water, northern Baffin Bay), *Ann. Glaciol.*, *9*, 1-4, 1987.

Stoyan, D., W.S. Kendall, and J. Mecke, *Stochastic Geometry and Its Applications*, 345, John Wiley, New York, 1987.

Wadhams, P., Sea-ice topography of the Arctic Ocean in the region 70°W to 25°E, *Philos. Trans. R. Soc. London*, *302*, 45-85, 1981.

Wadhams, P., The underside of the Arctic sea ice imaged by sidescan sonar, *Nature*, *333*, 161-164, 1988.

Wadhams, P., and R.J. Horne, An analysis of ice profiles obtained by submarine sonar in the Beaufort Sea, *J. Glaciol.*, *25*(93), 401-424, 1980.

J. Key, Cooperative Institute for Research in Environmental Sciences, University of Colorado, Boulder, CO 80309-0449.

S. Peckham, Cooperative Institute for Research in Environmental Sciences, and Department of Geology, University of Colorado, Boulder, CO 80309-0449.

(Received November 8, 1990;
revised June 25, 1991;
accepted July 2, 1991.)

Arctic Ice Surface Temperature Retrieval from AVHRR Thermal Channels

J. KEY and M. HAEFLIGER

Cooperative Institute for Research in Environmental Sciences, University of Colorado, Boulder

The relationship between AVHRR thermal radiances and the surface (skin) temperature of Arctic snow-covered sea ice is examined through forward calculations of the radiative transfer equation, providing an ice/snow surface temperature retrieval algorithm for the central Arctic Basin. Temperature and humidity profiles with cloud observations collected on an ice island during 1986-1987 are used. Coefficients that correct for atmospheric attenuation are given for three Arctic clear sky "seasons", as defined through statistical analysis of the daily profiles, for the NOAA 7, 9, and 11 satellites. Modeled directional snow emissivities, different in the two split-window (11 and 12 μm) channels, are used. While the sensor scan angle is included explicitly in the correction equation, its effect in the dry Arctic atmosphere is small, generally less than 0.1 K. Using the split-window channels and scan angle, the rms error in the estimated ice surface temperature (IST) is less than 0.1 K in all seasons. Inclusion of channel 3 (3.7 μm) during the winter decreases the rms error by less than 0.003 K. The seasonal dependence of the coefficients is important, with errors in the range of 0.1 - 0.6 K when coefficients from one season are used with data from another. Similarly, mixing coefficients and data from different satellites results in average errors from 0.1 to 1.0 K. Overall, employing the IST coefficients results in increased accuracy of up to 0.6 K over SST coefficients developed for the North Atlantic and the Greenland Sea areas.

1. INTRODUCTION

Satellite data for the estimation of radiative and turbulent heat fluxes is becoming an increasingly important tool in large-scale studies of climate. One parameter needed in the estimation of these fluxes is surface temperature. Sea and land surface temperature (SST and LST) retrieval algorithms have been developed by using the thermal infrared window portion of the spectrum, with the degree of success dependent primarily upon the variability of the surface and atmospheric characteristics. The general approach to estimating surface temperature is to relate satellite observations to surface temperature observations with a regression model. Lacking sufficient observations, however, satellite radiances or brightness temperatures can be modeled by application of the radiative transfer equation. This approach is commonly used for SST retrieval [cf. *Minnett*, 1990; *Llewellyn-Jones et al.*, 1984; *Barton*, 1985]. A more complete review of SST algorithms is given by *McClain et al.* [1985]. For SST estimated using two "split-window" infrared channels (e.g., approximately 1 μm wide centered at 10.8 and 12.0 μm) an absolute accuracy of 0.5-1 K (rms error) has been obtained [*Llewellyn-Jones et al.*, 1984; *McClain et al.*, 1985]. Land surface temperature estimation is generally less accurate due to the larger variability of surface conditions, where errors of ±2-3 K are common [*Price*, 1983].

To our knowledge, little effort has been directed to the retrieval of the sea ice surface temperature (IST) in the Arctic, an area where the first effects of a changing climate are expected to be seen. The reason is not one of methodology, but rather our limited knowledge of atmospheric temperature, humidity, and aerosol profiles, the microphysical properties of polar clouds, and the spectral

characteristics of the surface types found there. In this paper we present a means to correct for the atmospheric attenuation of satellite-measured clear sky brightness temperatures used in the retrieval of snow-covered ice surface temperature from the split-window thermal channels of the advanced very high resolution radiometer (AVHRR) sensors on board three of the NOAA series satellites. These corrections are specified for three different "seasons" and as a function of satellite viewing angle and are expected to be applicable to the perennial ice pack in the central Arctic Basin (Figure 1). We do not develop a completely new methodology; instead we modify a standard procedure for use with Arctic data. In this paper it is assumed that a valid cloud-clearing algorithm exists and that only clear sky radiances are being examined. The cloud clearing problem in polar satellite data is not trivial, however. For a review of polar cloud detection algorithms, see *Key and Barry* [1989] and *Sakellariou et al.* [1992].

2. Data

Analyses are based on atmospheric temperature and humidity profiles collected by rawinsonde from a Soviet ice island (NP-26), located at approximately 85°N 170°W during 1983-1987 (Figure 1). Generally, two observations per day were collected covering a vertical range of 0 - 25 km. Profiles that have at least 10 levels are retained in the analysis. Observations include temperature, dew point depression, wind speed, and wind direction. Ice crystal precipitation is not reported. For the years 1986-1987, surface-based cloud observations are also available. These observations include low, middle, and high cloud types, height of the cloud base, and cloud fraction.

Only clear sky profiles are used in this study (1986-1987), since the satellite thermal radiances under cloudy conditions will measure cloud top temperature and a significant amount of cloud cover will affect the lower tropospheric temperature structure. Clear sky is defined to be no more than 25% cloud cover by the surface observations. Clear sky "seasons" that differ in their vertical temperature and humidity structures are then defined. The seasons are determined objectively with a squared Euclidean distance clustering algorithm; the variables are temperature and humidity at each level. To reduce the degree of statistical dependence between levels, only one measurement per kilometer was used. The resulting seasons are winter (October through March), summer (June through August), and transition (April, May, and September). This analysis was also performed with three other methods: subjectively, clustering principal component scores, and using a simple correlation method. The only difference between them was in the placement of October. By temperature alone it is grouped with the transition months. When humidity profiles are also included in the analysis, however, it is more similar to the other winter months.

The resulting mean seasonal temperature profiles for clear, cloudy (greater than 75% cloud cover), and mixed conditions are shown in Figure 2. Differences reflect not

only the near-surface temperatures but also the vertical temperature structure, which can also be seen in the monthly inversion frequencies reported by *Serreze et al.* [1991]. The effect of cloud on the surface radiation balance is evident in the clear and cloudy profiles where temperatures in the lower troposphere are higher under cloud cover in the winter and transition but lower under summer cloud cover. In addition, the summer surface inversion disappears under cloud cover. For comparison, the lowest 30 km of the standard subarctic summer and winter temperature profiles from the LOWTRAN 7 radiative transfer model data base [*Kneizys et al.*, 1988] are shown in Figure 3. The most obvious differences between the subarctic and Arctic profiles are the surface temperature and low-level inversion structure. In the Arctic profiles, standard deviation at all levels was computed for each parameter. The winter standard deviations of tropospheric clear sky temperature and dew point depression were computed for each layer, between 0 and 10 km. The maximum values occurred near the surface and were 6.8 K and 2.7 K, respectively. In summer the corresponding values are 4.5 K and 6.7 K, and in transition they are 7.9 K and 4.2 K. Interpretation of dew point depression variability requires care since the mean water vapor content is very low, generally less than 0.6 gm m^{-3}.

The AVHRRs on board the NOAA 7, 9, and 11 satellites are of interest in this study. Of the five AVHRR channels the three thermal channels (channel numbers 3, 4, and 5 centered at approximately 3.7, 11, and 12 μm) are simulated, and actual data are used for validation. NOAAs 8 and 10 are not used because they lack channel 5. First-order calibration was performed following the methods described by *NOAA* [1991] and *Lauritsen et al.* [1979]. Additional corrections were applied to the data to account for the nonlinear response of the thermal channels [*Weinreb et al.*, 1990]. Only NOAA 7 and 11 data were used in the validation. The AVHRR scan angle ranges from 0° to approximately 55°. Both local area coverage (LAC; 1.1-km field of view at nadir) and global area coverage (GAC; approximately 4 km) data are used in validation.

3. Retrieval Methodology

For the retrieval of SST a multichannel algorithm that corrects for atmospheric attenuation of upwelling radiation primarily due to water vapor absorption is commonly employed [e.g., *Barton et al.*, 1989]:

$$T_{sst} = a(\theta) + \sum_{i=3}^{5} b_i(\theta) T_i \qquad (1)$$

where $a(\theta)$ and $b_i(\theta)$ are satellite zenith angle-dependent coefficients and T_i are the satellite-measured brightness temperatures in the three AVHRR thermal channels. The coefficients are determined through a least squares regression procedure, where surface temperatures are regressed against modeled brightness temperatures. It is also possible to use differences between or ratios of two channels. Such an approach was taken by *Schluessel and*

Grassl [1990] for SST retrieval at high latitudes.

Alternatives to computing a different set of coefficients for each scan angle increment, as shown in (1), were sought. Equations that include explicitly the scan angle have been presented [cf. *McClain et al.*, 1985]. Here we use the equation

$$T_{ice} = a + bT_4 + cT_5 + d[(T_4 - T_5)\sec\theta] \quad (2)$$

for IST retrieval, where brightness temperatures are in Kelvin. The coefficients are given in the next section. The overall equation (2) produced the smallest standard error of all combinations of channels, channel differences, and scan angle functions tested, e.g., sec θ, [(1-sec θ)(T_4-T_5)], and similar variations. Although channel 3 could be included in (2), its use would be limited to winter analyses, since it measures reflected solar radiation as well as thermal emissions. The usefulness of this channel in IST retrieval is discussed in the next section.

To simulate radiances in the AVHRR thermal channels, the daily temperature and humidity profiles in each season are used with the LOWTRAN 7 (hereafter LOWTRAN) radiative transfer model [*Kneizys et al.*, 1988]. Earlier versions of LOWTRAN have been used in the retrieval of SST [e.g., *Barton et al.*, 1989]. LOWTRAN calculates atmospheric transmittance/radiance for wave numbers ranging from 0 to 50,000 cm^{-1} (0.2 μm to infinity) at a resolution of 20 cm^{-1} (for gaseous absorption) and includes calculations for multiple scattered radiation. The code may be initialized for standard or user-defined atmospheres, several cloud models, aerosol models, and specified solar and view geometry. Radiances are calculated at 5 cm^{-1} intervals (interpolated by LOWTRAN), equivalent to 0.06 μm at 11 μm. In this study, radiances are modeled for sensor scan angles from 0° to 60° in 10° increments. Atmospheric chemical composition and background tropospheric and stratospheric aerosols for the subarctic winter and summer models are used, since no such information is available from the ice islands. The optical properties of Arctic haze have not been extensively measured; model calculations [*Blanchet and List*, 1983] show that the volume extinction coefficient of Arctic haze is generally of the same order of magnitude as that of the tropospheric aerosols [*Tsay et al.*, 1989]. Therefore the use of tropospheric background aerosols is appropriate. The appropriate sensor response function (Figure 4) is applied to the calculated radiances, and radiances are then converted to brightness temperatures by inverting the Planck function at the central wavelength of the channel appropriate for the temperature range 230 - 270 K [*NOAA*, 1991]. The appendix provides additional detail on simulating satellite radiances.

The ice surface is assumed to be snow-covered year round. Directional surface emissivities for snow are modeled following the procedure of *Dozier and Warren* [1982]. Briefly, the single scattering albedo and asymmetry factor in the scattering phase function are calculated from the Mie equations, and the directional, wavelength-dependent emissivities are derived from the delta-Eddington approximation to the equation of radiative

transfer. The directional emissivities are then integrated with the response function for channel i:

$$\varepsilon_i(\theta) = \frac{\int_{\lambda_1}^{\lambda_2} \varepsilon(\lambda,\theta)\phi_i(\lambda)\, d\lambda}{\int_{\lambda_1}^{\lambda_2} \phi_i(\lambda)\, d\lambda}$$

where $\varepsilon(\lambda,\theta)$ is the emissivity in direction θ at wavelength λ and ϕ is the sensor response function which is 0 outside of $[\lambda_1,\lambda_2]$. These emissivities are given in Table 1 for NOAA 7. The difference between the integrated emissivities for the three satellites examined here is approximately 0.0001, so we only use those modeled for NOAA 7. At the wavelengths of AVHRR channels 4 and 5 the emissivity is essentially insensitive to snow grain size as well as the amount of liquid water, up to 20% of the total particle volume. Additionally, these emissivities do not change significantly over the range of temperatures encountered and therefore are applicable to the snow types encountered year round. It is possible, however, that melt ponds will contaminate the field of view during the summer. We do not adjust emissivities to account for this phenomenon.

The use of the rawinsonde profiles in modeling the surface temperature requires an additional step, since the first measurement in each profile is the shelter temperature, not the surface temperature. (In the discussions that follow, the terms "skin" and "surface" temperature are used interchangeably.) The shelter-surface temperature difference can be significant: more than 10 depending on the region and time of year [cf. *Stowe et al.*, 1988; *Rossow et al.*, 1989]. Therefore the (unknown) surface temperature for each profile is assigned a series of values representing the range of possible surface temperatures for the observed conditions during the month to which the profile belongs. An energy balance model is used to determine these surface temperatures, based on the observed range of shelter temperatures and wind speeds (the mean ±1 standard deviation) in the ice island data for each month. After *Maykut* [1982], the energy balance equation is

$$(1-\alpha)F_r - I_{ice} + F_L + \varepsilon\sigma T_{ice}^4 + F_s + F_e + F_c = 0$$

where α is the albedo, ε is the longwave emissivity, σ is the Stefan-Boltzmann constant (in W m^{-2} K^{-4}), I_{ice} is the amount of shortwave energy that penetrates the ice and does not directly heat the surface, F_r and F_l are the downwelling shortwave and longwave radiation respectively, F_s and F_e are the sensible and latent heat fluxes, respectively, and F_c is the conductive heat flux. A flux toward the surface is positive. The sensible and latent heat fluxes are dependent in part upon the wind speed, air temperature, T_{ice}, and bulk transfer coefficients. Radiative fluxes are modeled based on the mean monthly temperature and humidity ice island profiles. Ice thicknesses are taken from *Maykut* [1982]. Three new profiles are created for each original clear sky profile, where the surface temperatures are the minimum, mean, and maximum equilibrium temperatures estimated by the model. This results in seasonal sample sizes of 750, 123,

and 225 profiles for the winter, summer, and transition seasons, respectively.

4. Discussion

Coefficients for the estimation of IST are given in Tables 2-4 for NOAA 7, 9, and 11 satellites and are used with (2). Coefficients are given to five significant digits. (The rms error for using three significant digits rather than six in winter, for example, is 0.07 K, 0.003 K for four digits, and 0.0007 for five digits.) In all cases the coefficient of determination (R^2) is at least 0.98. Also shown is the root mean square (rms) error for the difference between the actual (energy balance model) surface temperature and the satellite-derived surface temperature. These errors are small—always less than 0.1 K and sometimes half that value—as a result of (1) the low water vapor content of the atmosphere and therefore little atmospheric attenuation, (2) the radiative transfer modeling approach, which does not incorporate satellite or ground-based instrument noise, and (3) natural variability in the polar atmosphere that was not captured in the ice island profiles. While the Arctic atmosphere is very dry, however, an atmospheric correction as in equation (2) is important. The uncorrected channel 4 and 5 brightness temperatures can be significantly different from the surface temperature; e.g., the mean T_{ice}-T_4 difference and its standard deviation (summer) are 0.66 and 0.43 K, 0.96 and 0.61 K for T_{ice}-T_5, -0.21 and 0.32 K for the winter channel 4 difference, and -0.23 and 0.43 K for channel 5 in winter, based on NOAA 7 simulated radiances at a surface emissivity of unity. Maximum differences are in the range of 1.7 to 2.3 K in summer and -2.5 to -3.5 in winter, for channels 4 and 5, respectively.

Due to a lack of Arctic surface and atmospheric data over the ice, it is difficult to define the area for which these coefficients apply. At present there is no evidence that temperature and humidity characteristics differ significantly over different portions of the perennial ice pack, but this cannot be confirmed. It has been found, however, that synoptic activity is quite different in the eastern Arctic (e.g., Kara Sea), affecting the strength and frequency of low-level inversions as well as humidity profiles [*Serreze et al.*, 1992]. We therefore consider these coefficients to apply to pack ice in the central Arctic Basin. The applicability of these coefficients to Antarctica is uncertain. The Arctic and Antarctic are both characterized by low temperatures, surface inversions, snow-covered surfaces, and low water vapor amounts. However, the temperatures and water vapor amounts are lower over Antarctica, although it is unknown how much lower the water vapor amounts are, by virtue of its higher elevation and lower incidence of cyclonic systems. Given this, one would expect there to be some difference between Antarctic surface temperatures estimated using the coefficients presented here and coefficients based on Antarctic temperature and humidity profiles, probably on the order of 0.1 - 0.3 K (see the discussion of SST coefficients below).

The utility of including channel 3 in surface tempera-

ture retrieval has been shown to be useful under certain conditions. For example, *Llewellyn-Jones et al.* [1984] found that triple-window simulations for the tropics were significantly better than split window, but not for temperate latitudes. *Barton* [1985] found channel 3 useful in both tropical and mid-latitude (Australia) locations. For IST retrieval, the use of channel 3 would be limited to winter analyses, since it has a reflected solar component as well as the thermal emissions. However, this channel is often noisy, especially during winter, when the amount of energy emitted at those wavelengths is small. To test its usefulness, winter is redefined as November - February, thereby avoiding a significant solar component in the upwelling radiance. Including channel 3 in (2) reduces the rms error by no more than 0.003 K or all satellites, which we do not consider a significant improvement in accuracy.

4.1. *Validation*

Validating the coefficients is difficult due to the lack of clear sky skin temperature measurements with corresponding satellite data. Therefore we use both measured and inferred surface temperatures. For example, AVHRR GAC data over the Barents Sea during July 1984 (NOAA 7) were used, with the surface temperature assumed to be near 273.15 K. This is a reasonable assumption for melting snow but may be an overestimate for ice due to its higher salinity. Over pack ice near the North Pole the mean estimated IST was 273.04 K. For a sample of pixels near the marginal ice zone with some melt ponds the mean IST was 273.27 K. Similarly, estimated ISTs in NOAA 11 AVHRR data over Greenland and Baffin Bay for July 1990 averaged 272.82 K over the ice sheet and 272.9 K over sea ice. The ice sheet location examined was the site of a Swiss Federal Institute of Technology (ETH) camp, which reported melt conditions (K. Steffen, personal communication, 1991).

GAC data during January 1984 north of Greenland were also used, where the estimated ISTs were compared to temperatures measured by drifting buoys [*Colony and Muñoz*, 1986]. There has been some discussion, although no formal study, concerning the accuracy of these buoy temperatures. During summer the buoy housing may experience radiational heating, and during winter they may be insulated by drifting snow. Comparison of estimated ISTs for 10 pixels around the location of two different buoys on January 7 yields mean temperature differences of 6 K for one buoy and 11 K for the other. The estimated ice surface temperatures were within 1 K of each other for each set of pixels. Differences of this magnitude were also reported by *Comiso* [1983, his Figure 3] for surface temperatures estimated from temperature humidity infrared radiometer (THIR) data, so that the use of the drifting buoys for validation does not appear to be useful.

Last, surface temperature measurements taken by a PRT 5 thermal radiometer during CEAREX in March 1989 are compared to NOAA 11 AVHRR data. The PRT 5 was flown on the NOAA P3 aircraft near Svalbard as part of

the Arctic Gas and Aerosol Sampling Program (AGASP). The altitude of the instrument varied between 50 m and 4 km for the "clear" sky area of coincident aircraft/satellite data. While in concept this data should be useful for validation of the ISTs, it is problematic due to (1) time differences between the aircraft flight and the satellite overpass (a few hours), (2) an assumed unit emissivity in the calculation of PRT 5 temperatures, (3) geolocation errors for both the aircraft and the satellite data, and (4) the presence of aerosols and/or ice crystals above the aircraft. The last of these conditions greatly reduced the number of areas usable for validation. The geolocation problem dictates that the comparison between the PRT 5 and AVHRR data be done over a number of pixels rather than a single pixel. Given these problems, the best situation occurred when the aircraft was at an altitude of 160 m. The mean IST for a sample of four AVHRR pixels was 258.9 K, while the mean PRT 5 temperature (adjusted for an emissivity of 0.998) of four consecutive measurements 1 km apart was 259.04 K. Given the difficulties in comparing the two data sets, these results are encouraging.

4.2. *Dependencies and Atmospheric Considerations*

A potential problem in the retrieval of IST is the presence of ice crystal haze, or "diamond dust." It is particularly difficult to detect in AVHRR data because it is usually close to the surface and exhibits similar spectral properties. Values of the visible optical depth for ice crystal haze have been reported to range from 5 to 21 for wintertime and from 0.03 to 3 for springtime [*Curry et al.*, 1990]. The effect of varying optical depth of ice crystal haze on the estimated IST is illustrated indirectly in Figure 5, which shows brightness temperature differences between AVHRR channels 4 and 5 as a function of the optical depth of ice crystal haze over two ice surfaces: 5-cm-thick ice with a surface temperature of 256.62 K and 2 m ice with a surface temperature of 235.38 K. Mean January atmospheric conditions for the central Arctic are used at a satellite scan angle of 30°. The top of the ice crystal haze layer is near the top of the inversion, which has a temperature of 248 K. Using the coefficients developed here, estimated ISTs over the 2-m ice surface for the points indicated (in order of increasing optical depth) are 235.36, 237.51, 239.57, and 246.15 K. Depending on the cloud detection algorithm used, a temperature change of more than 2°-3° would probably signify cloud, so that in this example, diamond dust with optical depths greater than 0.34 do not present a problem in IST retrieval. At smaller optical depths, however, estimated ISTs could be in error. Given the uncertainty in the frequency of occurrence and spatial extent of this phenomenon, we do not attempt to adjust for it in the coefficients presented. Admittedly, this can be an important problem at certain times of the year.

The dependence of the coefficients on sensor scan angle has been found to be important by other investigators [cf. *Barton*, 1985; *Minnett*, 1990]. This is also the case for IST retrieval, although incorporating both channels 4 and 5 in

(2) reduces the effect that increased path length at large scan angles has on the surface temperature estimation when scan angle is not taken into account explicitly. With the coefficients presented here the estimated surface temperature from (2) is very close to the surface temperature at all scan angles, while the estimated surface temperature using only channels 4 and 5 varies as a function of scan angle. Even though the differences are small, not including the scan angle explicitly results in an increased rms error of less than 0.1 K over using (2).

Coefficients in (2) were also computed assuming emissivities independent of wavelength and scan angle. In this case a different set of coefficients was produced at emissivities of 0.96 to 1.0 in increments of 0.01. Using the scan angle and wavelength dependent coefficients (Tables 2-4) with data based on fixed emissivity coefficients results in underestimates of 0.2 K for an emissivity of 1.0 and 0.6 K for an emissivity of 0.99 during summer with NOAA 7 simulated data. Since pure water has a slightly lower emissivity than pure snow (e.g., 0.992 at 11.9 μm and nadir), the estimated IST of an AVHRR pixel contaminated by summer meltponds would be incorrect by an amount somewhere between these two extremes depending on the proportion of water within the field of view.

The seasonal dependence of the coefficients is illustrated in Table 5, where coefficients from each season were applied to data from every other season. Results are shown for NOAA 9 and indicate errors between 0.1 K for transition coefficients with winter data and 0.6 K when summer coefficients are used with winter data. Similarly, the satellite dependence of the coefficients is shown in Table 6 for summer conditions. On the average, errors ranging from 0.1 to 1.0 K, depending on season, can be expected in applying coefficients derived for one satellite to data from another, the smallest errors occurring between NOAA 7 and 9 coefficients and data.

Using SST coefficients developed for the North Atlantic [*Llewellyn-Jones et al.*, 1984] and the Greenland Sea area [*Minnett*, 1990] to estimate IST would result in an underestimate of up to 0.7 K, largest in winter and at scan angles of 40° and greater. Not surprisingly, the difference is much larger (up to a 5.0 K overestimate) when tropical coefficients [*Llewellyn-Jones et al.*, 1984] are used. This comparison was made by using simulated radiances based on the directional emissivities, whereas the emissivity of the sea surface in the aforementioned studies was computed by using the Fresnel equations with the refractive index of water (actual values not given). These errors are similar to those reported by *Minnett* [1986], where SST was retrieved from North Atlantic data using coefficients from other regions.

Sensor characteristics and calibration also influence the retrieved IST. AVHRR GAC data are less noisy than LAC data and would result in a smoother IST field. Incorrect sensor calibration can produce large errors in estimated IST; errors in IST near Greenland of up to 3 K resulted from not including the nonlinear response correction in the calibration. Quantization of the signal (i.e., how much of a degree is represented by one digital count) introduces

additional error. Some of these factors affect whether or not there is a systematic difference between the estimated ISTs and the true (measured) IST—the system bias—but due to the small quantity of coincident surface/satellite measurements, the degree of influence is impossible to assess. Therefore no empirical corrections to the forward model are suggested, which would otherwise account for sensor and other factors such as radiosonde accuracy and the treatment of the stratosphere above the known profile.

5. Summary and Conclusions

The relationship between AVHRR clear sky thermal radiances and the surface (skin) temperature of central Arctic snow-covered sea ice is examined through forward calculations of the radiative transfer equation. Temperature and humidity profiles and cloud data from ice islands during 1986-1987 are used. Coefficients that correct for atmospheric attenuation are given for three Arctic clear sky "seasons," as defined through statistical analysis of the daily profiles, for the NOAA 7, 9, and 11 satellites. Modeled directional emissivities, different in the two split-window channels, are used. While the sensor scan angle is included explicitly in the correction equation, its effect in the dry Arctic atmosphere is small, generally less than 0.1 K. The coefficients presented are for use with AVHRR channels 4 and 5 (11 and 12 μm) and the sensor scan angle. With this method the rms error in the estimated ice surface temperature is less than 0.1 K in all seasons. Inclusion of channel 3 (3.7 μm) during the winter decreases the rms error by less than 0.003 K.

The seasonal dependence of the coefficients is important, with rms errors in the range of 0.1 - 0.6 K when coefficients are applied across seasons. Similarly, using coefficients from one satellite with data from another results in average errors from 0.1 to 1.0 K. Overall, employing the IST coefficients results in increased accuracy of up to 0.6 K over SST coefficients developed for the North Atlantic and the Greenland Sea areas. While this difference is small in terms of outgoing longwave radiation, it is important for long-term climate monitoring. Modeled ice crystal haze during January indicates that at small optical depths the haze may not be detected as cloud and could result in IST errors of up to 2°.

Two important problems remain in the retrieval of ice surface temperature. First, until a reliable method of cloud clearing becomes accepted by the science community, IST retrieval results will have an additional level of uncertainty. Second, coincident satellite, surface, and atmosphere measurements over sea ice must be taken across the Arctic and in all seasons before the bias of these IST coefficients can be accurately determined.

Appendix

Assuming that clouds do not contaminate the satellite scene, that the remaining atmosphere is nonscattering, and that the surface is nonblack, then the radiative transfer equation for the upward monochromatic radiance $L(\lambda,\theta)$ at wavelength λ and satellite view angle θ can be expressed as

$$L(\lambda,\theta) = \varepsilon_\lambda(\theta)B_\lambda(T_s)e^{-\sigma_\lambda} + \int_0^{\sigma_\lambda} B_\lambda[T(\sigma'_\lambda)]e^{-\sigma'_\lambda}d\sigma'_\lambda + [(1-\varepsilon_\lambda(\theta)]e^{-\sigma_\lambda}\int_{\sigma'_\lambda}^{0} B_\lambda[T(\sigma'_\lambda)]e^{-\sigma'_\lambda}d\sigma'_\lambda$$

where ε_λ is the emissivity of the surface (which is assumed equal at all λ within a channel in this study), T_s is the surface temperature in Kelvin, σ_λ is the optical depth of the slant path, and $B_\lambda(T)$ is the Planck function at temperature T. The first term on the right is the contribution from the surface, the second is from atmospheric emission, and the third represents downward atmospheric emission that has been reflected upward. The surface contribution is assumed to be the dominant one for the IST retrieval outlined in (2), which can be illustrated by estimating radiances in the two split-window channels using the clear sky Arctic mean and subarctic standard winter and summer profiles with identical surface temperatures. The maximum difference in radiances is 0.05 W m^{-2} sr^{-1}, indicating that the vertical temperature distribution of the relatively dry Arctic atmosphere plays a relatively small role in the attenuation of upwelling longwave radiation.

To simulate the satellite radiance, the radiances at wavelengths across each channel must be integrated with the sensor response function:

$$L_i = \frac{\int_{\lambda_1}^{\lambda_2} L(\lambda,\theta)\phi_i(\lambda)\,d\lambda}{\int_{\lambda_1}^{\lambda_2} \phi_i(\lambda)\,d\lambda}$$

where L_i is the channel i radiance, $\Phi_i(\lambda)$ is the channel's response function, and λ_1 and λ_2 are the lower and upper limits of the channel, i.e., where the response is 0. Using a rectangular response function defined by the half-amplitude full-width portion of the actual channel response (but with 100% response at all wavelengths) instead of the full response function results in brightness temperature differences of the order of 0.05 K in channel 4 and 0.5 K in channel 5 (January conditions). These figures are valid for two central wavelengths used in the conversion of radiance to brightness temperature: that from the full response function or one based on Planck radiances specifically for the half-amplitude function.

Acknowledgments. J. Key was supported under NASA grant NAGW-2407 (University of Washington subcontract 721566) and ONR grant N00014-90-J-1840. M. Haefliger was supported under NASA grant NAGW-2158. Thanks are due to M. Serreze and J. Kahl for providing the ice island atmospheric data (NA85RAH05066), R. Schnell for the aircraft PRT-5 CEAREX data, K. Steffen for a sample of the Greenland ETH data (which is part of an ongoing project with results to be reported subsequently), and R. Lindsay and the anonymous reviewers for a thorough review of an earlier version of the manuscript.

REFERENCES

Barton, I. J., Transmission model and ground-truth investigation of satellite-derived sea surface temperatures, *J. Clim. Appl. Meteorol.*, *24*, 508-516, 1985.

Barton, I. J., A. M. Zavody, D. M O'Brien, D. R. Cutten, R. W. Saunders, and D. T. Llewellyn-Jones, Theoretical algorithms for satellite-derived sea surface temperatures, *J. Geophys. Res.*, *94*(D3), 3365-3375, 1989.

Blanchet, J., and R. List, Estimation of optical properties of arctic haze using a numerical model, *Atmos. Ocean*, *21*, 444-465, 1983.

Colony, R., and E.A. Muñoz, Arctic Ocean buoy program data report: 1 January 1984 - 31 December 1985, 277 pp., Polar Sci. Center, Appl. Phys. Lab., Univ. Wash., Seattle, Oct. 1986.

Comiso, J. C., Sea ice effective microwave emissivities from satellite passive microwave and infrared observations, *J. Geophys. Res.*, *88*(C12), 7686-7704, 1983.

Curry, J. A., F. G. Meyer, L. F. Radke, C. A. Brock, and E. E. Ebert, Occurrence and characteristics of lower tropospheric ice crystal in the Arctic, *Int. J. Climatol.*, *10*, 749-764, 1990.

Dozier, J., and S. G. Warren, Effect of viewing angle on the infrared brightness temperature of snow, *Water Resour. Res.*, *18*(5), 1424-1434, 1982.

Key, J., and R. G. Barry, Cloud cover analysis with arctic AVHRR data, 1, Cloud detection, *J. Geophys. Res.*, *94*(D15), 18,521-18,535, 1989.

Kneizys, F. X., E. P. Shettle, L. W. Abreu, J. H. Chetwynd, G. P. Anderson, W. O. Gallery, J. E. A. Selby, and S. A. Clough, Users guide to LOWTRAN 7, *Rep. AFGL- TR-88-0177*, 137 pp, Environmental Research Papers, No. 1010, Air Force Geophys. Lab., Bedford, Mass., 1988.

Lauritson, L., G. G. Nelson, and R. W. Port, Data extraction and calibration of TIROS-N/NOAA A-G radiometer, *NOAA Tech. Memo., NESS 107*, 81 pp., Natl. Oceanic and Atmos. Admin., Boulder,Colo., 1979.

Llewellyn-Jones, D. T., P. J. Minnett, R. W. Saunders, and A. M. Zavody, Satellite multichannel infrared measurements of sea surface temperature of the northeast Atlantic Ocean using AVHRR/2, *Q. J. R. Meteorol. Soc.*, *110*, 613-631, 1984.

Maykut, G. A., Large-scale heat exchange and ice production in the central Arc , *J. Geophys. Res.*, *87*(C10), 7971-7984, 1982.

McClain, E. P., W. G. Pichel, and C. C. Walton, Comparative performance of AVHRR-based multichannel sea surface temperatures, *J. Geophys. Res.*, *90*, 11,587-11,601, 1985.

Minnett, P. J., A numerical study of the effects of anomalous North Atlantic atmospheric conditions on the infrared measurement of sea surface temperature from space, *J. Geophys. Res.*, *91*(C7), 8509-8521, 1986.

Minnett, P. J., The regional optimization of infrared measurements of sea surface temperature from space, *J. Geophys. Res.*, *95*(C8), 13,497-13,510, 1990.

NOAA, NOAA Polar Orbiter Data User's Guide, U.S. Dept. of Commer., Nat. Ocean. and Atmos. Admin., NESDIS, Boulder, Colo., Feb. 1991.

Price, J. C., Estimating surface temperatures from satellite thermal infrared data—A simple formulation for the atmospheric effect, *Remote Sens. Environ.*, *13*, 353-361, 1983.

Rossow, W. B., L. C. Garder, and A. A. Lacis, Global, seasonal cloud variations from satellite radiance measurements, I, Sensitivity of analysis, *J. Climate*, *2*, 419-458, 1989.

Sakellariou, N. K., H. G. Leighton, and Z. Li, Identification of clear and cloudy pixels at high latitudes from AVHRR radiances, *Int. J. Remote Sen.*, in press, 1992.

Schluessel, P., and H. Graasl, SST in polynias: A case study, *Int. J. Remote Sens.*, *11*(6), 933-945, 1990.

Serreze, M. C., J. D. Kahl, and R. C. Schnell, Low-level temperature inversions of the Eurasian Arctic and comparisons with Soviet drifting station data, *J. Climate*, in press, 1992.

Stowe, L. L., C. G. Wellemeyer, T. F. Eck, H. Y. M. Yeh, and The Nimbus-7 Cloud Data Processing Team, Nimbus-7 global cloud climatology, I, Algorithms and validation, *J. Climate*, *1*, 445-470, 1988.

Tsay, S.-C., K. Stamnes, and K. Jayaweera, Radiative energy budget in the cloudy and hazy arctic, *J. Atmos. Sci.*, *46*(7), 1002-1018, 1989.

Weinreb, M. P., G. Hamilton, and S. Brown, Nonlinearity corrections in calibration of advanced very high resolution radiometer infrared channels, *J. Geophys. Res.*, *95*(C5), 7381-7388, 1990.

J. Key and M. Haefliger, Cooperative Institute for Research in Environmental Sciences, Division of Cryosphric and Polar Processes, University of Colorado, Boulder, Colorado 80309-0449.

(Received October 31, 1991;
revised January 13, 1992;
accepted January 15, 1992.)

Paper number 92JD00348.
0148-0227/92/92JD-00348 $05.00

KEY AND HAEFLIGER: ICE SURFACE TEMPERATURE RETRIEVAL

KEY AND HAEFLIGER: ICE SURFACE TEMPERATURE RETRIEVAL

KEY AND HAEFLIGER: ICE SURFACE TEMPERATURE RETRIEVAL

KEY AND HAEFLIGER: ICE SURFACE TEMPERATURE RETRIEVAL

KEY AND HAEFLIGER: ICE SURFACE TEMPERATURE RETRIEVAL

KEY AND HAEFLIGER: ICE SURFACE TEMPERATURE RETRIEVAL

KEY AND HAEFLIGER: ICE SURFACE TEMPERATURE RETRIEVAL

KEY AND HAEFLIGER: ICE SURFACE TEMPERATURE RETRIEVAL

KEY AND HAEFLIGER: ICE SURFACE TEMPERATURE RETRIEVAL

KEY AND HAEFLIGER: ICE SURFACE TEMPERATURE RETRIEVAL

KEY AND HAEFLIGER: ICE SURFACE TEMPERATURE RETRIEVAL

KEY AND HAEFLIGER: ICE SURFACE TEMPERATURE RETRIEVAL

KEY AND HAEFLIGER: ICE SURFACE TEMPERATURE RETRIEVAL

KEY AND HAEFLIGER: ICE SURFACE TEMPERATURE RETRIEVAL

KEY AND HAEFLIGER: ICE SURFACE TEMPERATURE RETRIEVAL

KEY AND HAEFLIGER: ICE SURFACE TEMPERATURE RETRIEVAL

TABLE 1. Angular Emissivities of Snow in NOAA 7 AVHRR Channels 4 and 5

Scan Angle	Channel 4 Emissivity	Channel 5 Emissivity
0	0.9988	0.9961
10	0.9987	0.9958
20	0.9984	0.9949
30	0.9977	0.9933
40	0.9968	0.9908
50	0.9955	0.9872

TABLE 2. Winter, Transition, and Summer Season Coefficients and rms Error Based on AVHRR Channels 4 and 5 for NOAA 7

Season	*a*	*b*	*c*	*d*	rms
Winter	-3.38568	6.28508	-5.27306	-2.45291	0.102
Transition	-3.77780	4.73209	-3.71850	-1.40115	0.074
Summer	-0.47429	3.77483	-2.77389	-0.56024	0.057

Season coefficients based on equation (2).

TABLE 3. Winter, Transition, and Summer Season Coefficients and rms Error Based on AVHRR Channels 4 and 5 for NOAA 9

Season	a	b	c	d	rms
Winter	-5.82059	7.81491	-6.79284	-3.34169	0.127
Transition	-6.06238	5.64562	-4.62267	-1.91927	0.089
Summer	0.49995	4.12165	-3.12356	-0.68087	0.067

Season coefficients based on equation (2).

TABLE 4. Winter, Transition, and Summer Season Coefficients and rms Error Based on AVHRR Channels 4 and 5 for NOAA 11

Season	*a*	*b*	*c*	*d*	rms
Winter	-5.39436	5.46800	-4.45233	-1.45853	0.071
Transition	-5.35487	4.47913	-3.46285	-0.97128	0.053
Summer	-1.76899	3.66554	-2.66249	-0.39676	0.053

Season coefficients based on equation (2).

TABLE 5. The rms Error in Applying Coefficients (NOAA 9) Developed for One Season to Data From Another

	Data from		
Coefficients	Winter	Summer	Transition
Winter	0	0.403	0.128
Summer	0.587	0	0.342
Transition	0.117	0.219	0

TABLE 6. The rms Error in Applying Coefficients (Summer) Developed for One Satellite to Data From Another

	Data from		
Coefficients	NOAA 7	NOAA 9	NOAA 11
NOAA 7	0	0.272	0.655
NOAA 9	0.296	0	1.017
NOAA 11	0.682	0.961	0

Figures

Fig. 1. Average minimum (solid) and maximum (dashed) sea ice extent in the Arctic Ocean. Also shown is the area covered by the NP-26 drifting ice island.

Fig. 2. Clear, cloudy, and mixed temperature profiles for the ice island data during winter (October - March), transition (April, May, September) and summer (June - August).

Fig. 3. Standard subarctic winter and summer temperature profiles.

Fig. 4. Response functions for AVHRR channels 4 and 5 on NOAA 7, NOAA 9, and NOAA 11.

Fig. 5. Brightness temperature difference between AVHRR channels 4 and 5 as a function of the optical depth of ice crystal haze over two ice surfaces: 5-cm-thick ice with a surface temperature of 256.6 K and 2-m ice with a surface temperature of 235.4 K. Mean January atmospheric conditions for the central Arctic are used. The top of the ice crystal haze layer is near the top of the inversion, which has a temperature of 248.0 K. Satellite scan angle is 30°. Estimated ISTs over the 2-m ice surface for the points indicated (in order of increasing optical depth) are 235.36, 237.51, 239.57, and 246.15 K.

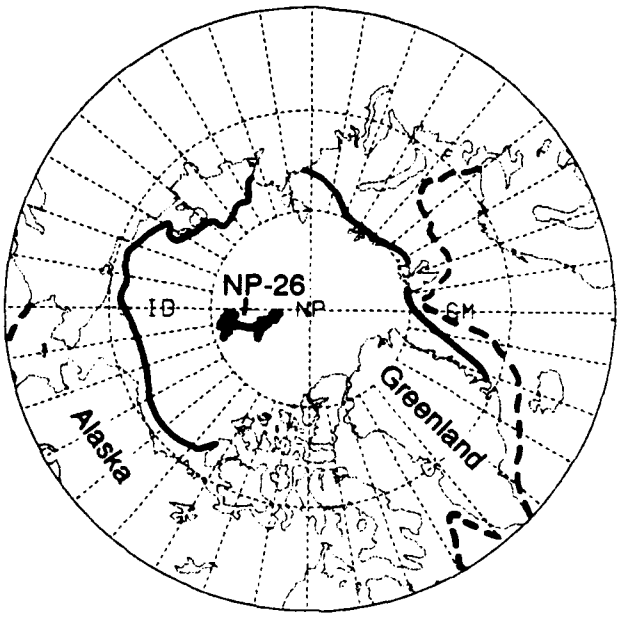
NP-26
IB
NP
GM
Alaska
Greenland

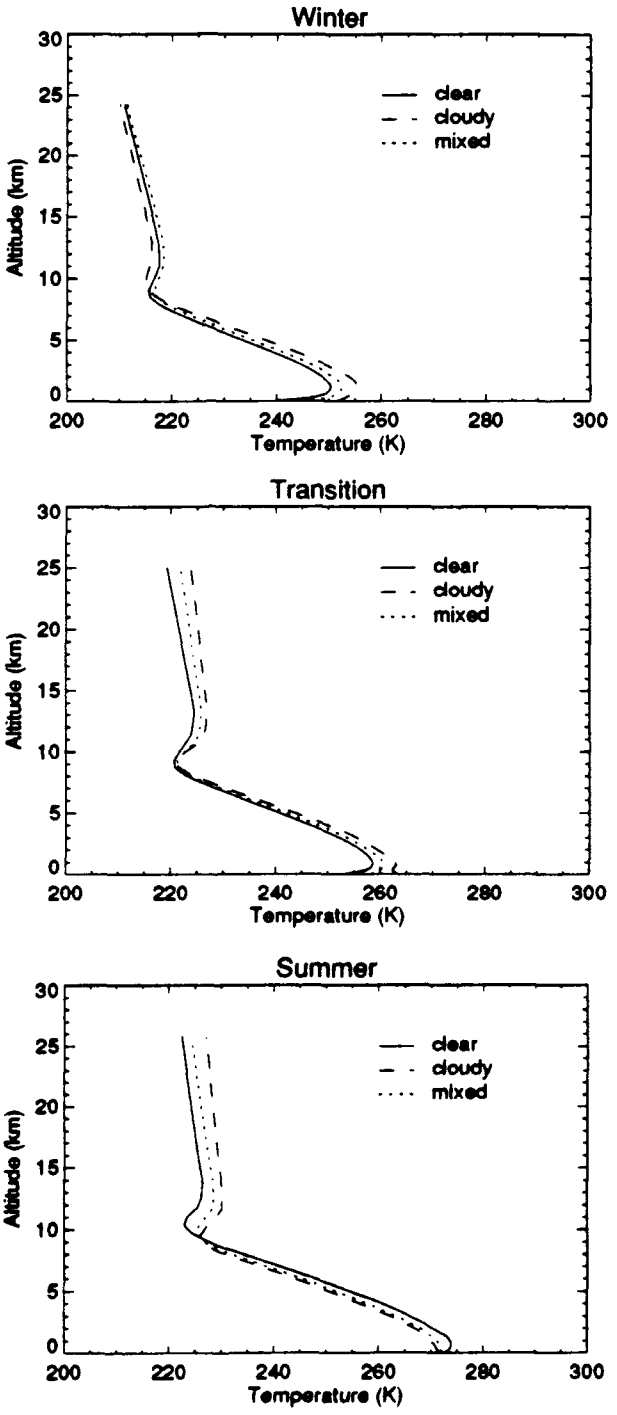
Winter
clear
cloudy
mixed
Altitude (km)
Temperature (K)
Transition
clear
cloudy
mixed
Altitude (km)
Temperature (K)
Summer
clear
cloudy
mixed
Altitude (km)
Temperature (K)

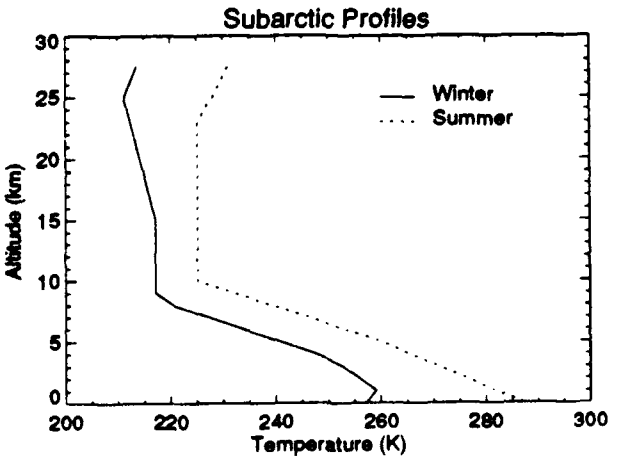
Subarctic Profiles
Winter
Summer
Altitude (km)
30
25
20
15
10
5
0
200
220
240
260
280
300
Temperature (K)

(3)

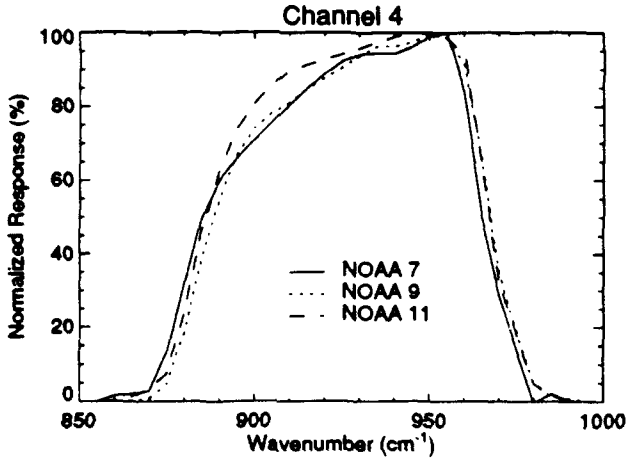
Channel 4
Normalized Response (%)
100
80
60
40
20
0
850
900
950
1000
Wavenumber (cm-1)
NOAA 7
NOAA 9
NOAA 11

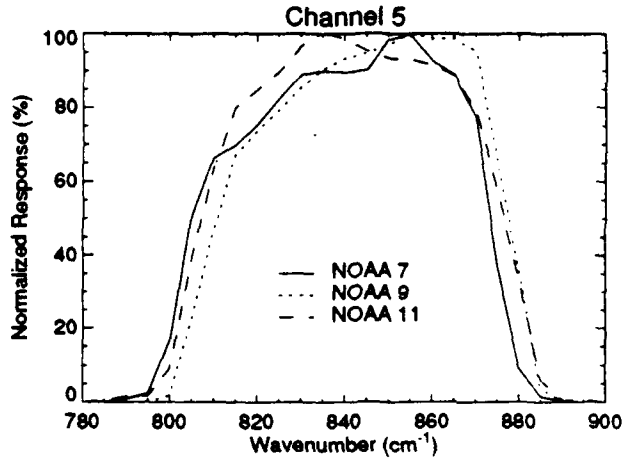
Channel 5
Normalized Response (%)
100
80
60
40
20
0
780
800
820
840
860
880
900
Wavenumber (cm-1)
NOAA 7
NOAA 9
NOAA 11

(4)

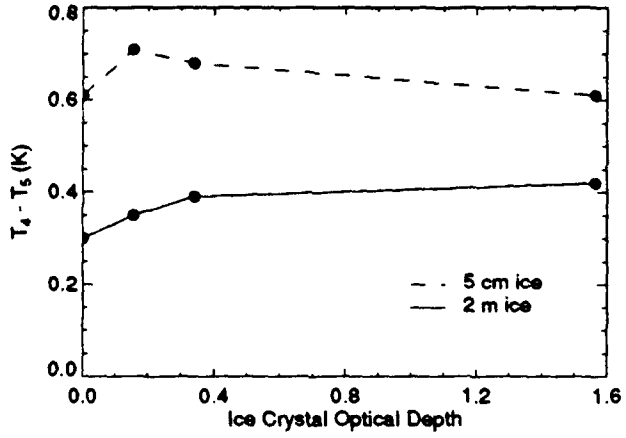
0.8
0.6
0.4
0.2
0.0
$T_s - T_5$ (K)
0.0
0.4
0.8
1.2
1.6
Ice Crystal Optical Depth
5 cm ice
2 m ice

(5)

The Detectability of Sea Ice Leads in Satellite Data as a Function of Atmospheric Conditions and Measurement Scale

J. Key, R. Stone, J. Maslanik, and E. Ellefsen

Division of Cryospheric and Polar Processes
Cooperative Institute for Research in Environmental Sciences
University of Colorado
Boulder, CO 80309-0449

Annals of Glaciology
(Prepared for the meeting of the
International Glaciological Society
Boulder, CO, May 1992)

March 12, 1992

ABSTRACT

The release of heat from sea ice leads is an important component of the heat budget in the Arctic, but their impact on regional scale climate is difficult to assess without more information on their distribution in both space and time. Remote sensing of leads using satellite data, specifically AVHRR thermal and Landsat visible imagery, is examined with respect to one lead parameter: lead width. Atmospheric effects are illustrated through the concept of thermal contrast transmittance, where the brightness temperature contrast between leads of various ice thicknesses and the surrounding multiyear ice are simulated using a radiative transfer model. Calculations are made as a function of aerosol, ice crystal precipitation, and cirrus cloud optical depths. For example, at ice crystal optical depths of more than 0.3 under mean January conditions in the central Arctic, the split-window brightness temperature differences between 2 m and 5 cm thick ice are similar to the ice temperature variability so that there would be insufficient contrast to distinguish a lead from the surrounding ice. The geometrical aspects of the sensor are also simulated so that the effect of sensor field-of-view on retrieved lead width statistics can be assessed. This is done using Landsat data degraded to AVHRR pixel sizes.

INTRODUCTION

Sea ice leads (linear openings in the ice pack) are an important component in local scale heat exchange in the Arctic, providing a significant source of heat and moisture to the atmosphere. Unfortunately, their impact on regional scale climate is difficult to assess without more information on their frequency of occurrence in both space and time. The use of satellite data, and in particular the thermal channels of the Advanced Very High Resolution Radiometer (AVHRR), for the detection and mapping of leads has been suggested but its utility is questionable because of its relatively low resolution (1.1 km at nadir) and the influence of the intervening atmosphere on upwelling radiation. It is necessary, therefore, to understand how sensor characteristics, atmospheric properties, and surface conditions influence the detection and interpretation of sea ice leads in AVHRR and other satellite data. We seek

to determine the sources and magnitudes of errors inherent in the measurements and how lead statistics change with the different spatial resolutions of existing and future sensors. Specifically, we address the following issues: What is actually being measured by these sensors? To what extent do surface, atmosphere, and sensor factors affect lead observations and image interpretations? How does lead detection depend on ice thickness as a function of sensor response, surface temperatures, and atmospheric conditions? Since the temperature contrast between open water and ice provides a means to map leads using thermal imagery, to what degree does this contrast affect the apparent width of a lead and our ability to detect it? How do atmospheric, boundary layer, and solar zenith angle effects combine with surface conditions and viewing geometry to determine the thresholds of lead detection?

To address these questions our approach includes both modeling and empirical studies. The radiative transfer modeling is done for the purpose of simulating the satellite sensor response under a variety of atmospheric and surface conditions. The empirical studies include a comparison of lead statistics determined in imagery of varying scales (e.g., AVHRR, Landsat, and OLS data) and the use of lead statistics derived from low resolution imagery to estimate characteristics of the distributions obtained in the high resolution images. In this paper we discuss both the empirical and modeling studies with respect to lead width, which is defined as the distance across a lead along a line perpendicular to the local orientation of the lead.

2. THERMAL CONTRAST BETWEEN LEADS AND THE SURROUNDING ICE

Atmospheric and view angle effects are modeled under a variety of conditions to simulate sensor response in order to gain a better understanding of how leads might appear in the satellite data under varying surface and atmospheric conditions. With this knowledge, it may be possible to estimate the smallest resolvable lead under a given set of surface/atmospheric/sensor resolution and view angle conditions. Emphasis is on the AVHRR thermal channels (3: centered at approximately 3.7 μm, 4: 11 μm, 5: 12 μm).

To simulate radiances measured by the sensor, the LOWTRAN 7 (hereafter LOWTRAN) atmospheric transmittance/radiance model (*Kneizys et al.*, 1988) is used. LOWTRAN calculates atmospheric transmittance/radiance for wave numbers ranging from 0 to 50,000 cm^{-1} (0.2μm to infinity) at a resolution of 20 cm^{-1}, and includes calculations for multiple scattered radiation. The code may be initialized for standard or user-defined atmospheres, several cloud models, aerosol models, and specified solar and view geometry. Analyses are based on atmospheric temperature and humidity profiles collected by radiosonde from the Soviet ice islands RVAB (approximately 80°N 160°W) during 1979-83 and EMIO (approximately 87°N 175°E) during 1983-1987. Generally two observations per day were collected covering a vertical range of 0 to 25 km. Profiles that had more than 10 levels were retained in the analyses. Pertinent observations include temperature and dew point depression. Results for mean January conditions are presented here.

LOWTRAN calculations were made over a range of 0.55 micron optical depths for 3 prescribed surface temperatures used to characterize different lead types (open or refrozen) and a fourth to represent the "background" scene consisting of 2 meter thick ice. These temperatures were estimated using a surface energy balance approach (*Maykut*, 1982) to characterize the open leads at 271 K, leads covered by 5 cm thick ice (257 K) and 15 cm thick ice (248 K). The thick ice has a skin temperature of 235 K in all model calculations. The model was run for satellite viewing angles of 0° (nadir), 20° and 50° and accounted for differences in directional emissivity at each central wavelength of the AVHRR channels. Temperature and humidity profiles were based on the mean January ice island soundings discussed above. All simulated radiances were converted to brightness temperatures for ease of analysis and intercomparisons. Examples of the results are shown in Figure 1 for two commonly observed conditions in the Arctic, ice crystal precipitation and haze in the boundary layer. Figure 1a is a composite of results at 50° viewing angle showing the behavior of channel brightness temperatures (numbered 3, 4 and 5 on the plots) for simulations assuming each of the surface temperatures defined above. A hypothetical cirrus

cloud of varying optical depth was inserted in the lowest 1 km of the atmosphere to simulate the effects of "ice crystal precipitation" which is a common feature affecting the radiative balance of the lower troposphere in the Arctic. Regardless of the underlying surface type the simulated brightness temperatures rapidly converge to the 248 K blackbody radiating temperature of the "cloud top" level as optical depth increases. Note that because all three channels are centered in window regions of the spectrum, surface temperatures are well simulated at zero optical depths. Maximum brightness temperature differences exist between the channels at around optical depth 0.5 to 0.8. If satellite radiances can be measured accurately, these differences may be used to delineate leads when optically thin ice crystal precipitation is present in the boundary layer, but brightness temperature differences and contrast between surface types is rapidly diminished as the optical depth increases beyond about 1.0, making it impossible to detect the underlying leads. This value is not at all unexpected as optical depths of up to 20 have been reported for ice crystal precipitation (*Curry et al.*, 1990).

Figure 1b shows the results assuming that an aerosol (haze) layer exists from the surface to a altitude of 2 km (the boundary layer aerosol model defined in LOWTRAN) over the same range of optical depths. In this figure two sets of channel 3 curves are shown to contrast the differences between nighttime (strictly thermal) and daytime simulations where the upper, bold set of curves relate to daytime conditions. Multiple scattered solar radiation adds significantly to the upwelling radiances as optical depths of the haze layer increase while the infrared channels do not show any multiple scattering effects. All other input parameters to LOWTRAN are the same as for Figure 1a. In the haze simulations it is obvious that the brightness temperature differences between channel pairs are small when only thermal radiances are considered (nighttime) over the entire range of optical depths while large differences exist between channel 3, and channels 4 or 5 when solar radiation is accounted for during the day. Also, the contrast between surface types for each channel remain significant over the range of visible optical depths shown, particularly when only thermal radiances are considered. Gross differences between Figures 1a and 1b

are due to markedly different properties of the haze and cirrus models defined for LOWTRAN.

The contrast between varying lead types and the ice pack can be expressed by the difference in simulated channel brightness temperature for a hypothetical lead temperature, say open water, 5 cm thick ice or 15 cm thick ice and the surrounding ice pack at any optical depth, normalized by the brightness temperature of the ice pack (here taken to be 2 m thick). Figures 2a and 2b show the normalized contrast for channel 4 assuming the conditions illustrated in Figures 1a and 1b respectively. This relative measure of contrast may provide a means to detect leads using AVHRR data even at night, though it is apparent that if optically thick ice crystal precipitation exists that the contrast is essentially zero making it impossible to detect leads using such a method.

Also modeled, though not illustrated here, were channel brightness temperatures, pair differences and normalized contrasts in surface types for high-level cirrus clouds at each viewing angle. Again, brightness temperatures converged at the blackbody radiating temperature at cloud top for large optical depths, but the convergence was less dramatic than in the case of low level ice crystal precipitation. Channel 3 minus channel 4 brightness temperature differences at 50° viewing angle were significant in this case reaching nearly 12 K over open leads at a 0.55 micron optical depth of about 2.6 with the difference being less than 5 K over the pack ice. Differences in these signatures when incorporated into image analysis algorithms in conjunction with ancillary information should be very useful in the detection of leads. Though the normalized contrast between surface types degrades with increasing cirrus optical depth, our simulations indicate that reasonable signatures should be detectable for a range up to about optical depth 4.0, that is, for most cirrus conditions expected to be observed in the Arctic region. Combining brightness temperature differences with contrast will improve our ability to detect leads significantly. Developing an algorithm to do so presents a challenge for the future.

3. EMPIRICAL APPROACHES AND RESULTS

While there have been studies of the effect of sensor resolution on parameter retrieval, the approaches have been empirical and have dealt only with cloud fraction (and a single cloud type such as cumulus; e.g., *Shenk and Salomonson* (1972), *Wielicki and Welch* (1986)) or land cover classes (e.g., *Woodcock and Strahler* (1987), *Townshend and Justice* (1988)). In the case of cloud fraction, real and synthetic data containing cloud fields were degraded in resolution, and the fractional coverage was observed as a function of scale. In the case of land cover classes, the variance of the image was plotted as a function of measurement scale for the purpose of determining the optimal resolution for monitoring. While all of these studies are useful, no concise statement of the relationship between fractional coverage and sensor resolution was given, so that the results are difficult to generalize to other parameters. An analytical solution to this problem is currently being investigated, but here we present results from an empirical study.

While there are advantages to comparing lead statistics derived from different types of imagery, such a study would be difficult given different acquisition times, wavelength ranges of the various sensors, and geolocation problems. To alleviate these problems, comparisons are made across image scales based on the same initial image, where the change in resolution is obtained by modeling the transfer function between the initial data and the desired resolution and then subsampling. A spatial filter that estimates the point spread function of the Landsat sensor is applied following the methodology presented in *Justice et al.* (1989). At each degradation cycle, Gaussian random noise is added back into the image to reduce the smoothing effects of the filtering operation. Images with FOVs of 160, 320, 640, and 1280 m were created in this manner. Data are Landsat Multispectral Scanner (MSS) band 4 (0.5-0.6 μm) scenes of the Beaufort Sea, March 1988, with an initial field-of-view (FOV) of 80 m.

Leads statistics are retrieved from a lead/not-lead binary image. To obtain the binary image the fourth order trend surface is removed from original grey scale image (*Eppler and Full*, 1992) and a

thresholding procedure is applied at each degradation cycle. Valid lead fragments are identified, where "valid" refers to a linear feature for which a meaningful width and orientation can be determined. Linearity is determined through correlation/regression analysis. Lead widths are measured perpendicular to the regression line, at 1 km intervals, and the slope of the regression line is the measure of the lead orientation.

One of the Landsat scenes analyzed is shown in Figure 3. Image size is 80 x 80 km, a subset of the full Landsat scene. The corresponding distribution of lead widths is shown in Figure 4. The disappearance of small leads due to a lack of contrast and the increase in the relative frequency of large leads as pixel size increases can readily be seen. In this particular image, a width threshold of approximately 250 m divides those leads which would disappear in the 320 and 640 m degradations. However, the criteria for how a given lead will "grow" or disappear during image degradation must include a measure of its thermal contrast to the surrounding ice. For example, a narrow, open lead might grow during the first degradation, accompanied by a drop in contrast due to smoothing, and then disappear in the subsequent scene. A narrow refrozen lead, in comparison, might disappear during the first degradation. This change in lead widths as a function of pixel size affects the total lead area as shown in Table 1 for the images in Figure 3, where lead area fraction decreases with increasing pixel size. Orientations of leads can also be expected to change, if anisotropy (i.e., a preferred orientation) exists. An illustration of this is shown in Figure 5 for the Landsat image in Figure 3. Results from other Landsat scenes show similar patterns.

Given that very small features will generally not be resolved, the issue then becomes one concerning the possibility of using the partial distribution of a particular statistic (e.g., lead widths) measured at low resolution to estimate the complete or "true" distribution of that parameter. For example, assume that lead widths, x, follow a negative exponential distribution with an unknown mean, λ. From a sampling point of view it is useful to treat the distribution of widths as discrete and address the number

n_i of leads in bin i that have widths between x_i and x_i+w where w is the width of the bin:

$$n_i = \frac{Nw}{\lambda} e^{-x_i/\lambda} \tag{1}$$

where N is the unknown total number of leads in the spatial area. The idea is that n_i is measured for a few bins, and that λ and N are estimated. To accomplish this, (1) is rewritten in linear form as

$$\ln(n_i) = \ln(\frac{Nw}{\lambda}) - \frac{1}{\lambda} x_i \tag{2}$$

Letting $a = \ln(Nw/\lambda)$ and $b = \lambda^{-1}$ and solving for a and b by the method of least squares with the observed data, the mean of the distribution and the total number of leads can then be estimated.

Experiments with this model show it to be very sensitive to the bin width and the number of bins in which leads actually occurred in the low resolution imagery. This is not unexpected considering that the entire range of x is being estimated in the least squares model by observations in only one part of its entire range (such extrapolation is not recommended). The problem can be alleviated somewhat by including a few observations of small lead widths; for example, measurements from a few SAR images within the same area.

4. SUMMARY AND CONCLUSIONS

The use of the thermal channels of the AVHRR for the detection and mapping of leads has been evaluated for varying atmospheric and surface conditions. Our approach included both modeling and empirical studies, discussed with respect to lead width. Concerning atmospheric effects, the detectability of leads is dependent on the degree of thermal contrast between surface types, which varies with surface and atmospheric conditions as well as sensor response. The transfer of radiation through the atmosphere is modeled using data from Arctic ice islands and climatological values of atmospheric chemical constituents. The satellite radiances in the three AVHRR thermal channels are simulated for a variety of surface and atmospheric conditions: a range of satellite view angles, four ice thicknesses (three within

leads), varying aerosol and ice crystal optical depths, and thin cirrus clouds. The change in the contrast between the lead and the surrounding ice is examined as a function of optical depth. For example, at ice crystal optical depths of more than 0.3 under mean January conditions in the central Arctic, the split-window brightness temperature differences between 2 m and 5 cm thick ice are similar to the ice temperature variability. Therefore, thresholding operations will not be able to distinguish between ice and leads. Due to the wide variety of atmospheric and surface conditions that exist in the Arctic, additional experiments in this area must be performed before general statements about the determination of optimal thresholds can be made.

Concerning measurement scale, Landsat MSS data is successively degraded from 80 m to 1.2 km field-of-views, using the modulation transfer function for the sensor. It can be seen that small leads disappear in the coarser resolution data and large leads "grow". The total lead fraction decreases with resolution, roughly following a fractal scaling relationship. Lead orientation distributions also change with increasing pixel size indicating that, in the imagery examined, small leads exhibit different orientations than larger leads. The possibility of using lead width distributions from AVHRR data to estimate the "true" lead width distribution is also assessed, where the large leads measured by satellite are first adjusted for their artificial growth, and then their distribution is used to predict the first moments of the true (hypothesized) negative exponential distribution. The results are shown to be very sensitive to the number and range of lead widths measured, but the accuracy of the procedure can be improved dramatically with a few samples of the same lead network at a higher resolution; e.g., from SAR data.

Acknowledgements. This work was supported by ONR grant N00014-90-J-1840 and NASA grant NAGW-2407 (University of Washington subcontract #721566).

REFERENCES

Curry, J.A., F.G. Meyer, L.F. Radke, C.A. Brock, and E. Ebert, 1990. Occurrence and characteristics of lower tropospheric ice crystal in the Arctic. *Int. J. Climatology*, 10, 749-764.

Eppler, D.T. and W.E. Full, 1992, Polynomial trend surface analysis applied to AVHRR images to improve definition of Arctic leads. *Remote Sensing of Environ.*, in press.

Justice, C.O., B.L. Markham, J.R.G. Townshend, and R.L. Kennard, 1989. Spatial degradation of satellite data. *Int. J. Remote Sens.*, 10 (9), 1539-1561.

Kneizys, F.X., E.P. Shettle, L.W. Abreu, J.H. Chetwynd, G.P. Anderson, W.O. Gallery, J.E.A. Selby, and S.A. Clough, 1988. Users Guide to LOWTRAN 7, AFGL- TR-88-0177, *Environmental Research Papers*, No. 1010, 137 pp.

Maykut, G.A., 1982. Large-scale heat exchange and ice production in the central Arctic, *J. Geophys. Res.*, 87(C10), 7971-7984.

Shenk, W.E. and V.V. Salomonson, 1972. A simulation study exploring the effects of sensor spatial resolution on estimates of cloud cover from satellites, *J. Appl. Meteor.*, 11, 214-220.

Townshend, J.R.G. and C.O. Justice, 1988. Selecting the spatial resolution of satellite sensors required for global monitoring of land transformations, *Int. J. Remote Sensing*, 9 (2), 187-236.

Wielicki, B.A. and R.M. Welch, 1986. Cumulus cloud properties derived using Landsat satellite data, *J. Clim. Appl. Meteorol.*, 25, 261-276.

Woodcock, C.E. and A.H. Strahler, 1987. The factor of scale in remote sensing, *Remote Sensing Environ.*, 21, 311-316.

Table 1. Changes in lead area fraction with pixel size in one Landsat scene.

Pixel Size (m)	Lead Area Fraction	Lead Area (km^2)
80	0.030	270.0
160	0.027	235.8
320	0.023	196.7
640	0.016	124.9

LIST OF FIGURES

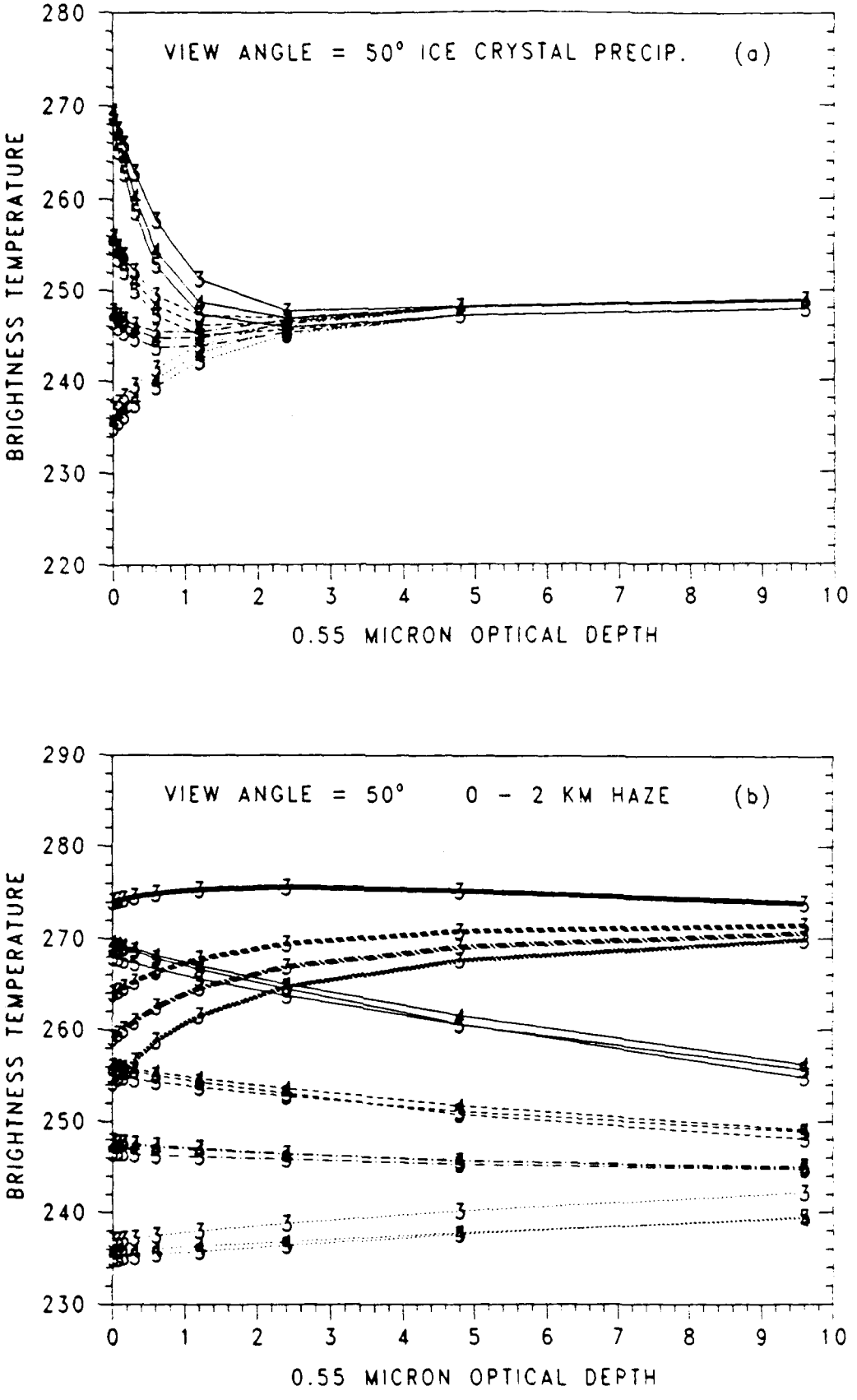

Figure 1. The effect of a layer of (a) ice crystal precipitation and (b) boundary layer haze on the three AVHRR thermal channels (3, 4, 5) at a satellite view angle of 50°. Optical depths (0.55 μm) are varied from 0 to 10. The tops of the ice crystal and haze layers are near the top of the inversion at a temperature of approximately 248 K. The brightness temperature change in each channel over each of the four surface types (ice thicknesses: 0, 5, 15, 200 cm from top to bottom) can readily be seen.

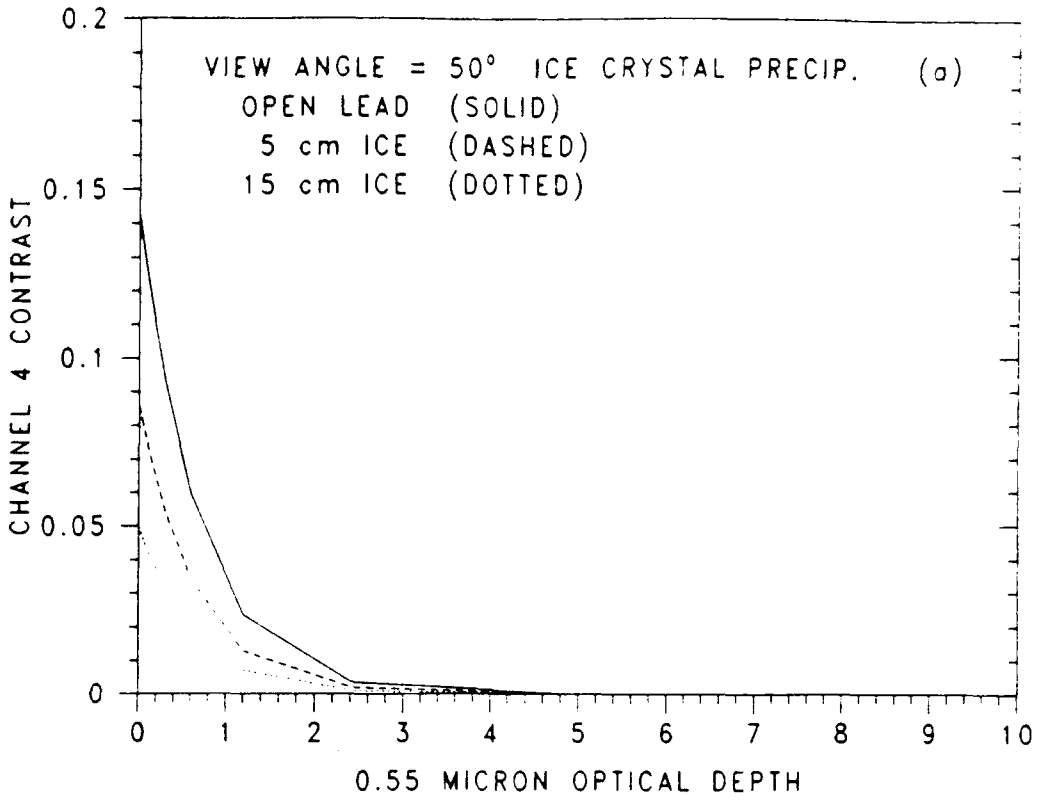

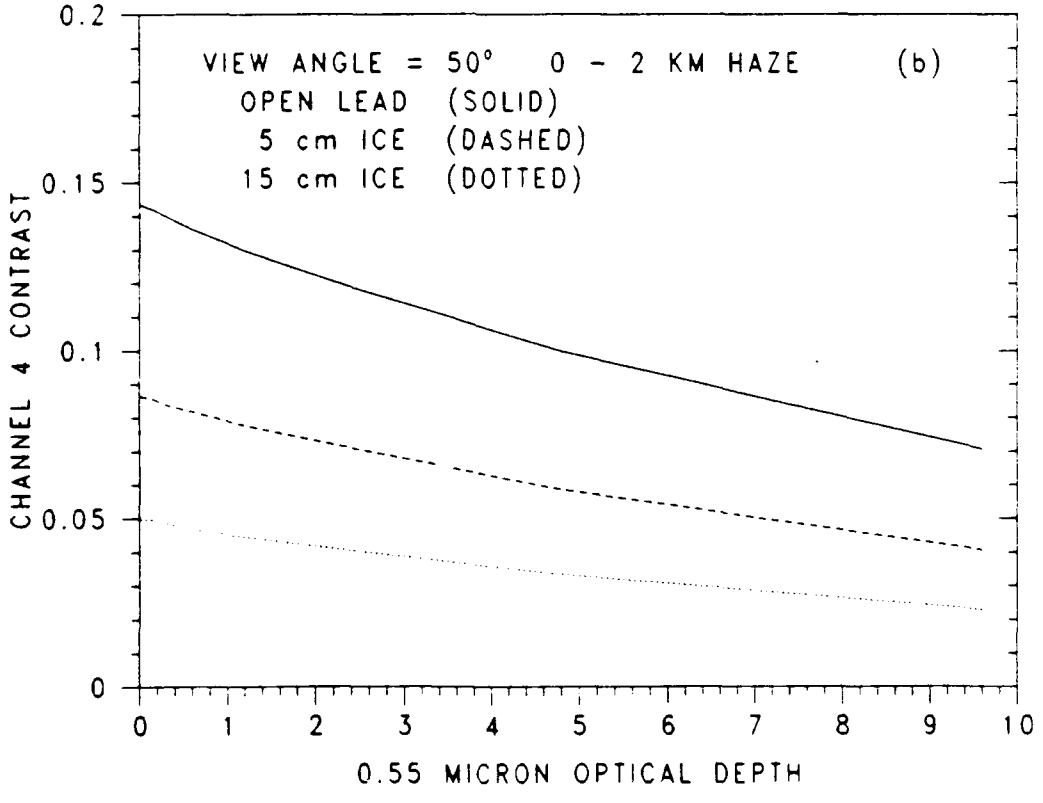

Figure 2. Normalized contrast between an open water lead and ice of two thicknesses for (a) ice crystal precipitation and (b) boundary layer haze. Conditions are mean January in the central Arctic.

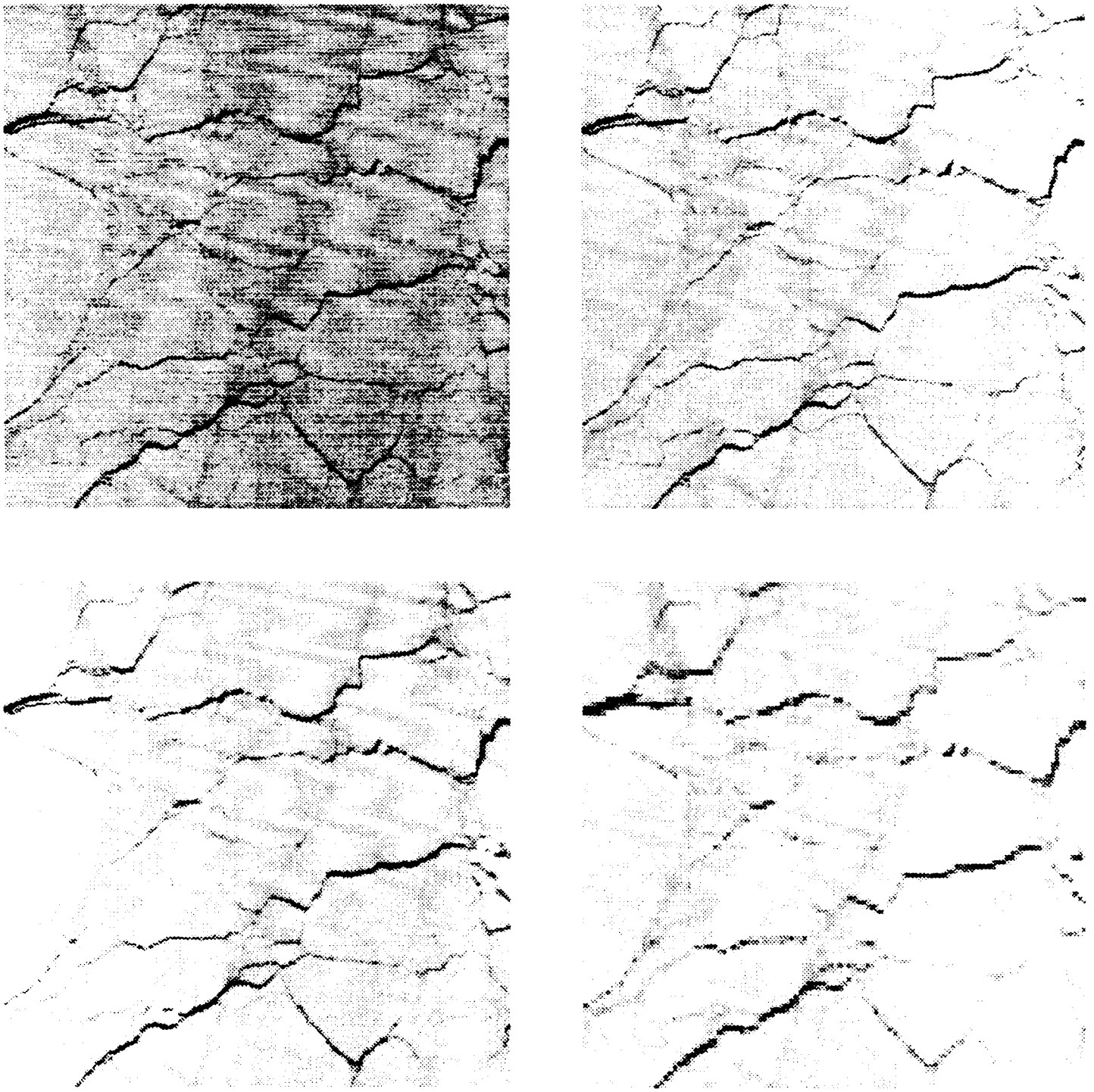

Figure 3. Landsat MSS band 4 scene of the ice pack north of Alaska in March 1988. Area covered in the upper left image is approximately (80 km)^2 The remaining are degraded images with pixel sizes of 160, 320, and 640 m.

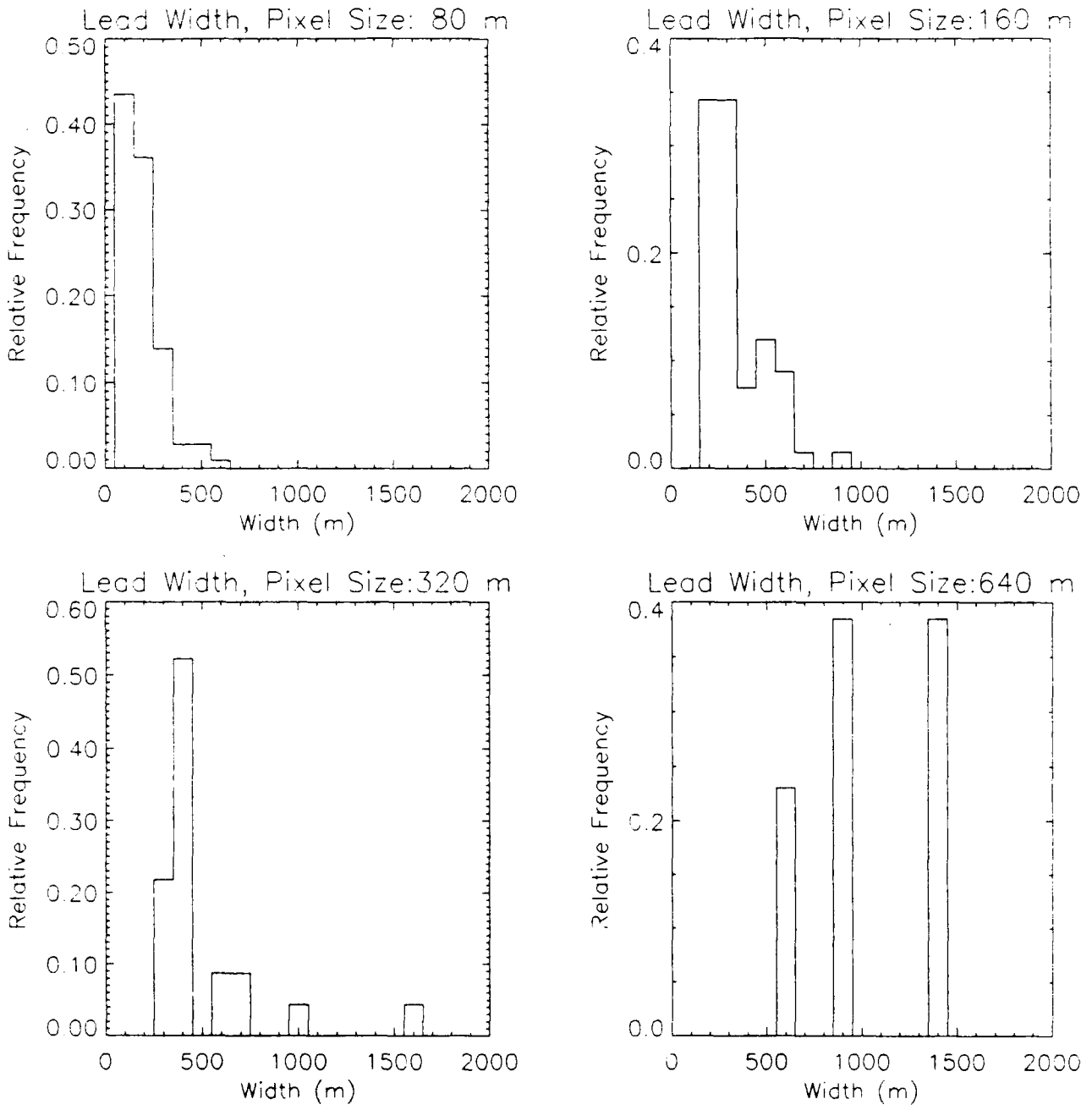

Figure 4. Lead width distributions for the images in Figure 3. Widths are grouped in 100 m bins.

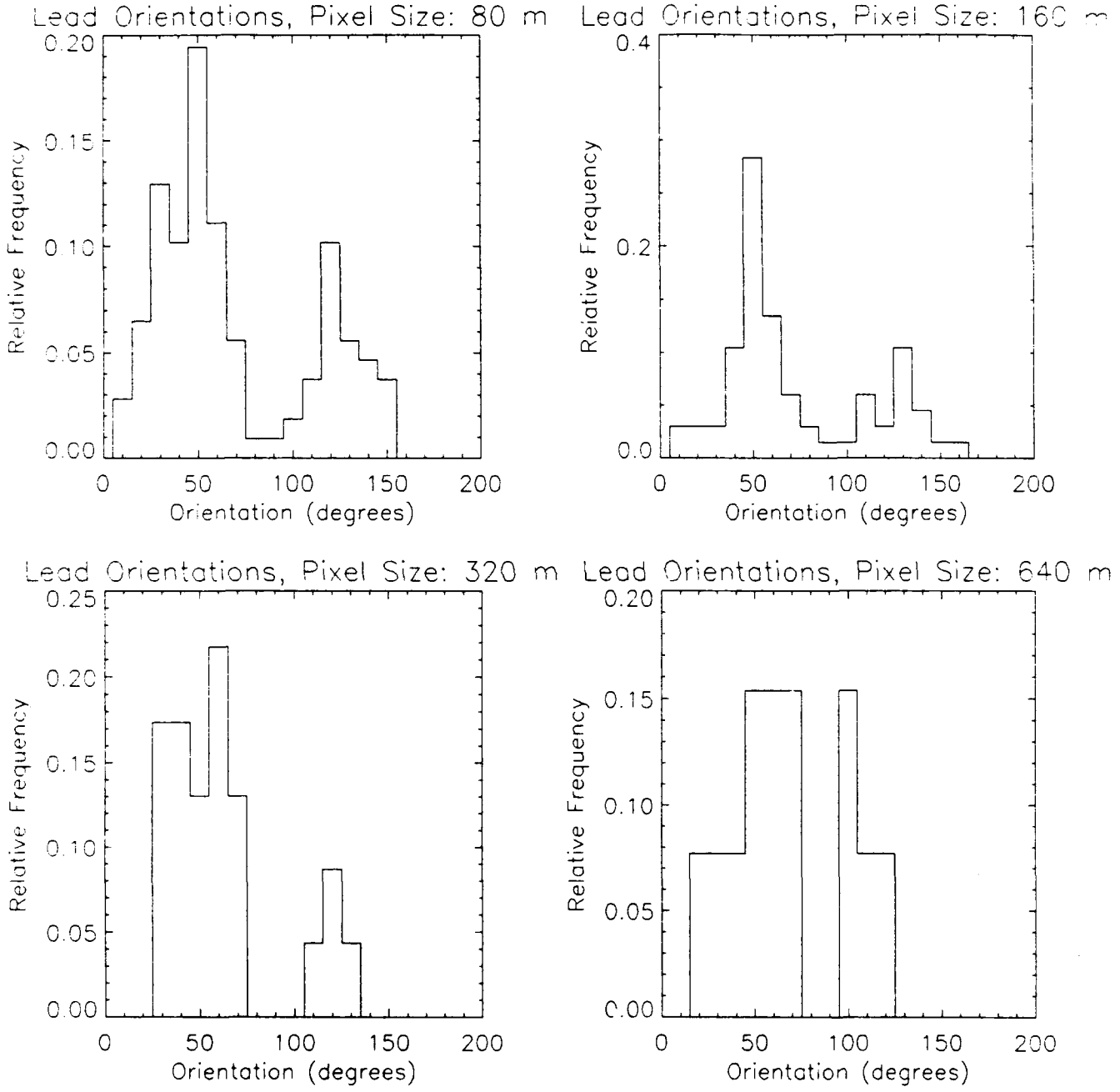

Figure 5. Lead orientations for the degraded Landsat series shown in Figure 3. Orientation is the angle that a lead makes with the horizontal axis, measured counterclockwise.